
Unterschrift des Betreuers



TECHNISCHE
UNIVERSITÄT
WIEN
Vienna University of Technology

DIPLOMARBEIT

Charge Sharing Studies of Silicon Strip Sensors for the CMS Phase II Upgrade

ausgeführt am
Institut für Hochenergiephysik
der Österreichischen Akademie der Wissenschaften

unter der Anleitung von
Priv.-Doz. DI Dr. Christoph SCHWANDA

und
DI Dr. Thomas BERGAUER

durch
Viktoria HINGER, BSc

Patrizigasse 13-15/3,
1210 Wien

28. März 2017

Unterschrift

Zusammenfassung

Das CMS Experiment am CERN steht als eines von vier großen Experimenten am Large Hadron Collider (LHC) vor zahlreichen Herausforderungen. Wissenschaftliche Zielsetzungen, wie Higgs-Präzisionsmessungen und die Suche nach neuer Physik jenseits des Standardmodells, machen es erforderlich, den LHC mit höherer Luminosität zu betreiben als zuvor. Die daraus erwachsenden Anforderungen müssen von CMS erfüllt werden. Das betrifft einerseits die Strahlenschäden am CMS Detektor und andererseits die erhöhte Anzahl an Kollisionen pro Frequenzintervall, welche die Rekonstruktion der Spuren von entstehenden Zerfallsprodukten erschweren. Mit geplantem Beginn ab 2023 werden im Rahmen des CMS Phase II Upgrades die notwendigen Anpassungen des CMS Detektors durchgeführt. Zu diesem Zeitpunkt wird auch der CMS Silizium-Tracking-Detektor das Ende seiner vorgesehenen Lebenszeit erreicht haben und vollständig erneuert werden. Die dort neu eingesetzten Siliziumsensoren müssen im extrem strahlungsbelasteten Milieu des High Luminosity LHC störungsfrei funktionieren. Zu diesem Zweck werden künftig, anstelle der aktuell verwendeten n-Typ Sensoren, p-Typ Siliziumstreifensensoren, welche sich insgesamt als stabiler gegenüber Strahlenschäden erwiesen haben, am CMS Tracker eingesetzt werden. Dementsprechend ist das Bestreben groß, p-Typ Siliziumstreifensensoren mit n^+ -Streifen einsatzbereit für den Betrieb im neuen CMS Tracker zu machen.

Diese Sensoren vom Typ n-in-p benötigen eine spezielle Struktur mit hoher p^+ -Dotierkonzentration, das sogenannte p-stop, zur elektrischen Separation der einzelnen Streifen. Für bestmögliches Sensorverhalten muss das p-stop Layout optimiert werden.

Als Hauptziel dieser Arbeit wurden mehrere Prototyp-Sensoren mit verschiedenen p-stop Geometrien und unterschiedlichen Implantationstiefen und Konzentrationen mithilfe eines Lasersystems sowie mit geladenen Teilchen aus einer radioaktiven ^{90}Sr -Quelle getestet. Um diese Tests zu ermöglichen, wurde ein kürzlich erworbenes Sensor-Auslesesystem am Institut für Hochenergiephysik in Wien in Betrieb genommen. Die zugehörige Datenanalysesoftware wurde angepasst und weiterentwickelt, um die Anforderungen, die aus positionsauflösenden Laserscans erwachsen, zu erfüllen. Mit diesem System wurden anschließend Vergleichsstudien mit den Prototyp-Sensoren durchgeführt und Eigenschaften wie die Aufteilung von Ladung zwischen benachbarten Streifen sowie Ladungsverluste an der p-stop Schicht untersucht. Anhand dieser Untersuchungen wird als Abschluss der vorliegenden Diplomarbeit eine mögliche Layoutkonfiguration vorgeschlagen, um die Performance der p-stop Schicht in Bezug auf die untersuchten Parameter zu optimieren. Diese Ergebnisse werden künftig von Bedeutung für weiterführende Entwicklungsschritte auf dem Weg zum neuen CMS Tracker sein.

Abstract

As one of the four large experiments at the LHC at CERN the CMS experiment is met with many challenges. Physics goals like precision Higgs studies and the search for physics beyond the Standard Model demand for the LHC to run at higher luminosities than before. CMS is now faced with the challenge to fulfil the requirements that come with the High Luminosity LHC. These include the radiation damage to the CMS detector and the increased number of collisions per bunch crossing, which make it more difficult to reconstruct the tracks of resulting decay products. The necessary adaptations to CMS will take place during the CMS Phase II Upgrade scheduled to start in 2023. By this time the CMS silicon tracker will have reached the end of its designated life time and will be replaced entirely. The newly installed silicon sensors have to ensure a smooth operation in the harsh radiation exposed environment of the High Luminosity LHC. For this purpose the CMS tracker will employ p-type silicon sensors, as they are known for a more resilient behaviour under irradiation than the currently installed n-type variant. Thus, high efforts are put into making p-type silicon strip sensors with n⁺-strip implants fit for the incorporation in the new CMS silicon tracker.

These n-in-p type sensors require a special structure of high p⁺ doping concentration, the so-called p-stop, to electrically separate the individual strips. To achieve the best possible performance of the sensors, this p-stop layout has to be optimised.

As the main goal of this thesis I tested a number of prototype sensors with various geometric p-stop layouts and varying implant depths and concentrations, employing an infrared laser system and a ⁹⁰Sr radioactive charged particle source. To facilitate these tests, I commissioned a newly purchased sensor readout system at the Institute of High Energy Physics in Vienna and adapted and enhanced the data analysis software to fit the needs of position sensitive laser scanning. With this system I subsequently conducted comparative studies with the prototype sensors, investigating properties like charge sharing between neighbouring strips and the phenomenon of charge loss at the p-stop layer. From these investigations, as a conclusion of this thesis, I move on to propose a possible layout configuration to optimise the performance of the p-stop layer with respect to these parameters. The such obtained results will be important for subsequent development steps along the way toward the upgraded CMS tracker.

Acknowledgements

The creation of this thesis is owed to the support and expertise of many people, colleagues and friends at HEPHY and also to the people outside of my scientific environment, who constantly encouraged me and stood behind me during the time of my studies.

First of all I want to express grateful thanks to Christoph Schwanda for supervising my thesis and helping me along the way of completing my studies.

Also, many thanks are owed to Thomas Bergauer, who welcomed me to HEPHY and supported this scientific project along the whole way. The finalised version of this thesis is owed to him and his expert supervision and useful inputs.

Special thanks to Axel König for the excessive help he offered me, whenever I had questions, and for conducting electric measurements of the sensors while I was sidelined by a fractured knee. I sincerely want to thank him and Johannes Grossmann and Elias Pree for helping me along especially at the beginning of my work at HEPHY, when I still had many questions to ask, for showing me the handling of the sensors and the laser system and the radioactive source, for all the helpful advice on programming and for their scientific input on any issue I encountered. Especially, of course, I want to thank them for being great colleagues and friends.

I also would like to thank Marko Dragicevic for a lot of helpful advice and scientific input, whenever there was an open question.

Furthermore I want to express thanks to Michael Hofer for the laser measurements he conducted together with me during the first weeks, as well as for the implementation of the AICoPi software for laser scans.

I also owe thanks to Wolfgang Brandner for always helping me around the clean room and providing the necessary infrastructure for the conducted measurements.

I want to also thank Andreas Berger, Roland Stark, Stefan Schultschik, Klaus Dieter Fischer, Christoph Irmeler and Markus Friedl for technical and scientific help along the way.

Finally I want to sincerely and gratefully thank all my friends and family, who supported me during the time of my studies. First and foremost, of course, I really owe my deepest thanks to my loving parents and my wonderful sister Isabella. They helped me through tough times on so many occasions and encouraged me to complete my studies that I really want to dedicate this work to them and their unconditional love and support. Thank you, with all my heart!

Contents

Zusammenfassung	i
Abstract	ii
Acknowledgements	iii
1 Background and Introduction	1
1.1 Introduction	1
1.2 The Large Hadron Collider at CERN	2
1.3 The CMS Experiment at the LHC	3
1.3.1 The CMS Tracker	4
1.3.2 The CMS Tracker Phase II Upgrade	6
1.4 The Physics of Semiconductors	7
1.4.1 Energy Bands	7
1.4.2 Doping	8
1.4.3 Charge carrier transport	9
1.4.4 The p-n Junction	10
1.5 Silicon Strip Sensors	12
1.5.1 Signal Generation	13
1.5.2 Radiation Damage	15
1.5.3 P-Stop Strip Separation	16
1.5.4 Sensor Design	18
2 Prototype Sensors and Test-Structures	21
2.1 Wafer Layout	21
2.1.1 Test-Structures	22
2.2 The P-Stop-GEO Sensor	22
2.2.1 Electrical Characterisation	24
3 Experimental Sensor Characterisation	26
3.1 The Laser Test Stand in the HEPHY Clean Room	26
3.2 The ALiBaVa Readout System	28
3.2.1 Hardware Components	29
3.2.2 Operation Modes	30
3.2.3 ALiBaVa Software	32
3.2.4 Offline Data Analysis	32
3.3 The P-Stop-GEO Sensor Module	33
3.3.1 Noise	35
3.4 Radioactive Source Tests	37
3.4.1 Measurement Procedure	37
3.4.2 Clustering	39
3.4.3 Signal Calibration	42
3.5 Strip Scans with the Infrared Laser	44
3.5.1 Signal Generation	44

3.5.2	Measurement Procedure	45
3.5.3	Tuning of the Laser Signal	45
3.5.4	Determination of the Laser Spot Size	46
3.5.5	Optical Properties of Different Sensor Layers	50
4	Results	55
4.1	Influence of the P-Stop Layer on Charge Sharing	55
4.1.1	The η -Function	55
4.1.2	Comparing Charge Sharing for Different P-Stop Layouts	57
4.2	Charge Loss at the P-Stop Implant	62
4.2.1	Comparison of Different P-Stop Layouts	62
4.3	Favoured P-Stop Layout	66
5	Summary and Conclusion	67
5.1	The P-Stop Layer and its Influence on Sensor Performance . . .	67
5.2	Outlook and Open Issues	68
A	ALiBaVa ROOT Macros for Offline Data Analysis	70
A.1	Installation	70
A.2	Important Classes and Functions	71
A.2.1	DataFileRoot	71
A.2.2	Analysis Methods	72
A.2.3	sin_preguntas.C	72
A.2.4	Processing of the Laser Data	74
A.3	Cluster Finding Algorithms	74
A.3.1	DataFileRoot::find_clusters()	75
A.3.2	DataFileRoot::find_clusters_vh()	76
A.4	The Common Mode Algorithm	77
	Bibliography	78

List of Figures

1.1	3D view of the CMS experiment.	4
1.2	First half of the CMS inner tracker barrel with layered sensor modules.	5
1.3	Fluence in the CMS Tracker.	6
1.4	Visualisation of the energy band model.	8
1.5	Schematic energy band representation of doped semiconductors.	9
1.6	Schematic visualisation of a p-n junction.	11
1.7	Energy loss (stopping power) for positive muons in copper as a function of $\beta\gamma = p/Mc$	14
1.8	Signal generation in silicon strip sensors.	15
1.9	Electron accumulation layer and p-stop implant.	17
1.10	Schematic 3D view of an n-in-p silicon strip sensor.	19
2.1	Schematic wafer layout.	22
2.2	Schematic view of the P-Stop-GEO sensor.	23
2.3	Global electric sensor parameters.	24
2.4	Electric strip parameters.	25
3.1	Schematic of the laser test stand.	27
3.2	ALCoPi Python programme graphical user interface.	28
3.3	ALiBaVa daughter board.	29
3.4	ALiBaVa mother board.	30
3.5	ALiBaVa graphical user interface.	33
3.6	P-Stop-GEO test module.	34
3.7	Microscope view of open channels on the P-Stop-GEO sensor module.	35
3.8	Low-pass RC filters.	35
3.9	Sensor noise levels.	36
3.10	Masking effect on non-Gaussian noise.	38
3.11	Non-Gaussian tails at radioactive source signal spectra.	39
3.12	Hit map of the ^{90}Sr source above the Infineon sensor.	40
3.13	Cluster widths of the ^{90}Sr source above the Infineon sensor.	41
3.14	Signal of the ^{90}Sr source for different cluster cuts and widths.	42
3.15	ADC response function to the Beetle chip test pulses.	43
3.16	Signal of the infrared laser.	46
3.17	Signal height of the infrared laser as a function of laser tune.	47
3.18	Laser scan over an aluminium strip.	48
3.19	Laser spot diameter for varying z heights.	49
3.20	Schematic of the surface layers of a silicon strip sensor.	52
3.21	Signal change due to surface layer variations for Hamamatsu and Infineon sensors.	53
3.22	Multilayer reflectance as a function of the layer thickness.	54

4.1	Reconstructed impact position using the η -function compared to the real position of the laser spot.	56
4.2	η -function with error bars.	58
4.3	η -function for the Hamamatsu P-Stop-GEO sensor.	59
4.4	η -function for the Infineon P-Stop-GEO sensor.	60
4.5	Simulation of the electric field in the inter-strip region of a silicon strip sensor.	61
4.6	Laser scans for the Hamamatsu P-Stop-GEO sensor.	63
4.7	Laser scans for the Infineon P-Stop-GEO sensor.	64
4.8	Charge loss at the p-stop layer, measured for Hamamatsu and Infineon sensors.	65
5.1	Proposed p-stop layout for minimised charge loss.	68

List of Tables

1.1	Variables of the Bethe Bloch equation	13
2.1	Wafer parameters	21
2.2	P-Stop-GEO layout dimensions	23
3.1	Laser parameters	26
3.2	Laser focus parameters	27

Chapter 1

Background and Introduction

1.1 Introduction

Already Goethe's Faust knew it to be one of humans' deepest desires to "*perceive whatever holds the world together in its inmost folds*"¹. Today's high-energy physics in principle serves exactly this ambitious purpose – to gain a deeper understanding of the constituents and the mechanisms that make up our world.

The knowledge we have of this field of science today is condensed in the so-called Standard Model of particle physics. It incorporates all known elementary particles and their interactions and is a very useful tool to describe a wide variety of physical phenomena and experimental results. However, as every theory has its limits, the Standard Model is far from being a "theory of everything". There are many fundamental questions it cannot answer. Such questions, like, e.g., the search for dark matter or the fundamental asymmetry of matter and antimatter, are therefore attributed to physics beyond the Standard Model. It is the main goal of today's efforts in high-energy physics to not only understand and test the Standard Model of particle physics, but especially to probe for new physics beyond.

For this purpose it is necessary to continuously improve the performance of particle accelerators, such as the Large Hadron Collider at CERN that provide the needed environment to conduct high-energy physics research, and also to develop new detector technologies that are able to cope with the harsh atmosphere of a high-energy physics experiment. Detector systems of such experiments have to fulfil the demands that arise with this constant need for improvement.

This thesis deals with the development of new silicon strip sensors that can be employed in such detector systems. It looks at a specific type of sensor test-structure designed to investigate the properties of the sensor with respect to electrical strip separation. For this purpose a readout system for silicon strip sensors for tests with a laser system and a radioactive source is commissioned in the laboratory of the Institute of High Energy Physics in Vienna. Subsequently, comparative tests with different geometric strip separation layouts are performed and the influence of the strip isolating structure on the sensor performance is studied, with the aim of eventually being able to provide a preferable layout estimate.

The following sections of chapter 1 provide the necessary physical background and concepts addressed in this thesis. The investigated silicon strip

¹German original [1]:
*„Dass ich erkenne, was die Welt
Im Innersten zusammenhält.“*

sensors are introduced in chapter 2. Chapter 3 covers the experimental environment and procedures employed during the course of the presented work. Measurement results and interpretations are presented in chapter 4. Finally, chapter 5 provides a summary of the findings of this thesis and an outlook on unresolved questions and future research prospects.

1.2 The Large Hadron Collider at CERN

The Large Hadron Collider (LHC) at the European Organization for Nuclear Research (CERN²) is the world's largest and most powerful particle accelerator as of today. It provides the necessary environment and infrastructure for thousands of scientists all over the world to conduct their research and, as such, plays an integral role for our current understanding of the universe.

The LHC is an underground synchrotron storage ring with a circumference of about 27 km. It was built near Geneva at the French-Swiss border, reusing the already existing underground tunnel of the Large Electron Positron Collider (LEP) and superseding it as the largest accelerator ring at CERN. Inside the ring protons are accelerated in two counter-rotating beams and collide with a centre-of-mass energy of up to 14 TeV [2]. In an additional mode of operation the LHC accelerates ²⁰⁸Pb nuclei instead of protons, reaching an energy of up to 2.76 TeV per nucleon or a centre-of-mass energy of 1148 TeV upon collision [3].

The collisions happen at four different interaction points, where the particle beams intersect. At each of these points a large-scale high-energy physics experiment is located to measure the particles produced in the collisions. ATLAS³ and CMS⁴, the two larger experiments of these four, are general-purpose detectors, built to investigate a wide range of particles and to search for new physics. The remaining two experiments, namely LHCb⁵ and ALICE⁶, each operate in a more specialised field of physics. While LHCb probes with high precision for CP-violation and rare decays of *b* (beauty) and *c* (charm) hadrons to find answers to fundamental questions like the asymmetry of matter and antimatter [4], ALICE investigates heavy-ion collisions in search for quark-gluon-plasma, a state of matter as it is assumed to have existed shortly after the Big Bang.

The proton beams are not continuous but, in case of the LHC, are made up of up to 2808 so-called "bunches" per beam. These are clouds of about 10¹¹ protons each that are injected into the accelerator in regular intervals and thus allow a precise timing of the collisions. A total of 1232 dipole magnets with a magnetic field of up to 8.33 T are distributed around the accelerator ring to keep the particles on their circular track, and 392 quadrupole magnets are used to focus the beams. The particles are accelerated by 8 radio-frequency (RF) cavities per individual beam. Aside from transferring energy to the beam during acceleration, the main role of these cavities is to keep the proton clouds tightly bunched to ensure high luminosity at the collision point [3]. The luminosity *L* of an accelerator is an indicator for the quality of the machine. It denotes the

²CERN: Conseil Européen pour la Recherche Nucléaire

³ATLAS: A Toroidal LHC Apparatus

⁴CMS: Compact Muon Solenoid

⁵LHCb: LHC-beauty experiment

⁶ALICE: A Large Ion Collider Experiment

number of collisions in a given time divided by the event cross-section. For a synchrotron it can be expressed as [5]

$$L = f \cdot n \cdot N_1 \cdot N_2 \cdot A^{-1}. \quad (1.1)$$

Here f denotes the collision frequency, n the number of bunches in the accelerator, N_1 and N_2 the number of particles per bunch, and A the beam cross-section at the interaction point. With tightly packed, well-defined proton bunches and a collision rate of up to 600 million collisions per second the LHC currently reaches a design luminosity of $10^{34} \text{cm}^{-2} \text{s}^{-1}$ in proton-mode [3].

In order to make new discoveries and provide quality physics by increasing the rate of rare events, an even higher luminosity is desirable for the future. Thus, various upgrades and improvements to the accelerator performance are planned for the long shut-down (LS) periods in-between data-taking runs. At the end of LS3, which is scheduled between 2023 and 2025, the instantaneous luminosity of the LHC is expected to level at $5 \times 10^{34} \text{cm}^{-2} \text{s}^{-1}$, with a potential peak value at $2 \times 10^{35} \text{cm}^{-2} \text{s}^{-1}$ [6]. With regard to this, the era of the LHC after 2025 is referred to as the High Luminosity LHC (HL-LHC).

1.3 The CMS Experiment at the LHC

The CMS experiment, or Compact Muon Solenoid, is one of the four main experiments located at the LHC. Built as a large, general purpose detector, it dedicates itself to seeking answers to fundamental questions like, what is the nature of dark matter, why did matter and antimatter not annihilate completely after the Big Bang, and do supersymmetric particles exist [7].

Much like a large onion, CMS is made up of various layers of sub-detectors, each specifically designed to measure important properties, like charge, momentum, and energy, of the particles produced in the LHC collisions. These layers are arranged in concentric cylinder shape around the particle interaction point at the very centre with corresponding end-caps at the cylinder openings, completing the characteristic barrel-shape of the detector (Figure 1.1).

As its name suggests, one of the main components of CMS is a large superconducting solenoid magnet, capable of producing a magnetic field of nearly 4 T [7]. The tracks of charged particles are bent by the strong magnetic field, and from the curvature of those tracks the particle momenta can be deduced. Thus, albeit not a detector itself, the solenoid plays an important role for particle identification. Its iron return yoke, used to confine the magnetic field, makes up for 12,000 tons of the total detector weight of 14,000 tons. This, together with the experiment's "small" size as compared to other detectors such as ATLAS, is why CMS is referred to as "compact" in its acronym.

From the interaction point at the centre of the detector particles first travel through the silicon tracking system (see the following section 1.3.1), which charts the tracks of charged particles and such allows to determine their momenta. Outside of the tracker the particles hit the two different calorimeters that measure the energy of the incoming particles. The electromagnetic calorimeter (ECAL) is made to measure the energy of electromagnetically interacting particles, such as electrons and photons, whereas the outer hadronic calorimeter (HCAL) measures the energy of any particle comprised of quarks. These calorimeters are specifically designed so that the incoming particles deposit all of their energy inside that detector part and such are stopped in their

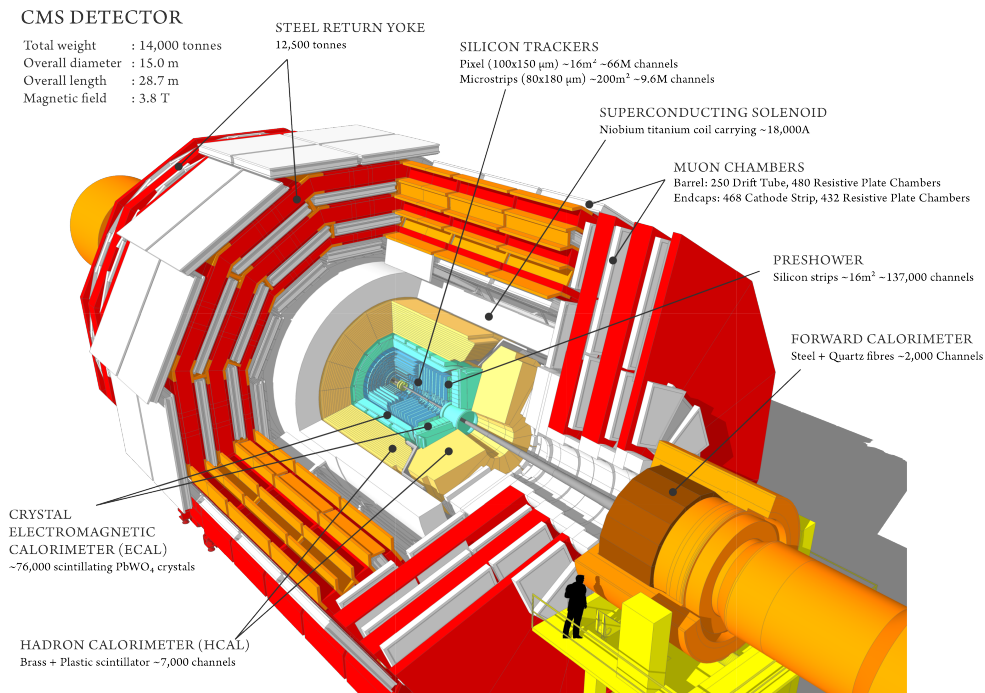


FIGURE 1.1: Schematic 3D view of the CMS experiment, showing the individual detector layers [7].

tracks [7]. However, weakly interacting particles such as muons make it past the calorimeter and even past the iron return yoke of the solenoid. This is why a key feature of CMS, which is also accounted for in the name “Compact Muon Solenoid”, are the muon chambers in the outer part of the experiment. These are drift tubes and wire chambers alternating with layers of the iron return yoke [7]. They are specifically designed to detect muons, which have an especially high importance for the identification of short-lived particles like, e.g., the Higgs boson.

In 2012 both, the ATLAS and CMS collaboration, observed a particle with a mass of about $125 \text{ GeV}/c^2$ that could later be identified as a Higgs boson [6]. Since its postulation by Peter Higgs in 1964 [8, 9] as the manifestation of a mechanism that introduces the mass of elementary particles, the Higgs boson was regarded as the last missing puzzle piece in the Standard Model of particle physics, and, as such, high efforts were put into the task of finding it. The discovery in 2012 was indeed so significant to the world of physics that in 2013 François Englert and Peter Higgs were awarded the Nobel Prize in Physics for their discovery of the underlying mechanism [10].

1.3.1 The CMS Tracker

The innermost part of the CMS experiment is the CMS tracker [11]. Its main purpose is to record the trajectories of charged particles so that from this the particle momentum can be deduced. Thus, the tracker plays an important role for particle identification. The entire CMS tracker is contained in a cylinder with a length of 5.8 m and a diameter of 2.6 m [6]. To assure a good performance of the CMS experiment, the tracker has to measure the particle tracks

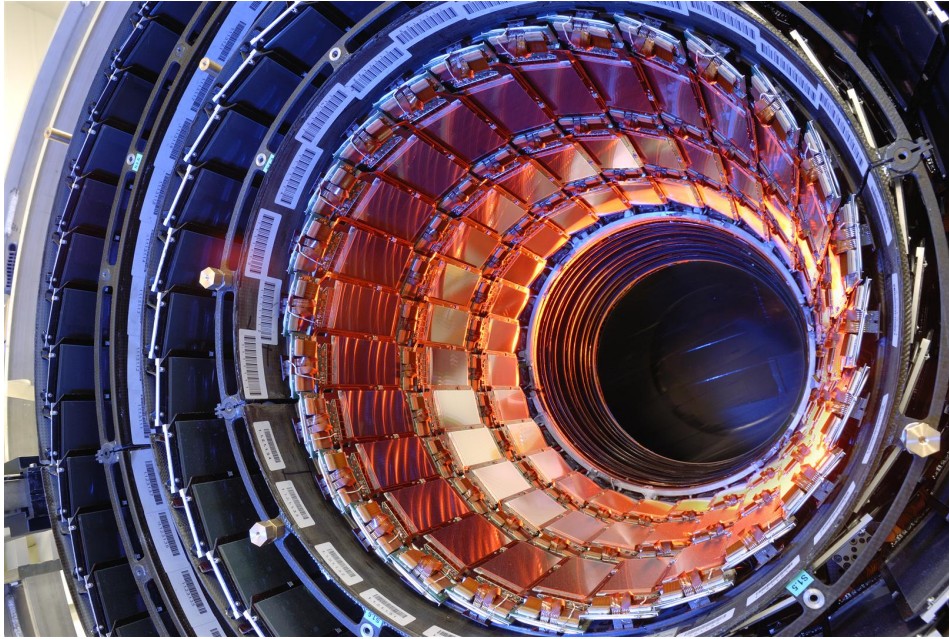


FIGURE 1.2: First half of the CMS inner tracker barrel with layered sensor modules [13].

as accurately as possible yet interfere with the particles as little as possible. Additionally, the tracker material must be able to function properly even under the high radiation stress resulting from the LHC design luminosity. For these reasons the CMS tracker is wholly made out of silicon detector material, comprising silicon pixel sensors at the very centre and silicon micro-strip sensors in the outer layers [12].

The pixel detector is the first detector barrier the particles emerging from the collision traverse on their way through CMS. Located closest to the interaction point, it has to resolve a large number of tracks with a particle rate as high as $10 \text{ million particles cm}^{-2} \text{ s}^{-1}$ at 8 cm distance from the beam line. To tackle this task, it contains 65 million pixels on roughly the size of a shoe box [7].

Right after the pixel detector the traversing particles pass through the silicon micro-strip tracker. It consists of ten overlapping cylindrical layers of silicon strip sensors in the barrel region (Figure 1.2) – four in the inner barrel (TIB) and six in the outer barrel (TOB). Two inner disks (TID) and two end-caps (TEC) close off the detector. Due to the high radiation exposure and the damages that occur in the silicon because of it, the entire tracker is cooled to -20°C . In total the silicon strip tracker contains roughly 15,200 sensor modules with about 10 million individual strips, which are read out by 80,000 micro-electronic chips. The modules consist of one or two silicon strip sensors, a mechanical support structure, and the read-out electronics [7].

The silicon strip sensors used in the tracker vary in shape and size according to their respective place in the detector with, e.g., the sensors with shorter strips and higher granularity being placed in the inner parts and those with longer strips and lower granularity at the outer layers. A description of silicon strip sensors and their working principle is given in sections 1.4 and 1.5.

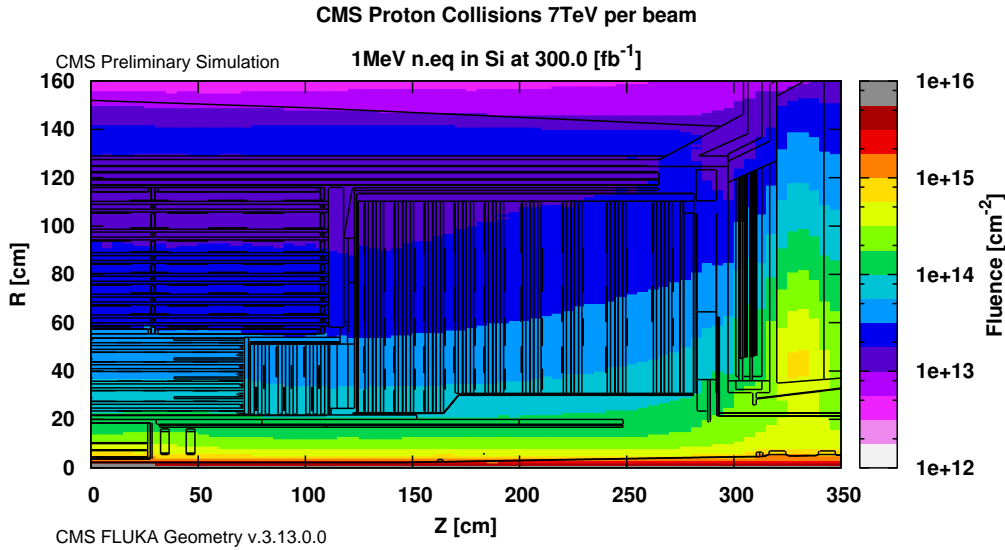


FIGURE 1.3: Simulation of the 1 MeV neutron equivalent fluence in the CMS tracker region for an integrated luminosity of 300 fb^{-1} . The interaction point in the centre is at the axes' origin [15].

1.3.2 The CMS Tracker Phase II Upgrade

As discussed in section 1.2, the luminosity of the LHC is expected to reach $5 \times 10^{34} \text{ cm}^{-2} \text{ s}^{-1}$ by 2025. With this improvement comes a new set of challenges for the LHC experiments. For the CMS tracker, especially, this means a number of new objectives. For one, the radiation exposure of the detector will significantly increase during the high-luminosity era of the LHC. Secondly, the increased luminosity means a higher number of collisions per bunch crossing, resulting in a larger pile-up in the detector. This makes it more difficult to resolve and reconstruct the tracks of individual particles.

The necessary upgrades to the CMS experiment are scheduled to take place during LS3 between 2023 and 2025, by which time the end of the designated tracker life-time will be reached. This is called the Phase-II upgrade of the Compact Muon Solenoid [6]. Next to other improvements it will see a complete replacement of the silicon tracker. A replacement is necessary, since the radiation damage due to the constant bombardment with particles will already be significant by then. Figure 1.3 shows the fluence inside the CMS tracker for an overall integrated luminosity of 300 fb^{-1} , as it is expected to be reached by 2023. The fluence is scaled to 1 MeV neutron equivalent according to the NIEL (non-ionising energy loss) hypothesis [14].

For the new silicon tracker three main areas of improvement can be pointed out. Firstly, the granularity of the sensor elements will have to be improved to adapt to the overall higher track density. Furthermore, the new sensors will have to be built to withstand the expected high radiation damage. And as the third objective the tracker needs to provide input to the CMS level one trigger to help lower the trigger rate to deal with the high number of events and only store and process the “interesting” ones. With this in mind, it becomes an important objective to develop new sensor technologies that are able to tackle the challenges that arise with the High Luminosity LHC.

1.4 The Physics of Semiconductors

1.4.1 Energy Bands

Semiconductors, like silicon, are generally crystalline or amorphous solids. Silicon, for example, crystallises in a tetrahedral diamond lattice structure, where each atom is surrounded by four closest neighbours that form covalent bonds by sharing their four valence electrons. The periodic potential of the atomic nuclei in the crystal lattice leads to the degeneration of the normally discrete energy levels of the bound electrons to continuous energy bands [16]. At low temperatures all valence electrons are bound. However, at higher temperatures they may be excited through thermal vibrations and break out of the covalent bond. The freed electron leaves behind an empty space, or a “hole”, equivalent to a positive charge carrier. Speaking in the energy band model, these electrons are excited from the valence band into the conduction band, generating holes in the valence band. The free electrons can move through the lattice, and, similarly, a hole may be filled by a neighbouring electron, causing the vacancy to move as well. Hence both, the electrons and the holes, are available for conduction [17].

Whether or not there can be electrons in the conduction band depends on the temperature and the material. Due to them being fermions, electrons follow Fermi-Dirac statistics. The probability of an energy state E to be occupied at a given temperature T is given by the Fermi-Dirac distribution function [16]

$$F(E) = \frac{1}{1 + \exp[(E - E_F)/kT]}. \quad (1.2)$$

Here k is the Boltzmann constant, and E_F is the Fermi level, denoting the energy level where at thermal equilibrium the occupation probability is one half.

Depending on the location of the Fermi level and the band structure, we can distinguish conductors, isolators, and semiconductors (Figure 1.4). For conductors the Fermi level lies in the conduction band. Valence and conduction band overlap, and the electrons from the valence band contribute to the current flow. Insulators, on the other hand, generally have a large gap of forbidden energy states between the valence and the conduction band. The Fermi level lies in this band gap, far away from the conduction band, reducing the probability of an electron to be lifted into the conduction band to practically zero. Semiconductors have a band gap as well, but it is small enough to be overcome by thermal excitation. For silicon at room temperature and under normal atmospheric pressure the band gap is 1.12 eV [16].

Due to this small band gap, the electrons in semiconductors already occupy the conduction band at room temperature. These electrons may recombine with holes in the valence band, while new electrons may be excited into the conduction band. Eventually, thermal equilibrium is established between excitation and recombination, and for a semiconductor without any impurities in the crystal lattice (*intrinsic semiconductor*) the number of free electrons n is equal to the number of free holes p ($n = p = n_i$). The intrinsic charge carrier density n_i is given by [16]

$$n_i = \sqrt{N_C N_V} \cdot \exp\left(-\frac{E_G}{2kT}\right) \propto T^{3/2} \cdot \exp\left(-\frac{E_G}{2kT}\right), \quad (1.3)$$

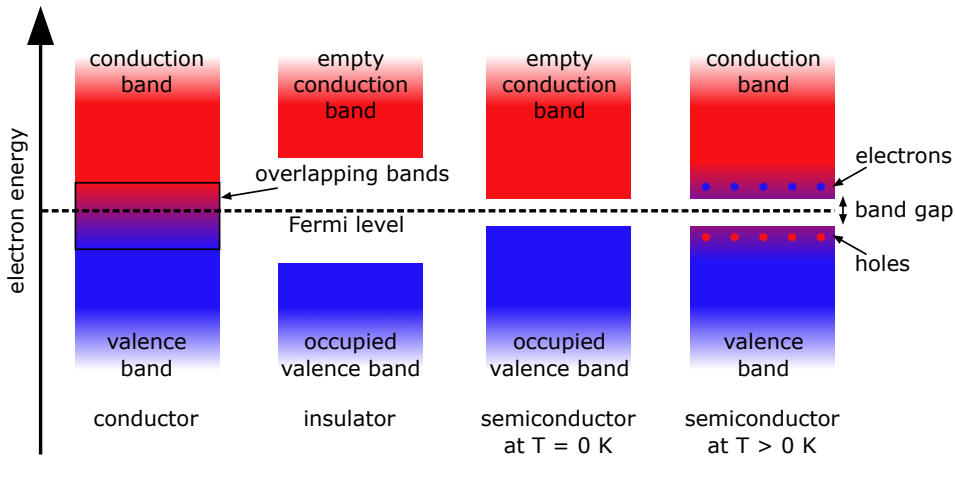


FIGURE 1.4: Visualisation of the energy band model.

where N_C and N_V are the effective densities of states in the conduction band and valence band respectively, and $E_G = E_C - E_V$ is the band gap. The Fermi level of an intrinsic semiconductor generally lies very close to the middle of the band gap [16]. The proportionality factor in equation 1.3 includes the effective masses of electrons and holes in the crystal lattice. From quantum mechanical considerations it can be deduced that for many purposes it is sufficient to treat the electrons and holes in the conduction and valence bands like free particles, but with an effective mass different from that of free elementary electrons [17].

1.4.2 Doping

Industry hardly works with intrinsic semiconductors. Instead, in most cases the properties of the material are intentionally altered by introducing small impurities into the crystal. Such a material is then called an *extrinsic semiconductor*. The procedure of generating an extrinsic semiconductor is referred to as doping.

Generally, one can distinguish two different ways of doping – n-type and p-type. For n-type semiconductors an excess of electrons is generated in the conduction band, while for p-type semiconductors additional holes are introduced into the valence band. Silicon, as an element of group IV in the periodic table of elements, can be doped by adding impurities from either group V (n-doping) or group III (p-doping). If impurities like arsenic or phosphorus with five valence electrons are introduced into the silicon lattice, only four of these electrons form the covalent bond with the neighbouring atoms. The fifth electron is “donated” to the lattice as a free conduction electron. Impurities like arsenic are therefore called electron *donors*. Similarly, a free hole is introduced by adding elements with only three valence electrons like boron or indium. In this case an additional electron is “accepted” to complete the covalent bonds around the impurity, which is called an electron *acceptor* [16].

Looking at the energy band model, the process of doping introduces additional energy levels that usually lie within the band gap. A donor impurity introduces an energy level close to the edge of the conduction band, filled with loosely bound electrons. Conversely, an acceptor impurity generates an additional energy level close to the valence band, filled with loosely bound holes.

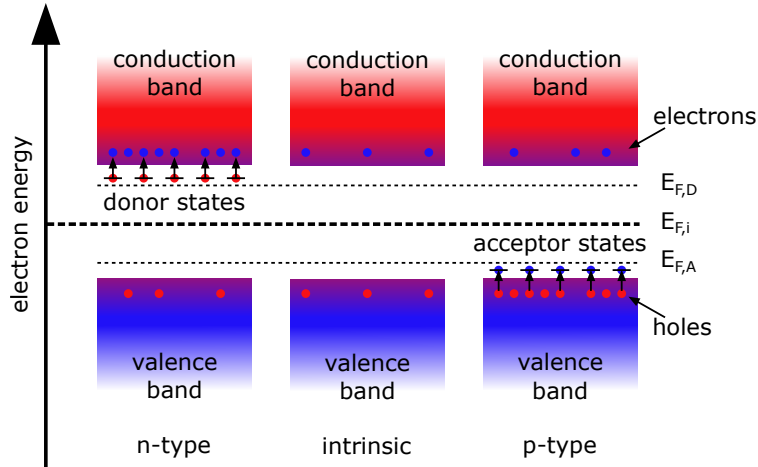


FIGURE 1.5: Schematic energy band representation of extrinsic n-type and p-type semiconductors compared to the intrinsic case.

At room temperature these newly introduced states will be almost completely ionised, i.e., the electrons from the donor levels will be lifted into the conduction band, and the holes in the acceptor levels will be filled with electrons from the valence band (generating holes in the valence band). This situation can be described by a shift of the Fermi level for doped semiconductors as compared to the intrinsic Fermi level $E_{F,i}$ (Figure 1.5). Donor impurities shift the Fermi level closer to the conduction band to $E_{F,D}$, while acceptor impurities lower the Fermi level toward the edge of the valence band to $E_{F,A}$ [17].

1.4.3 Charge carrier transport

When generated, electrons and holes can move through the semiconductor. The two main mechanisms responsible for this charge carrier transport are drift and diffusion. These two processes become especially important for systems out of thermal equilibrium.

Drift

When an external electric field is applied to the semiconductor material, the charge carriers will be accelerated in-between random collisions in a direction determined by the electric field. The drift velocity is dependent on the electric field strength E and the carrier mobility μ by

$$v_n = -\mu_n \cdot E \quad (1.4)$$

for electrons, and

$$v_p = \mu_p \cdot E \quad (1.5)$$

for holes [16]. The mobility μ is affected by scattering of the carriers at acoustic phonons and ionised crystal impurities and, as such, depends on temperature and the effective mass m^* of the charge carriers. Qualitatively, the mobility

can also be related to the mean carrier lifetime τ_m with [16]

$$\mu = \frac{q \cdot \tau_m}{m^*}, \quad (1.6)$$

where q is the electric charge of the electrons or holes respectively.

With increasing electric field the drift velocity no longer is linearly dependent on the electric field with the mobility as proportionality constant. For semiconductors like silicon and germanium it becomes less and less dependent on the applied field and approaches a saturation velocity of

$$v_s = \sqrt{\frac{8E_p}{3\pi m_0}} \approx 10^7 \text{ cm/s}, \quad (1.7)$$

where E_p is the optical-phonon energy [16]. With further increasing electric field the carriers gain enough energy to ionise atoms of the crystal lattice and in turn produce more electron-hole pairs. This results in an avalanche-like multiplication of charge carriers. For silicon the threshold energy where ionisation starts lies at 3.6 eV for electrons and 5.0 eV for holes [16]. The voltage that must be applied for avalanche multiplication to occur is generally referred to as the breakdown voltage [16].

Diffusion

While charge carrier drift occurs with an external electric field present, the mechanism of diffusion takes place without any external field. Rather, it is caused by a non-uniform distribution of excess charge carriers. As the system strives toward a state of uniformity, this leads to a movement of charge carriers along the gradient of carrier concentration, from the region of high concentration toward the region of low concentration. The flux of charge carriers is governed by Fick's law [16]

$$\left. \frac{d\Delta n}{dt} \right|_x = -D_n \frac{d\Delta n}{dx}, \quad (1.8)$$

where Δn is the difference in electron concentration, and D_n is the diffusion coefficient for electrons. For holes equation 1.8 holds with Δp as the difference in hole concentration and D_p as the diffusion coefficient for holes. Charge carrier mobility and diffusion coefficient are related by the Einstein equation

$$D = \frac{kT}{q} \mu \quad (1.9)$$

for electrons and holes respectively [16]. The diffusion length L_d , or the distance carriers can travel before they are annihilated by recombination, depends on the carrier lifetime τ and the diffusion coefficient D by [16]

$$L_d = \sqrt{D\tau}. \quad (1.10)$$

1.4.4 The p-n Junction

Contacting p-doped and n-doped semiconductor materials generates a so-called p-n junction (Figure 1.6). The junction shows diode characteristics,

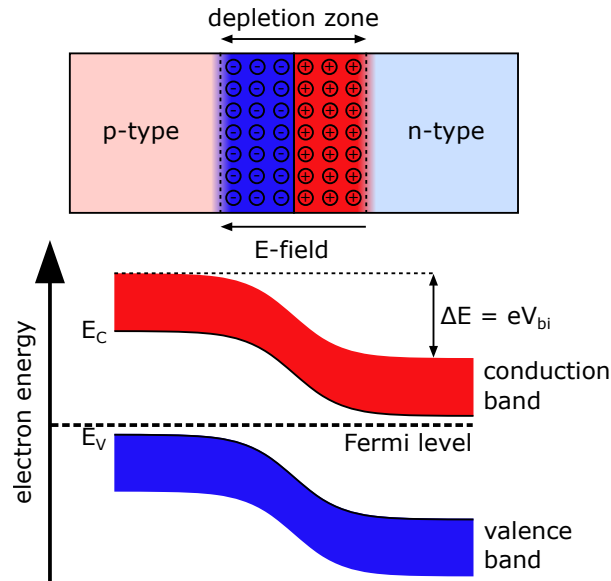


FIGURE 1.6: Schematic visualisation of a p-n junction in thermal equilibrium with shifted energy bands at the bottom.

meaning it conducts current mainly in one direction [17]. It can be considered one of the most important electronic structures today.

If p- and n-doped materials are brought into contact, the resulting gradient in charge carrier concentration causes the majority charge carriers to move into the adjacent material. Electrons diffuse from the n-side to the p-side, and holes wander from the p-type material into the n-doped crystal. There the carriers recombine with their respective counterparts. However, this means that the respective majority charge carriers are missing in the semiconductor material, which should be uncharged in a state of equilibrium. Due to the missing charge carriers, an excess of negative charge is created in the p-region, and an excess of positive charge in the n-region of the junction. This causes an electric field that induces a charge carrier drift, counteracting the diffusion movement. At thermal equilibrium drift and diffusion are balanced, and a space-charge region without any free charge carriers forms around the boundary of the p-n junction. The width of this *depletion zone* depends on the doping concentration and the intrinsic charge carrier concentration of the material. If both, p- and n-side, have the same doping concentration, the depletion region will stretch equally into both directions from the boundary. If one material exhibits a higher doping concentration, the depletion region will be wider on the less doped side [17].

Looking at the energy band model, the Fermi levels on both sides of the junction have to line up in thermal equilibrium. This causes a shift of the energy bands and a potential barrier to form. The potential difference V_{bi} between the positively charged n-side and the negatively charged p-side is called built-in voltage or diffusion voltage [17].

If an external voltage is applied to the p-n junction, the system is no longer in thermal equilibrium, and the properties of the diode vary with the direction of the applied voltage. Depending on the direction of the external voltage, one speaks of forward and reverse biased mode.

To operate the diode with forward bias, the anode is contacted to the p-side of the p-n junction and the cathode to the n-side. As a result electrons and holes can advance further into the space-charge region. The potential barrier in the depletion zone diminishes, and the depletion region itself narrows until at high-enough voltages it vanishes completely. This causes the current across the junction to increase significantly.

If, on the other hand, the positive electrode is connected to the n-side, and the negative electrode is connected to the p-side, the diode is operated in reverse biased mode. In this case the electrons and holes are pulled toward the respective electrodes, away from the depletion zone. As a result the depletion region widens, and the potential barrier increases. Diffusion across the junction is strongly suppressed. However, the current across the junction does not reach zero. Charge carriers can still be thermally excited inside the depleted volume and cause a very small flow of current, the so-called leakage current or dark current. With increasing bias voltage the depletion region grows closer towards the electrodes until the depleted volume reaches across the entire width of the semiconductor device. The minimum voltage necessary to achieve this state is referred to as *full depletion voltage*. Its value can be determined by measuring the capacitance of the p-n junction as a function of the bias voltage. With the depletion region acting as an insulator separating the two diode contacts, the p-n junction behaves analogously to a parallel plate capacitor, and, as such, also exhibits a capacitance. When the bias voltage is increased and the depletion region becomes wider, the capacitance gradually decreases until its minimum value is reached at full depletion. Consequently, the capacitance will not decrease any further, even if the bias voltage is increased. From the resulting capacitance-voltage characteristics the full depletion voltage can be determined [18].

The current-voltage characteristics of an ideal diode are given by the Shockley equation [16]

$$I(V) = I_0 \left[\exp\left(\frac{qV}{kT}\right) - 1 \right]. \quad (1.11)$$

Here it is assumed that voltages $V > 0$ denote a positive forward bias and values $V < 0$ indicate an operation with reverse bias. As can be seen from equation 1.11, for forward bias the current increases exponentially, while for reverse bias it eventually saturates for high negative voltages at the saturation current I_0 . This ideal diode behaviour holds qualitatively true as long as the reverse bias voltage does not exceed a certain limit. If this so-called *breakdown voltage* is reached, electric breakdown occurs, and the reverse bias current increases drastically. The most important mechanism responsible for the breakdown at high fields is avalanche multiplication when the electric field becomes high enough that the accelerated charge carriers can break up covalent bonds in the lattice and create new electron-hole pairs. Additionally, thermal instability and tunnelling effects can also cause diode breakdown [16].

1.5 Silicon Strip Sensors

Next to its many applications in electronics and everyday technological life, silicon is well established as a detector device in particle physics today. Because of its small band gap, its high density, and nonetheless excellent charge carrier mobility, it is highly suitable for the detection of ionising radiation [17].

TABLE 1.1: Explanation of the variables used in the Bethe-Bloch formula.

Symbol	Description
N_A	Avogadro's number
r_e	Classical electron radius
m_e	Electron mass
Z	Atomic number of the target material
A	Atomic mass of the target material
ze	Charge of the incident particle
$\beta = \frac{v}{c}$	Ratio of the particle velocity v to the speed of light
$\gamma = (1 - \beta^2)^{-1/2}$	Relativistic Lorentz factor
T_{\max}	Maximum kinetic energy transferred to a free electron in a single collision
I	Mean excitation energy in eV
δ	Density-effect correction

In addition, the sensor development benefits greatly from the extensive experience of the semiconductor industry. To acquire the high position resolution that detectors like the CMS tracker require, the sensors are divided into thin strips (or pixels) that are read out individually.

1.5.1 Signal Generation

When a moderately relativistic charged particle travels through matter, it loses some of its energy through interaction with the surrounding material. Most of the energy loss is due to ionisation. The Bethe-Bloch formula [19]

$$-\frac{dE}{dx} = 4\pi N_A r_e^2 m_e c^2 \rho \frac{Z}{A} \frac{z^2}{\beta^2} \left[\frac{1}{2} \ln \left(\frac{2m_e c^2 \beta^2 \gamma^2 T_{\max}}{I^2} \right) - \beta^2 - \frac{\delta}{2} \right] \quad (1.12)$$

describes the differential energy loss of charged particles per mass surface density of the traversed material in units of MeV/(g cm⁻²). The meaning of the used variables is listed in Table 1.1.

As can be seen in Figure 1.7, the Bethe-Bloch formula provides a very good description of the energy loss in the momentum range $0.1 < \beta\gamma < 100$. For lower energies of the incident particle the assumption of static atomic electrons does no longer hold true, and corrections must be made, while at higher energies radiative effects, which the Bethe-Bloch formula cannot describe, become increasingly important. Particles for which the mean energy loss lies close to the minimum of the Bethe-Bloch curve are called minimum ionising particles (MIP). For most practical purposes particles like the ones produced in LHC collisions can be considered MIPs.

The actual energy loss of a charged particle in matter is a statistical process that fluctuates around the mean value described by the Bethe-Bloch formula. For sufficiently thick absorber materials this is described by a Gaussian function. When looking at thin layers like typical silicon strip sensors⁷, however, it has to be taken into account that a fraction of the transferred energy is carried off by high-energetic δ -electrons. In this case the energy loss follows a Landau distribution [20]. Interactions with small energy transfer are more probable

⁷The typical thickness of silicon strip sensors ranges between 200 and 500 μm .

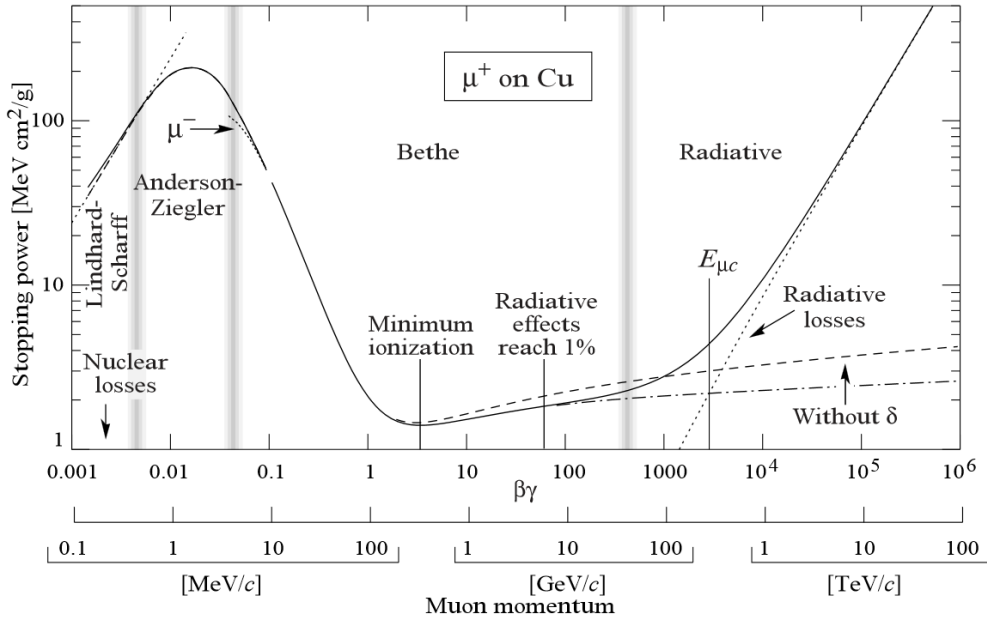


FIGURE 1.7: Energy loss (stopping power) for positive muons in copper as a function of $\beta\gamma = p/Mc$ [19].

than those with large energy transfer. High-energetic δ -electrons cause the characteristic tail at the high-energy end of the Landau curve. The main consequence of this asymmetric distribution is that the mean value is not equal to the most probable energy loss.

Silicon strip sensors can be viewed as many reverse biased diodes arranged next to each other. Individual highly doped strips are implanted into a bulk material with lower doping concentration. Thus, the depletion region can expand into the whole bulk, which is then essentially free of excess charge carriers. When a charged particle passes through the silicon strip sensor, it interacts with the material as described by the Bethe-Bloch formula and creates electron-hole pairs along its track (Figure 1.8). The created charge carriers are taken up by the electric field that is applied in reverse biased mode and drift toward the electrodes. The resulting motion of the charge carriers induces a signal at the strips closest to the track of the passing particle and such allows the spatial resolution of the track.

For a silicon strip sensor the signal induced by the charge carrier drift on an individual electrode can be obtained by calculating the weighting field of the respective electrode and applying the Shockley-Ramo-Theorem [21]. The weighting field $\vec{E}_{w,i}$ of electrode i is obtained from the weighting potential $\phi_{w,i}$ of that electrode by expressing the total potential of all involved electrodes

$$\phi_0(\vec{r}) = \sum_{i=1}^k \phi_i(\vec{r}) \quad (1.13)$$

as a superposition of the individual electrode potentials ϕ_i and setting all electrode potentials to zero but for the electrode i , which is set to $\phi_i = U_i$. The

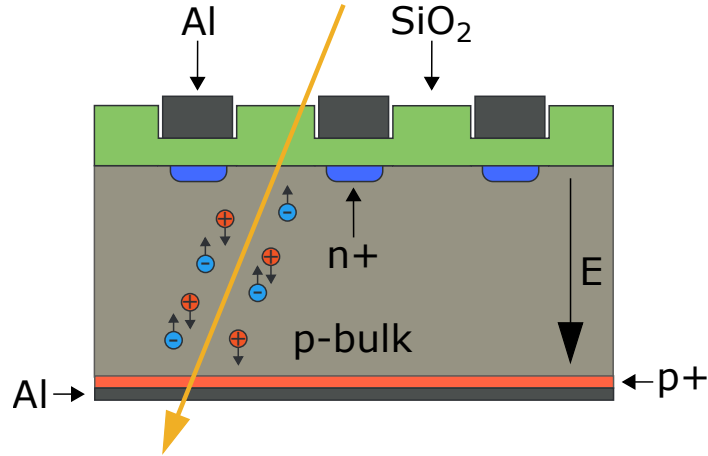


FIGURE 1.8: Electron-hole pairs created in the depleted bulk by a charged particle passing through the silicon strip sensor. The electric field causes the charges to drift toward the electrodes.

weighting potential and the weighting field then become

$$\phi_{w,i}(\vec{r}) = \frac{\phi_i(\vec{r})}{U_i}, \quad \vec{E}_{w,i} = -\vec{\nabla}\phi_{w,i}. \quad (1.14)$$

The weighting field only depends on the geometry of the configuration and determines the signal induced on the electrode i through the charge carrier drift with the resulting signal current

$$i_{S,i} = q\vec{E}_{w,i}\vec{v}. \quad (1.15)$$

Here q is the charge that drifts in the field and \vec{v} is the drift velocity.

The amplitude of the signal is determined by the number of generated electron-hole pairs. When assuming the excess charge carriers were only created by MIP ionisation, this number can be estimated by considering the total energy deposited in the material according to the Bethe-Bloch formula and dividing it by the mean energy necessary to create an electron-hole pair. For silicon the mean ionisation energy is 3.6 eV [17], which results in about 22500 electron-hole pairs created in a standard silicon sensor of 300 μm thickness [22]. However, the intrinsic charge carrier density for silicon is several orders of magnitude larger. To achieve a sufficient signal-to-noise ratio, it is therefore absolutely essential to remove the excess charge carriers, which is why silicon sensors are operated as p-n junctions in full depletion.

1.5.2 Radiation Damage

Silicon sensors like the ones used at the CMS tracker are under constant radiation stress due to the high particle flow in high-energy physics experiments. In respect of the planned upgrade of the CMS experiment and the increase of the LHC luminosity (see section 1.3.2), the CMS collaboration has conducted an extensive measurement campaign to determine a favoured silicon material and design to fulfil the requirements of the CMS tracker at the High-Luminosity LHC [23]. During this campaign it was found that, although

n-type base material showed higher signals under medium irradiation, p-type material exhibited overall preferable properties also for higher radiation fluences. Thus, the new sensors for the CMS tracker will be n-in-p type instead of p-in-n, which is in use for the current tracker.

However, also n-in-p type sensors are affected by radiation. Specifically, the separation of the individual strips is a problem. It requires additional measures to be taken to allow the sensor to function properly. In order to motivate this specific feature of n-in-p type sensors and to provide a basis to understand radiation damage in silicon sensors, in the following a short overview over the topic is given with an emphasis on the process that affects strip separation in n-in-p type sensors. An in-depth analysis of radiation defects in silicon detectors is given in [14].

Generally, radiation can interact with the electrons of the detector material or with the atoms of the lattice. These interactions have different impact and such also result in different kinds of damage to the material. One can distinguish surface damage and damage to the detector bulk.

Incoming particles that interact with the lattice atoms through elastic scattering can dislocate them from their positions. This is the main process responsible for defects in the silicon bulk. Depending on the energy transferred to the primary knock-on atom (PKA), the resulting defects can be point-like or extend to a larger cluster of atoms. Generally, these lattice defects create energy levels in the band gap between valence band and conduction band. Depending on their position, these energy levels have different effects. Shallow energy levels (close to the band edges) can act as donors or acceptors, and thus cause a modification of the effective doping concentration, which leads to a shift of the depletion voltage. Deep energy levels, on the other hand, can act as traps for charge carriers, affecting the charge collection efficiency of the sensor device. Additionally, the newly introduced energy levels can also make it easier for electrons and holes to be thermally excited, which results in an increased leakage current. This kind of bulk damage is mainly caused by massive particles such as neutrons, protons and pions.

Photons and charged particles, on the other hand, most importantly cause surface damage in silicon sensors. They mainly interact with the electrons of the atomic shell, generating excess charge carriers through ionisation. These effects are the principle for particle detection in the sensor, and, as such, are mostly reversible. However, in the amorphous oxide on top of the sensor and for detector electronics, which are also mainly made out of silicon, these excess charges pose an issue. Because of the isolating properties of the oxide, the charge carriers cannot disappear and build local concentrations of charge inside the oxide (Figure 1.9a). The positive oxide charges in the SiO₂ passivation layer attract free electrons from the silicon bulk. Thus, an accumulation layer of electrons forms at the interface of passivation and bulk between the strip implants. In the n-in-p configuration this effect causes the n⁺-strips to no longer be properly isolated from each other.

1.5.3 P-Stop Strip Separation

Strip isolation is important to ensure the resolution capabilities of a silicon strip sensor. If the individual strips are not well isolated from each other, the charge created by a passing particle will spread over many strips, and it will

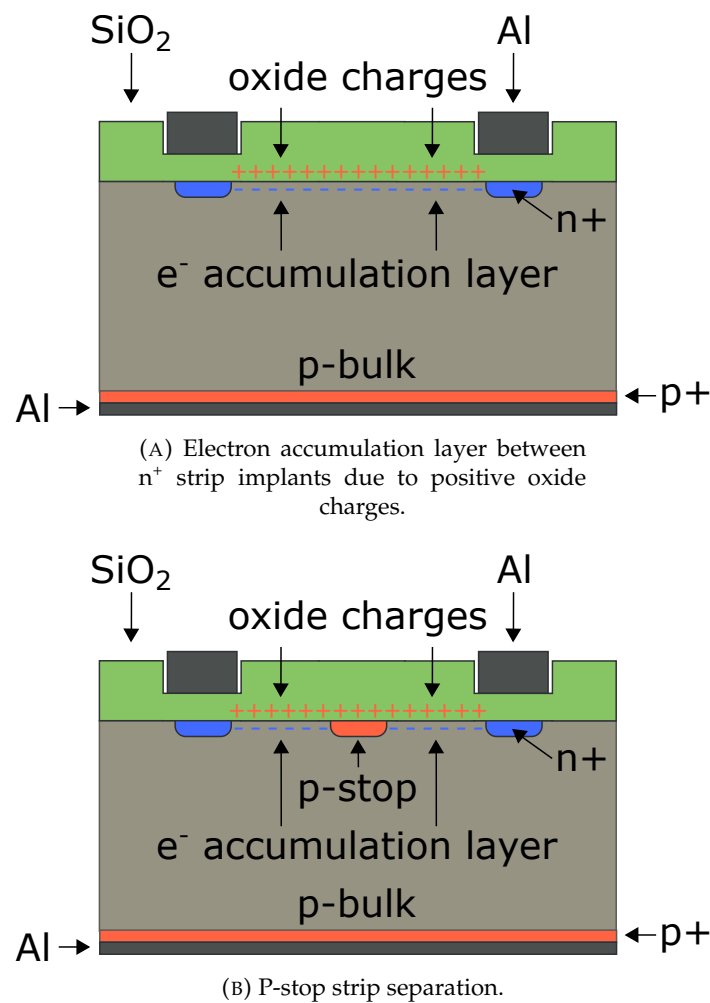


FIGURE 1.9: Electron accumulation layer forming between n⁺ strip implants in an n-in-p sensor due to positive oxide charges. A p-stop implant is added to interrupt the accumulation layer and increase the inter-strip resistance.

not be possible anymore to determine the initial position of the particle. Thus, the position resolution will be lost.

The electron accumulation layer that forms between the n⁺-strips of n-in-p sensors prevents proper strip isolation. Therefore, additional measures have to be taken to separate the individual strips from each other. Ultimately, the electron accumulation layer between the strips must be interrupted by a suitable structure that needs to be incorporated into the sensor.

Usually p⁺-implants are added between the n⁺-strips (Figure 1.9b). These so-called *p-stop* structures surround every strip so that again an inter-strip resistance in the order of magnitude of GΩ can be reached. Different configurations of p-stop layers are possible, varying in thickness and number of implants between the strips. The suitable layout has to be chosen according to the application and respective sensor specifications, considering isolation and charge-collecting properties as well as behaviour under irradiation.

It is also possible to introduce a layer of low intensity p-doping on the entire surface of the silicon bulk and the implanted strips. This so-called *p-spray*

method does not require an additional photo lithography step during manufacturing like the p-stop variant, but its performance suffers under strong irradiation.

Additionally, electric field plates can also be employed to shape the electric field between the strips. A simple example would be an aluminium field plate on negative potential between the readout strips that interrupts the electron accumulation layer. Also, large overhangs of the aluminium readout lines over the n^+ -implants can be used to act as field plates. This method is somewhat more elaborate, since it requires an additional voltage source, and, in case of the aluminium overhangs being used as field plates, the readout electronics need to cope with the shifted operation potential [24].

1.5.4 Sensor Design

Silicon strip sensors are built to detect particle tracks with high spatial resolution. For this purpose the distance between the strips has to be sufficiently small, and, generally, each of the many strips needs to be read out individually. For this to work the strips need to be well isolated from each other. Additionally, high signal-to-noise ratio, high breakdown voltage, low leakage current, and a well-defined electric field are all desirable qualities of a good sensor. Industrial silicon strip sensors comprise different structures to meet these requirements (Figure 1.10).

The basic raw material for the production of silicon sensors are high-purity silicon wafers. These are thin slices cut from silicon ingots, which are usually manufactured using the Float-Zone process [25]. They contain only a small amount of impurities, ensuring a high resistivity of the material. The surface of the raw wafer is structured using a photo lithographic process and the sensor structures are subsequently introduced into the wafer in many production steps, including edging techniques, thermal diffusion or ion implantation for doping, and sputtering techniques to apply the metallic contacts. In the end the wafers are cut (diced) to acquire the individual sensors.

Essentially, a sensor is made up of lightly p-doped silicon bulk material with strips with high donor concentration (n^+) implanted on the front side (see Figure 1.8 for comparison). Since the sensors should be fully depleted to ensure a good signal-to-noise ratio, a high resistivity of the bulk material is desirable as it corresponds to a low full depletion voltage. The high difference in impurity concentration between bulk and implants (several orders of magnitude) ensures that the depletion region will expand farther into the p-bulk than into the n^+ -strip. The highly doped p^+ -layer at the backside of the sensor ensures a good ohmic contact with the aluminium backplane, which serves as one of the biasing electrodes.

The pitch between the strips typically varies between 50 and about 100 μm and is very important for the achievable position resolution of the sensor. For sensors with digital readout the possible position resolution can be calculated depending on the strip pitch p with

$$\langle \Delta x^2 \rangle = \frac{1}{p} \int_{-p/2}^{p/2} x^2 dx = \frac{p^2}{12}, \quad (1.16)$$

where x is the position of the particle track [17]. This resolution can be improved when analogue readout is used. When the strips are close enough to

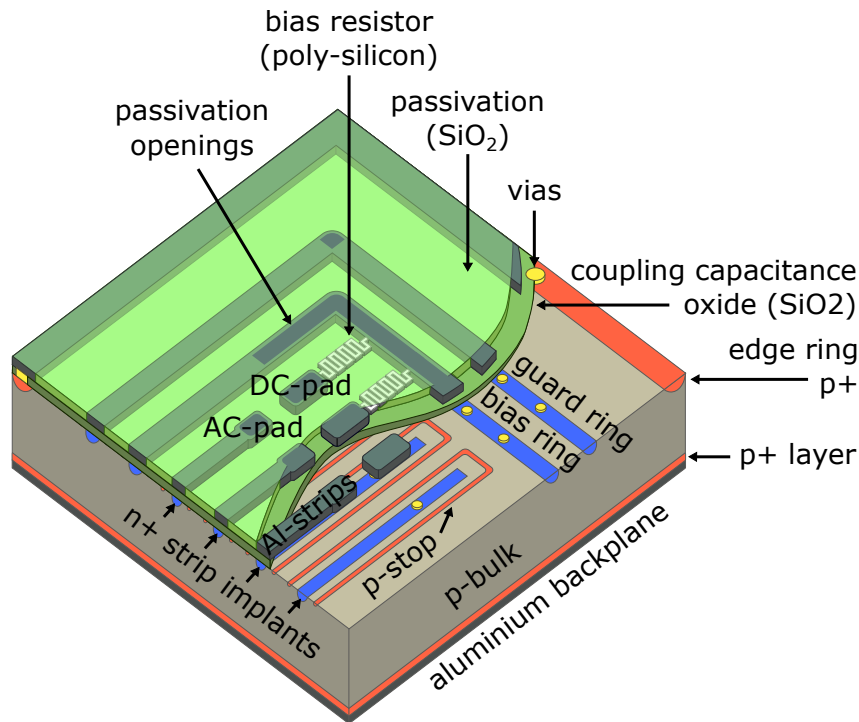


FIGURE 1.10: Schematic 3D view of an n-in-p silicon strip sensor.

each other so that the charge deposited by a traversing particle gets taken up by more than one strip (due to diffusion of the charge carriers), the coordinate can be found by interpolation, e.g., by calculating the centre of gravity of the signal.

The generated signal can be transmitted to readout electronics in essentially two ways. Either the aluminium readout strips are directly contacted to the strip implants (DC coupling), or they are only indirectly connected via a coupling dielectric in-between (AC coupling). In case of DC coupling the leakage current is transferred to the amplifier along with the actual signal. This method is therefore only suitable for systems with very low leakage current, like the very small structures of pixel sensors. For silicon strip sensors the leakage current is usually considerably larger, and because of this, AC coupling is used. Here a dielectric is introduced between the strip implants and the aluminium strips, which are then only capacitively coupled. This separates the DC biasing circuit from the AC signal circuit, and the leakage current is blocked from the amplifier. The coupling dielectric is applied on the whole sensor between the doped surface and the metal readout and biasing structures. For the DC circuit a via (vertical interconnect access) connection is established through the coupling dielectric. Usually silicon dioxide (SiO_2) is used as dielectric, but it is also possible to add materials like silicon nitride (Si_3N_4) or to use compositions of different materials to improve the properties of the dielectric.

Biasing of the sensor is done via the bias ring, with the aluminium backplane serving as the second electrode. The bias ring is an n^+ -implant covered by a layer of aluminium. It surrounds all the strips and is connected to each one via a polycrystalline silicon resistor. The poly-silicon resistors serve to

keep all the strips on the same potential as the bias ring and to control the flowing current.

To obtain a uniform, well-defined depletion region inside the sensor, a layer of p^+ , the edge ring, is implanted at the outer edges of the sensor, surrounding the entire device at the upper edge. Since both, backside and bulk, are p^+ - and p -doped respectively, an ohmic connection is established between the edge ring and the backplane, ensuring that both structures are on the same potential. This prevents the depletion region from growing all the way toward the edges of the sensor, where crystal impurities would otherwise cause a significantly increased leakage current.

An additional measure to shape the electric field inside the sensor and, as such, help to increase the breakdown voltage of the sensor, is the so-called guard ring. It is essentially another n^+ -doped ring structure surrounding all the strips as well as the bias ring. Thus, it regulates the potential difference between bias and edge ring, and prevents high electric fields near the surface of the sensor, where otherwise electrical breakdown would occur.

In addition to the above mentioned structures, a passivation layer covers the entire sensor on top. It protects the sensor from environmental influences and damage and serves as electrical isolation. Usually materials like silicon dioxide (SiO_2) or silicon nitride (Si_3N_4) are used, but also phosphor silicate glass (PSG) is a possible material [18].

To bias the sensor and to connect it to readout electronics, openings are etched into the passivation layer, making it possible to bond the sensor or to directly contact the aluminium structures, using probe needles. The AC pad at each strip is used to read out the AC coupled signal of the strip, while the DC pads are used to perform quality tests on the individual strips. The biasing of the sensor is possible via the passivation openings above the bias ring.

Chapter 2

Prototype Sensors and Test-Structures

For the CMS Phase II upgrade n-in-p type silicon strip sensors will be used because they exhibit an overall better performance under high radiation exposure than the currently used p-in-n sensors. Various development steps are necessary to provide CMS with the needed sensors and to meet the specifications set by the collaboration. The Institute of High Energy Physics (HEPHY) in Vienna works together with semiconductor manufacturers to develop these new silicon strip sensors for the CMS tracker. In particular, two manufacturers are considered within the scope of this thesis, the Japanese vendor *Hamamatsu Photonics K. K.* and the Austrian company *Infineon Technologies Austria AG.*

A number of prototype sensors have been manufactured and tested, and the results they show are in general very encouraging [18, 26, 27]. However, the research is still ongoing; new manufacturing runs will be conducted, and subsequently the produced sensors will be investigated.

This thesis focuses on a specific test-structure that is manufactured together with the main sensors, specifically to investigate the properties of the p-stop layer incorporated in the sensors for strip isolation. In the following sections a short description of the general wafer layout and test-structures will be given, with emphasis on the p-stop test-structure that was used for all investigations presented in this thesis.

2.1 Wafer Layout

Both, the wafers from Hamamatsu and Infineon, comprise prototypes of the main sensors, as they are planned to be used in the new CMS tracker, in the centre and many additional sensors and semiconductor structures in the wafer periphery (Figure 2.1). The wafer layout and parameters vary slightly for each vendor, with the main difference being that the Infineon sensors are processed on 8-inch wafers instead of on the more common 6-inch variant (Table 2.1).

TABLE 2.1: Important parameters of the wafers housing the investigated test-structures.

Manufacturer	Wafer diameter	Physical thickness (μm)	Active thickness (μm)	Resistivity ($\text{k}\Omega\text{ cm}$)
Hamamatsu	6"	320	240	~ 3
Infineon	8"	200	200	~ 7

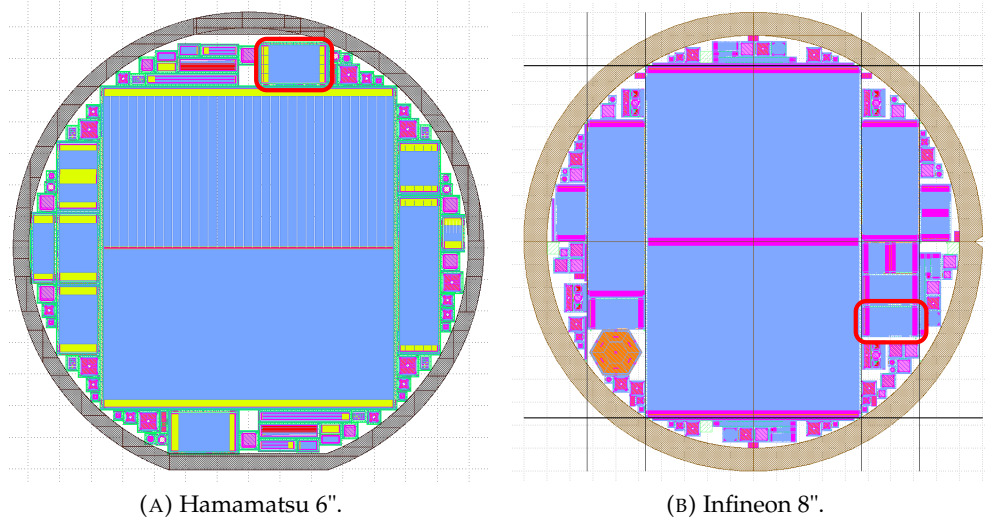


FIGURE 2.1: Schematic wafer layout based on the GDS layout file with main sensor in the centre and test-structures and smaller sensors in the periphery. The P-Stop-GEO sensor is highlighted in red on each wafer.

This change in wafer size is due to the increased cost efficiency that comes with larger wafers and strives to meet the standards of the semiconductor chip industry, where production on even larger 12-inch wafers is already state-of-the-art [27].

2.1.1 Test-Structures

To make use of the full size of the wafer, the main prototype sensors are placed in the centre, and smaller structures and sensors are arranged around them. These so called *test-structures* are used to perform quality tests and to investigate properties of the sensors that cannot be accessed directly on the main devices or require destructive processes to be measured. Since the test-structures are treated identically to the main sensors during production, it is assumed that they exhibit the same properties and possible weaknesses. It is therefore also feasible to monitor the production process using test structures.

In addition to the test-structures at the edges of the wafer there are also a number of smaller prototype sensors arranged around the main sensor in the centre. These small sensors are used to, e.g., perform irradiation tests and to investigate the influence of different sensor layouts.

2.2 The P-Stop-GEO Sensor

The structure that was investigated for this thesis is one of the small sensors located next to the main sensor on the processed wafers. It is called the *P-Stop-GEO* test-structure and comprises 120 individual strips that are arranged into four distinct regions (Figure 2.2). Each region consists of 30 strips with a pitch of $90\ \mu\text{m}$. The individual strips are embedded in a ring-like p-stop structure each, with an additional layer of p-stop surrounding every 30-strip section on the outside. This so-called “atoll” configuration is the standard p-stop pattern

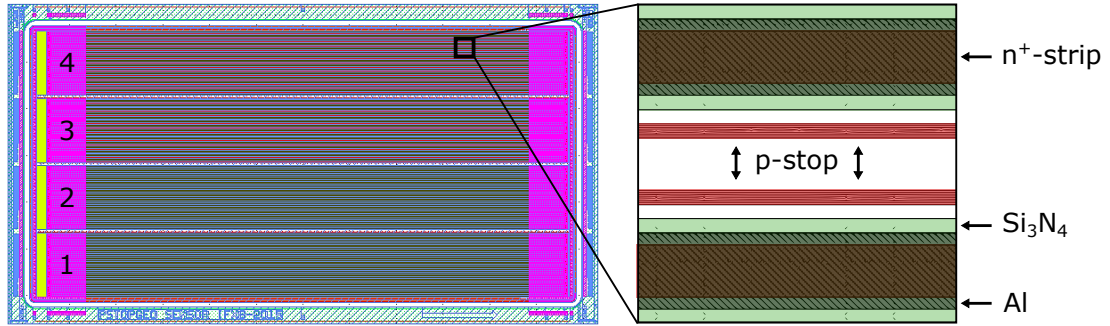


FIGURE 2.2: Schematic view of the Infineon P-Stop-GEO sensor with highlighted strip structure. Each of the four sensor segments exhibits a different p-stop layout. The Hamamatsu variant is identical but for subtle design differences.

TABLE 2.2: Dimensions of the p-stop layout for the P-Stop-GEO sensor for both, Hamamatsu and Infineon prototypes. The numbering of the sensor sections corresponds to the one indicated in Figure 2.2.

Manufacturer	Section number	P-stop thickness (μm)	P-Stop spacing (μm)
Hamamatsu	1	8	2
	2	4	20
	3	4	26
	4	8	18
Infineon	1	8	4
	2	8	18
	3	6	16
	4	6	22

nowadays. Compared to other configurations it has shown the best results in past tests, providing high signals and a high signal-to-noise ratio before as well as after irradiation [24]. As a consequence of the atoll configuration two layers of p-stop implantations come together in the inter-strip region, with an area of non-implanted bulk material in between.

In each sensor section a slightly different variant of the p-stop layout has been implemented (Table 2.2). The variable layout parameters are the thickness of the p-stop implants, denoted as “p-stop thickness”, and the distance of the p-stop ring from the strip. For an easier labelling, in this thesis the last parameter is expressed as the distance between the two p-stop implants in the inter-strip region and denoted as “p-stop spacing”.

With this configuration it is possible to study the influence of the p-stop layer on the signal and charge distribution in the sensor. In the context of this thesis parameters like charge sharing between adjacent strips and charge loss attributed to the p-stop layer have been investigated, to provide an insight into the role of the p-stop layer for these sensor parameters and to help point out a favourable layout for future applications.

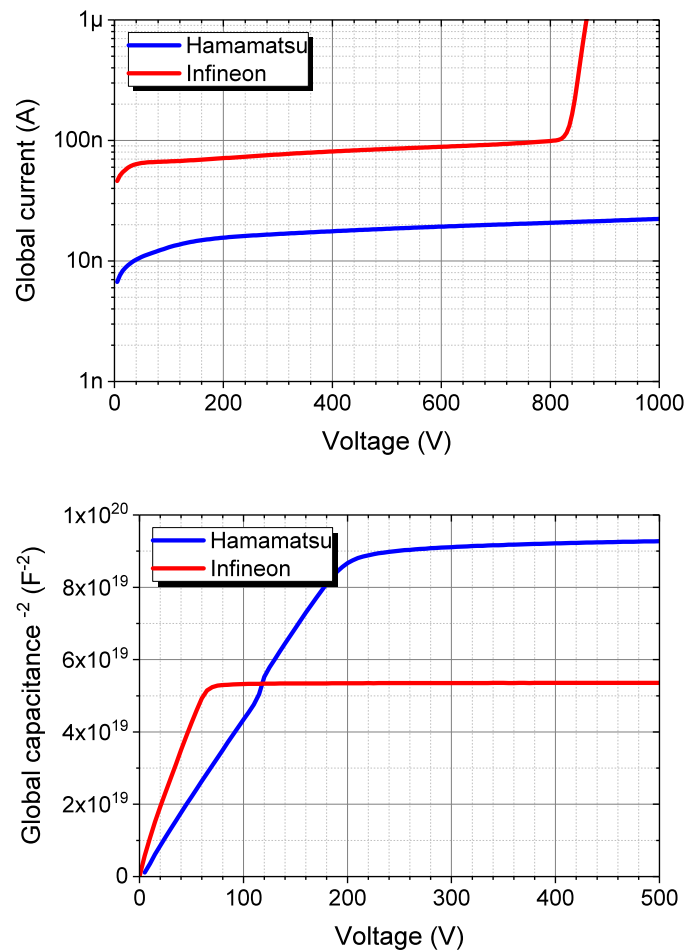


FIGURE 2.3: Global parameters of the two investigated P-Stop-GEO sensors from Hamamatsu and Infineon.

2.2.1 Electrical Characterisation

The two sensors that were used for the measurements as part of this thesis are the P-Stop-GEO sensors VPX18592_04 from Hamamatsu Photonics K. K. and VE525852_02 from Infineon Technologies Austria AG. Here the last number indicates the wafer that initially housed the sensor. To characterise the sensors prior to the investigations regarding the p-stop structure, electrical properties and characteristics were measured. A description of the measurement procedure and the various measured quantities can be found in [18].

The global current-voltage and capacitance-voltage characteristics (Figure 2.3) generally show no unexpected abnormalities. It can be noted that the Infineon sensor draws more current than the Hamamatsu model. Diode breakdown and with it the rapid increase of the current happens at slightly above 800 V for the Infineon sensor, whereas the Hamamatsu sensor remains stable over the measurement range of 1000 V. From the capacitance-voltage characteristics the full depletion voltages for both sensors can be determined. For the Hamamatsu sensor full depletion is reached at approximately 200 V, while the Infineon model is fully depleted at about 75 V.

Additionally, to detect possible defects in the sensor and potentially “bad”

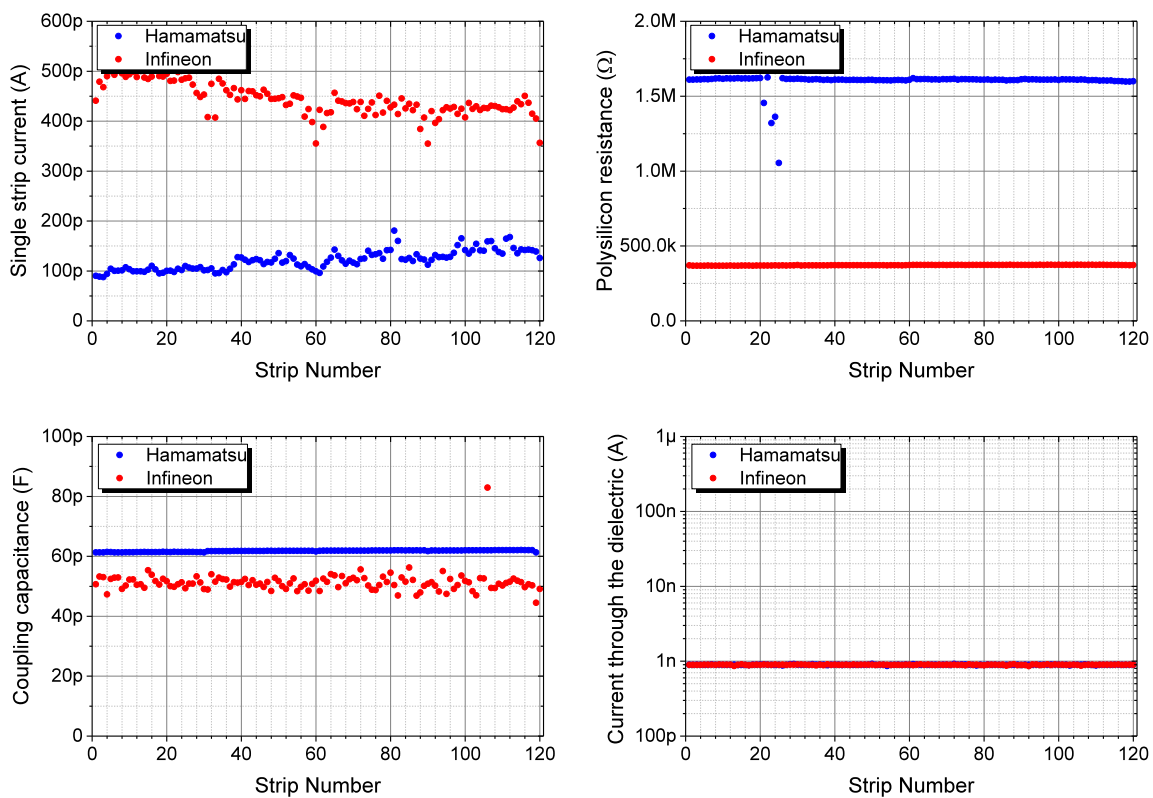


FIGURE 2.4: Single strip parameters of the two investigated P-Stop-GEO sensors from Hamamatsu and Infineon.

strips, important single strip parameters were measured (Figure 2.4). Here, too, no obvious damages or conspicuous behaviour could be noted. Generally, a good sensor should show uniform parameters over its whole area. The single strip leakage current should be sufficiently small, while the poly-silicon resistance as well as the coupling capacitance of each strip should be considerably large. All of these specifications are met by both sensors. The current through the dielectric is measured to detect shorts between the strip implant and the aluminium layer. These so-called pinholes would drastically increase the drawn current and as a result overload the amplifiers when connected to electronic readout. Measuring the current through the dielectric with a compliance value of 100 nA, no pinholes were detected, neither for the Hamamatsu sensor nor for the Infineon one. Hence for both sensors all the strips seem to work fine and can be read out.

Chapter 3

Experimental Sensor Characterisation

3.1 The Laser Test Stand in the HEPHY Clean Room

All measurements within the scope of this thesis were conducted at the laser test stand in the HEPHY clean room (Figure 3.1). The main component of the test stand is a light-tight metal box that contains a pico-second diode laser source¹ (Table 3.1) and an x-y-z table, onto which the device under test can be mounted. The x-y-z table consists of an x-y stage and a height-adjustable arm that covers the z-direction. Both components can be controlled via a LabVIEW software and together allow micron-precise movement in three dimensions. The laser source can be operated via the PC as well. Parameters like repetition rate, gain, and trigger mode can be set at a dedicated LabVIEW interface.

The output of the diode laser is passed into a beam splitter, which directs 90 % of the emitted power into a power and energy meter² that allows to continuously monitor the beam power using a photodiode. The remaining 10 % are subsequently transmitted into a single mode fibre, an attached fibre collimator, and a micro focus³ (Table 3.2) and constitute the fraction of the laser power used for sensor testing. Through this system the laser output is focused to reach a minimum beam spot diameter of approximately $4 \mu\text{m}$. To control the power of the laser beam, a variable attenuator with a maximum attenuation of 80 dB was installed before the beam splitter. This way the laser power can be regulated so that the charge generated inside the tested silicon sensor by the laser is comparable to the charge generated by a MIP. For the measurements taken as part of this thesis the attenuator was adjusted such that the power value read out in the power meter after the beam splitter was approximately

¹PiLas gain switched diode laser module PiL106X

²Thorlabs, Laser Power and Energy Meter PM100USB

³Schäfter + Kirchhoff, Micro-Focus Optics 5M-A6.2-03-S

TABLE 3.1: Important parameters of the diode laser system.

Quantity	Value
Wavelength	1055.6 nm
Spectral width	7.8 nm
Pulse width	50 ps
Maximum repetition rate	40 MHz
Maximum pulse energy	8 pJ

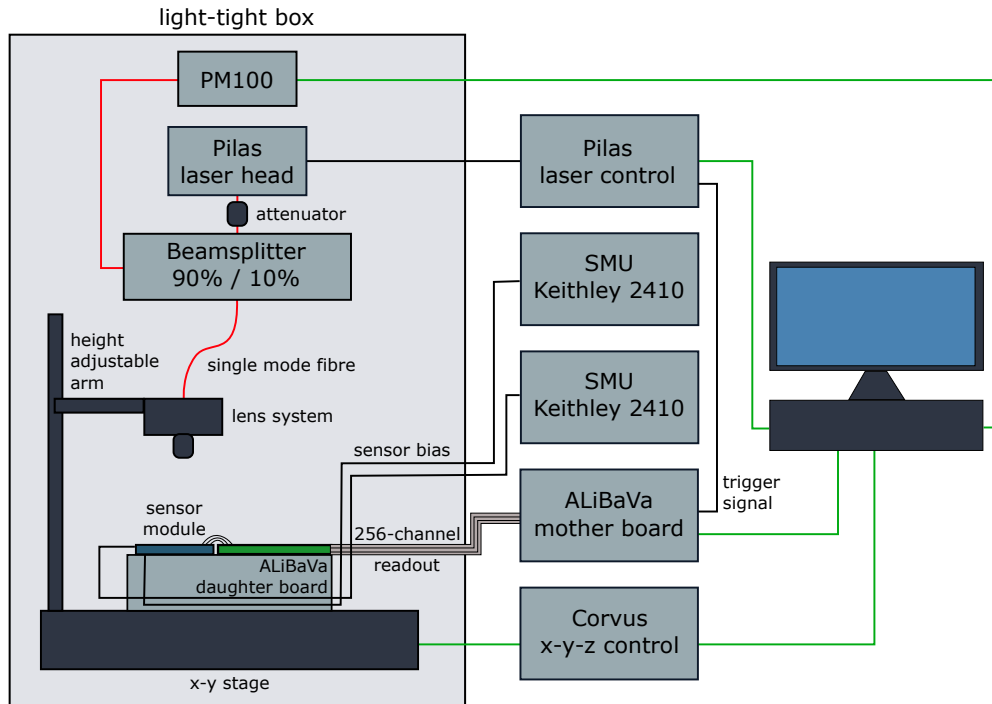


FIGURE 3.1: Schematic visualisation of the experimental setup used to investigate the p-stop properties using the laser system. Optical lines are indicated in red and USB connections in green. Black colour indicates electric connections. For tests with a radioactive source the source can be placed above the sensor module instead of the laser output lens system.

TABLE 3.2: Important parameters of the focusing optics for the diode laser output.

Component	Mode field diameter (μm)	Focal length (mm)	Numerical aperture
Fibre coupling optics	6.2	-	0.14
Fibre collimator	-	11	0.14
Micro focus	-	6.2	0.24

227 pW if the laser was operated in internal trigger mode, with an automatic laser tune value of 37 % and a pulse repetition rate of 1 kHz. The charge that is then generated by the laser in a 200 μm thick sensor corresponds to the charge generated by two MIPs.

Apart from testing with the laser source, the test stand also allows the use of a radioactive source for sensor tests with charged particles. The radioactive source can be placed above the device under test by an adjustable arm and thus replaces the laser as the source of charge generation inside the sensor material.

To provide the bias voltage for the sensors under test, up to two source measure units⁴ (SMU) were used, but in most cases the system was operated with just one sensor biased. The sensors are read out using the *ALiBaVa system* [28, 29, 30], which allows an automated readout comparable to the systems

⁴Keithley 2410

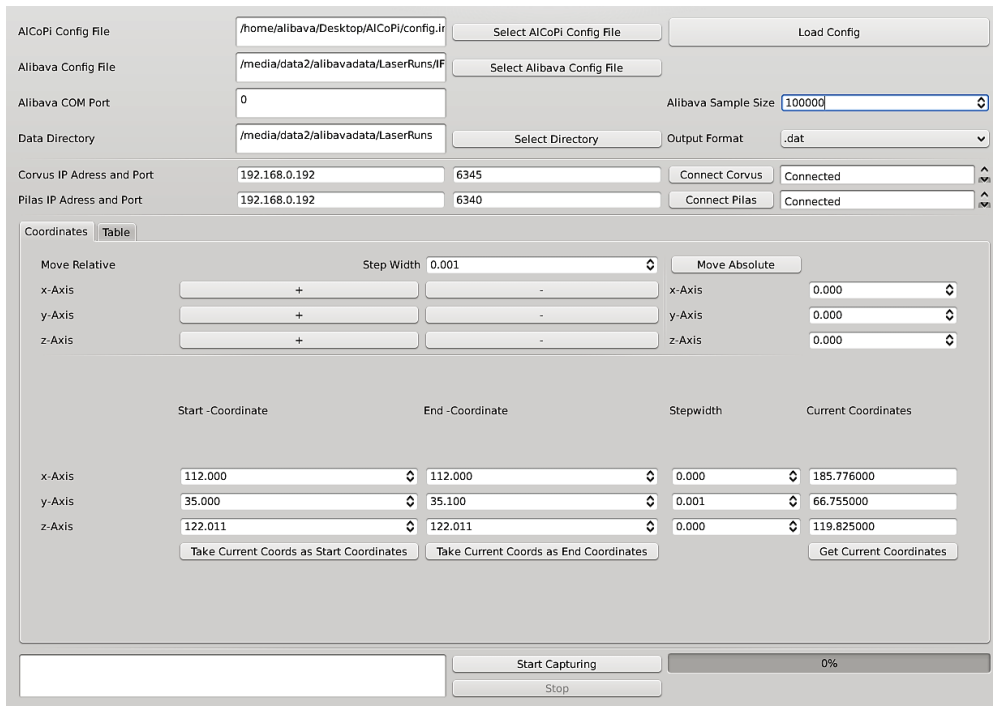


FIGURE 3.2: Graphical user interface of the AlCoPi Python programme for automatic laser scans with the ALiBaVa system.

used in LHC experiments (see section 3.2).

Data taking with this system has been automated by a Python programme⁵ that was home-made at the institute. This interface centralises the communication to the x-y-z stage, the laser, and the ALiBaVa readout (Figure 3.2). Thus, the laser can be automatically scanned along the sensor, and for each point of the scan data can be read out and saved.

3.2 The ALiBaVa Readout System

The ALiBaVa system [28, 29, 30] is a portable readout system designed for the experimental characterisation of silicon micro-strip sensors. It is developed and distributed by a collaboration between the *University of Liverpool*, the *Centro Nacional de Microelectrónica (CNM)* in Barcelona, and the *Instituto de Física Corpuscular (IFIC)* in Valencia, which together constitute the ALiBaVa collaboration⁶.

The main strength of the system, and the reason why it has developed to something like a “quasi-standard” in high-energy physics detector development, is that it employs the Beetle readout chip [31], which was developed for LHCb, and, as such, provides a configuration that is very similar to those used in LHC experiments. Furthermore, because of its portability and its various operation modes, the system also facilitates the comparability of experiments carried out at different locations and by different research groups.

As part of this thesis a newly purchased ALiBaVa system was set up and commissioned to work with the laser test stand in the HEPHY clean room and

⁵AlCoPi: ALiBaVa, Corvus, PiLas

⁶ALiBaVa collaboration: A Liverpool Barcelona Valencia collaboration

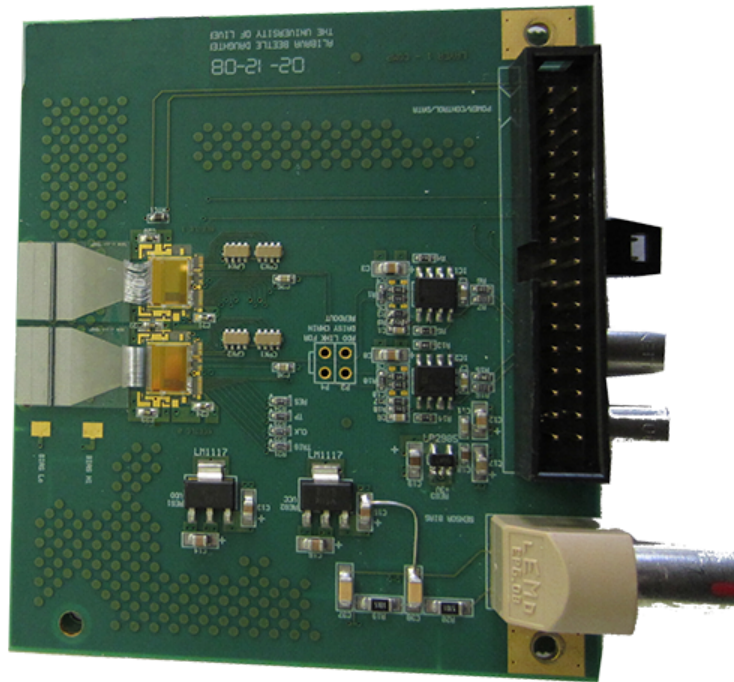


FIGURE 3.3: ALiBaVa daughter board with front-end Beetle readout chips and fan-ins on the left. The connectors for the multi-wire planar cable to the mother board and the LEMO high-voltage sensor bias are located on the right [28].

to gain the knowledge necessary to utilise the system for future experiments. In the course of this work various macros for offline data analysis were written using the ROOT framework [32].

3.2.1 Hardware Components

The ALiBaVa system measures the charge generated in silicon strip sensors by reading out up to 256 individual detector channels at the same time. Its main hardware components are a small daughter board and a larger mother board.

Daughter Board

The daughter board (Figure 3.3) is the direct connection to the investigated sensors. It houses the electronic front-end readout chips, a temperature sensor, and fan-ins to wire bond the sensor strips to the Beetle input channels. The high-voltage for the silicon sensors is supplied directly to the daughter board. The Beetle chips are operated in analogue readout mode. A flat-band cable transfers the data from the daughter board to the mother board. This way the mother board electronics can be kept out of the potentially harsh, radiation exposed environment close to the sensors.

Mother Board

The mother board (Figure 3.4) digitises and processes the signal and communicates with the PC running the system software. For this purpose it houses a

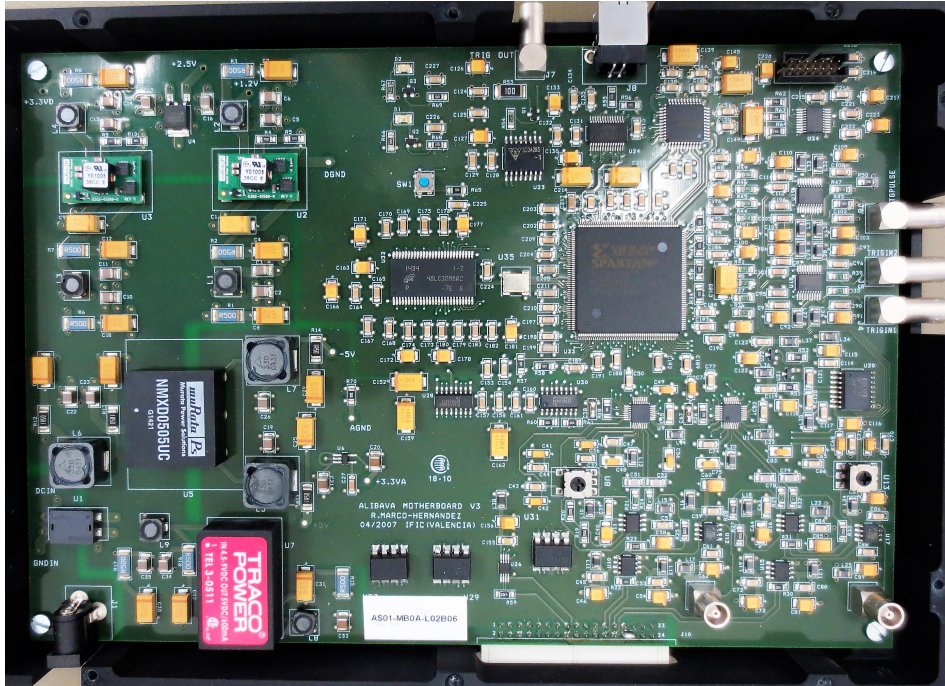


FIGURE 3.4: ALiBaVa mother board encased in a protective frame. The various components and connectors are specified in [33].

10 bit analogue-to-digital converter (ADC) and a field-programmable gate array (FPGA) that interprets and executes the orders of the software application. Additionally, the mother board can send and receive internal and external trigger signals to, e.g., trigger a laser output or work with a radioactive source.

Trigger Board

In addition to the standard daughter and mother board the ALiBaVa collaboration also provides a trigger board for measurements with a radioactive source. Since particles from a radioactive source are generated at random during the decay process, an external trigger is required to tell the data acquisition system when a particle has passed through the sensor. For this purpose the ALiBaVa trigger board incorporates a silicon diode sensor. The trigger board requires a 5 V power supply and a bias voltage of 80 V for the silicon diode sensor. Its design is matched to that of the daughter board so that it can be mounted below the daughter board onto the same metal frame and the sensitive surface of the diode is well aligned below the bonded strip sensors. When a particle passes through one of the silicon strip sensors under test, it also hits the diode below and a transistor-transistor logic (TTL) trigger signal is generated that is transferred to the mother board. It starts the data acquisition if the trigger exceeds a predefined level.

3.2.2 Operation Modes

ALiBaVa provides different operation modes so that it can be used with different laboratory setups. Mainly these are the laser mode and the radioactive

source mode, but the ALiBaVa system also provides a mode to calibrate the signal and one to take pedestal runs. In the following the different run types are described briefly.

Signal Calibration

For signal calibration the Beetle chips can inject an electric pulse with a defined amplitude into all the channels such that gain and offset of the characteristic curve of the preamplifier for each channel can be determined. Thus, the ADC response to a charge pulse can be converted into the equivalent number of electrons that would generate that specific signal. The amplitude of the charge pulse can be scanned with a minimum step size of 1024 electrons and a maximum number of 255 steps.

Aside from the pulse amplitude, also the strobe delay of the calibration pulse can be scanned. With this method the pulse shape can be recreated in a range from 0 to 255 ns and a minimum step size of 1 ns. In order for the calibration scan to yield a sensible result, the strobe delay has to be set to the pulse maximum.

Pedestal Run

A certain level of ADC counts is always read out, even if no input signal is present. This so-called pedestal must be known in order to correctly interpret the signals measured with the system. ALiBaVa provides the possibility to perform a dedicated pedestal run before the actual data acquisition to determine this systematic ADC level. For this purpose the ALiBaVa mother board sends a tunable number of random triggers to read out the sensors. This way the noise level of the setup and the pedestal can be determined and saved for offline data analysis.

Laser Run

In laser run mode the ALiBaVa mother board sends trigger signals to an external laser source, controlling the laser output with a variable frequency between roughly 450 and 550 Hz. The signal readout is timed with respect to the trigger signals by setting the laser delay to the corresponding value in the ALiBaVa software. For this purpose it is possible to perform a laser synchronisation run, where ALiBaVa measures the signal height as a function of the laser delay. The laser delay should then be set to the value where the peak of the pulse height is observed so that the data acquisition is performed at the correct time. For the described setup in the HEPHY clean room the laser delay was set to 100 ns.

Radioactive Source Run

If the system is operated with a radioactive source, the mother board processes the trigger signals supplied by one or two external trigger sources like the trigger board or, e.g., a scintillator. It starts the data acquisition if the trigger signal exceeds a predefined level. For this purpose there are two different trigger versions to choose from: The first one can process two negative input signals and fires if either one or both signals fall below the set trigger threshold. The second trigger variant uses two thresholds and starts the data acquisition if the

received signal is either below or above both threshold values. For the measurements as part of this thesis the trigger threshold was set such that a trigger signal below -200 mV would start the data acquisition.

Depending on the electronics and the cable lengths used in the setup, there is a certain time delay between the trigger pulse and the maximum of the signal. This so-called trigger latency has to be set to an appropriate value so that the signal is read out at the correct time. For the present setup the trigger latency was set to a value of 133.

3.2.3 ALiBaVa Software

Next to its hardware components the ALiBaVa system also contains a software part that allows to control and customise the data taking by manually adjusting the various parameters. The software runs on Linux, Mac, and Windows based systems, however, it was initially conceptualised for Linux, and when first set up at HEPHY during the course of this thesis, it was found to work much more smoothly on Linux systems. Thus, for all the research conducted and presented within this thesis the ALiBaVa software was run on a Linux machine.

To control the data acquisition using the ALiBaVa software application, a graphical user interface (GUI) is available (Figure 3.5). Here parameters like the number of recorded events per data taking run, laser delay, or Beetle chip parameters can be set, and the run can be monitored with the data displayed in various histograms. The same configurations that are possible with the GUI can also be sent directly via the command line. This feature was used to operate the ALiBaVa system together with the laser source and the x-y-z stage via the AlCoPi Python programme. The data taken with the ALiBaVa system can be stored in two different file formats, a simple binary data format and HDF5 data format. The HDF5 data format simplifies the usage of the data files with programmes based on Python, Matlab or Octave. However, the software provided for data analysis is mainly adapted for the binary data format, which is why this data format was used for all the measurements within this thesis.

3.2.4 Offline Data Analysis

ALiBaVa provides a number of ROOT macros for offline data analysis. During this thesis these macros were extended, and on the basis of the extended macros new macros were written to analyse the data acquired at the laser test stand, with the laser as well as with a radioactive source. The ALiBaVa software and the adapted macros can be found in an SVN repository [34]. In the following a short overview of the general methods of data processing using these macros is given. A more in-depth description of the macros and their functional principle can be found in Appendix A.

The analysis software reads out the data from the binary data format they are stored in, together with a header that contains information about the type of run that was taken, e.g., laser or radioactive source, and the number of recorded events. Then for each event the pedestal is subtracted from the raw signal and a common mode correction is performed (see Appendix A.4). The pedestal can either be calculated from the data with a number of provided algorithms, or it can be taken directly from a priorly recorded pedestal run. When these two possible approaches were investigated, the results obtained

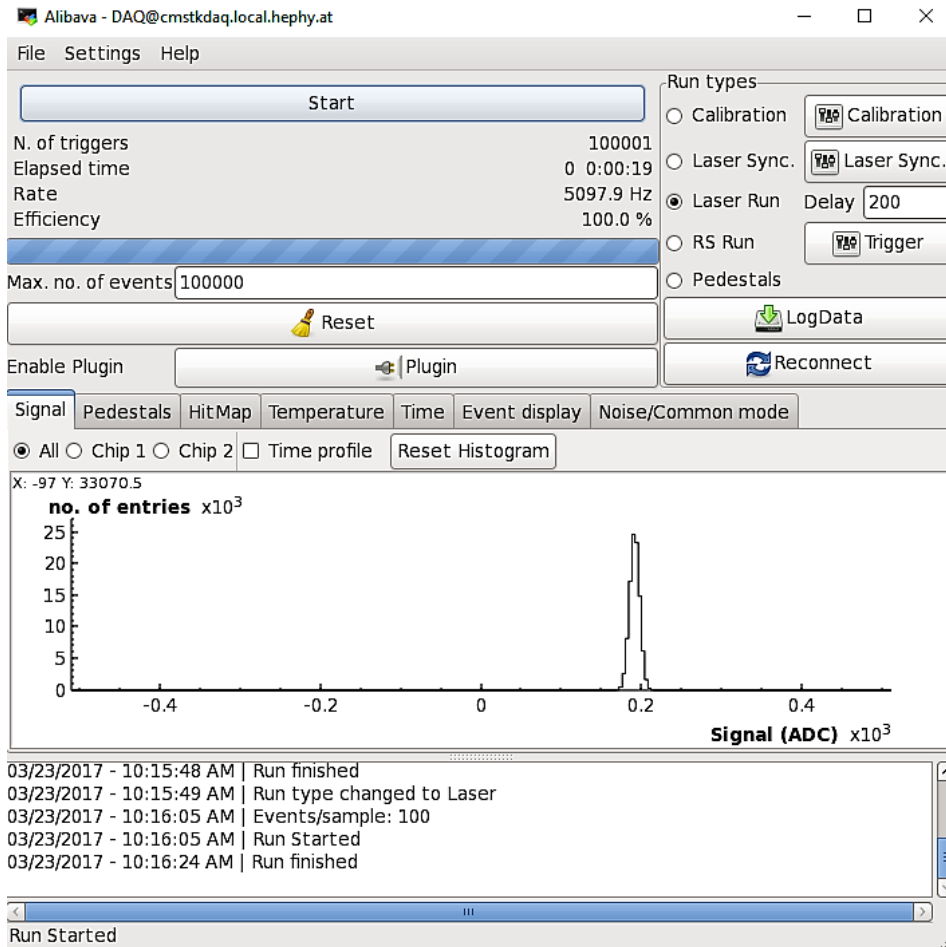


FIGURE 3.5: Graphical user interface provided by the ALiBaVa system.

with the measured pedestals proved to be more trustworthy than the calculated results, which were influenced by the signal present in the data. Because of this, if not indicated otherwise, in this thesis only directly measured pedestals are used for data analysis.

After the initial processing, depending on the demands of the individual experiment, further analyses with, e.g., cluster finding algorithms are possible. Finally, the data can be displayed and stored in various histograms and root-files to, e.g., visualise noise, the hit map, or the signal spectrum and to be able to further work with the data without the need of processing it anew.

3.3 The P-Stop-GEO Sensor Module

The two investigated P-Stop-GEO sensors⁷ are housed next to each other on a custom-made module (Figure 3.6). The module is mounted on a metal framework together with the ALiBaVa daughter board. This construction makes it easier to move the module and also to screw it onto the x-y-z stage to conduct tests with the laser or the radioactive source.

⁷Hamamatsu VPX18592_04, Infineon VE525852_02

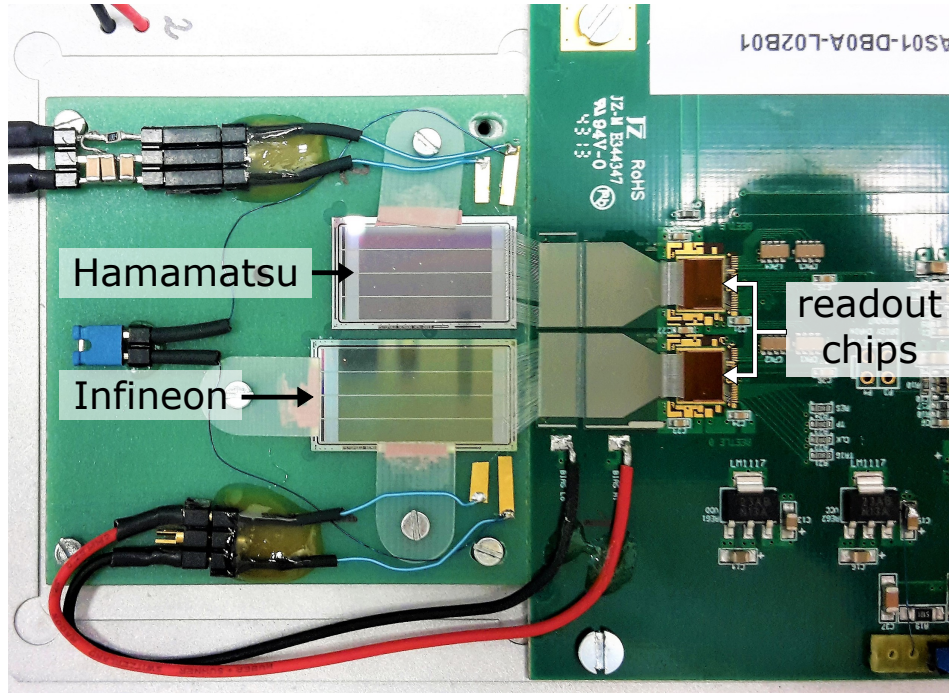


FIGURE 3.6: P-Stop-GEO sensor module with Hamamatsu and Infineon sensors connected to the electronic readout chips on the ALiBaVA daughter board.

To facilitate the bonding to the electronic readout chips and also to fixate the sensors against unwanted shifting, they are placed in specifically cut indentations to line up level with the module surface and fixated with isolating clamps. Each sensor is wire-bonded to one readout chip on the ALiBaVa daughter board such that all 120 strips can be read out, yielding a total of 240 read out channels on two chips. The ALiBaVa readout channels are numbered from 0 to 255. Channels 0 to 127 correspond to the first Beetle chip and are bonded in reverse order to strips 120 to 1 of the Hamamatsu sensor, while channels 128 to 255 correspond to the second Beetle chip and are bonded to strips 120 to 1 of the Infineon sensor. Since the electronic sensor readout provides 256 channels in total, 16 channels are not bonded to any sensor strips (Figure 3.7). These are channels 90 to 97 of the first chip and channels 128 to 135 of the second. Because these channels are left open, they show behaviour different to the connected channels, which has to be considered for the analysis of the read out data.

The bias line for both sensors is integrated into the module as well. The Infineon sensor is biased via the high-voltage port of the ALiBaVa daughter board, while for the bias of the Hamamatsu sensor an additional, custom-built port was included in the sensor module. A low-pass RC filter is incorporated into the bias line of each sensor (Figure 3.8). The Infineon bias line uses the second-order filter included in the ALiBaVa daughter board. It consists of two resistors R of value $5\text{ k}\Omega$ and two capacitors C with capacitance 10 nF each, which results in a cutoff frequency

$$f_c = \frac{1}{2\pi RC} \quad (3.1)$$

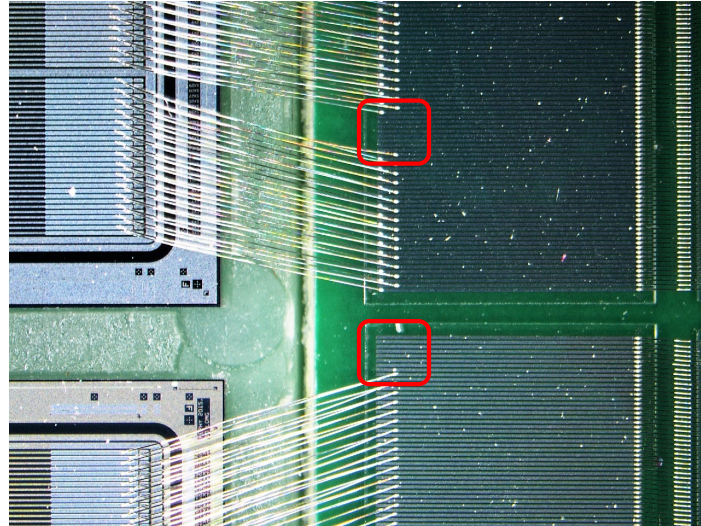


FIGURE 3.7: Microscope view of the wire-bonds from the sensor strips on the left to the pitch-adapters leading to the Beetle chip inputs on the right. Open channels are highlighted in red.

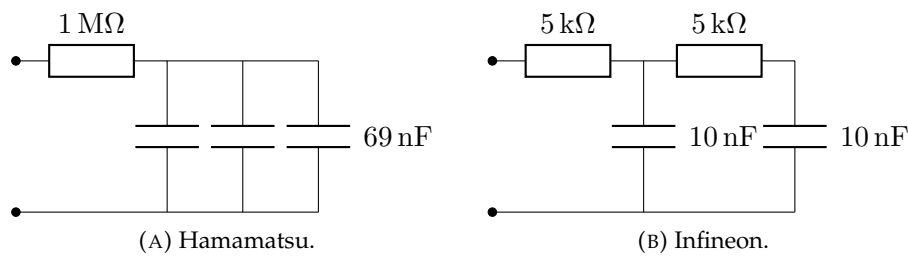


FIGURE 3.8: Schematic of the low-pass RC filters in the bias lines of the investigated sensors.

of approximately 3 kHz . The Hamamtsu sensor, on the other hand, is biased via a custom-made setup that includes a filter built at the electronic workshop of HEPHY. For this configuration a resistor of value $1\text{ M}\Omega$ and three grouped capacitors with a total resulting capacitance of 69 nF were used, yielding a cutoff frequency of 2.3 Hz .

During measurements the sensors are biased at about 20% over full depletion, yielding a bias voltage of 100 V for the Infineon sensor and 250 V for the Hamamatsu sensor. The only exception to this convention is made for radioactive source runs where in addition to both sensors the silicon diode of the external trigger board needs to be biased. This diode can be operated with a bias voltage of up to 80 V . Thus, whenever the trigger diode is in use, bias is provided via the same source as for the Infineon sensor, which in this case is operated only slightly above full depletion at 80 V instead of 100 V .

3.3.1 Noise

Noise is an important factor that has to be considered when looking at the performance of silicon strip sensors. An in-depth description of the various

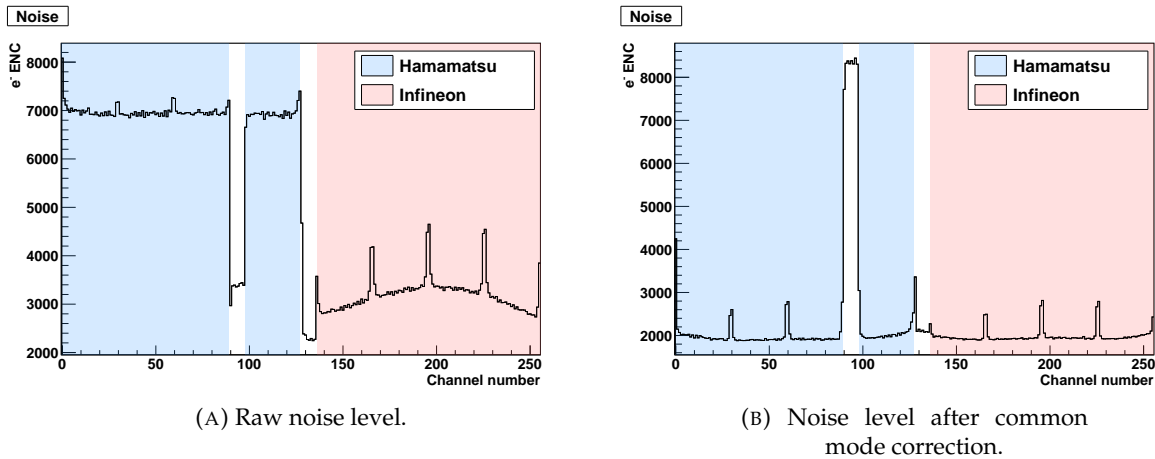


FIGURE 3.9: Equivalent noise charge (ENC) of the readout channels of the P-Stop-GEO sensor module for bias voltages 250 V for the Hamamatsu sensor and 80 V for the Infineon sensor. Channels bonded to sensor strips are indicated in colour. Non-bonded channels with initially low noise levels show disproportionately high values after common mode correction. The periodic peaks with a distance of 30 strips each indicate the higher noise level of strips at the edges of the separated p-stop zones.

sources of noise in silicon strip sensors and the underlying mechanisms can be found in [35].

Generally, the noise observed in the recorded data can be introduced by different sources. One can distinguish noise that is characteristic of a single channel and noise that is observed at a common group of readout channels. Single channel noise is mostly intrinsically related to the front-end electronics or the sensor itself, due to its geometry, faulty processing, defects in the material, etc. and is independent of other channels. However, environmental influences like the pick-up effect of the sensor or instabilities in the bias line or the grounding scheme typically affect a group of neighbouring channels. In the present setup this so-called *common mode noise* causes a coherent oscillation of the 128 channels read by the same front-end Beetle chip.

In order to ultimately achieve a signal that is well distinguishable from the noise background, measures have to be taken to limit the noise. This is done by directly optimising the setup configuration and by subtracting and masking the noise during data analysis.

Looking at the noise of the P-Stop-GEO sensor module two prominent effects can be noted (Figure 3.9): the noise level peaks in periodic intervals every 30 strips and a number of channels show a disproportionately high noise level as compared to the rest when the common mode noise is evaluated and subtracted from the noise signal. The regular peaks in the noise level can be attributed to the strips at the edges of the respective p-stop zones and their neighbours. Here, due to the sensor geometry, the electric field is different than in the centre regions and thus the relevant edge strips usually also have a different capacitance than the rest. All of these effects can lead to a different behaviour of the respective strips, also yielding a higher noise level.

In the common mode corrected noise plot the area of disproportionately

high noise levels results from the non-bonded channels of the Beetle chip. These channels show a significantly lower noise level when only the raw noise is considered. However, the common mode algorithm is naturally written such that it disregards largely discordant values and outliers, which in this specific case leads to an overcompensation for the non-bonded channels. It can be observed that this effect is mostly cancelled out for the non-bonded channels of the chip that reads the Infineon sensor, but is very pronounced for the channels of the chip associated with the Hamamatsu sensor.

The effect of these noisy channels can be observed as non-Gaussian tails in the signal spectra (Figure 3.10). Such noise effects are likely to produce fake hits when the data is analysed. As a result of these observations, the noisy channels, the ones due to edge strips as well as those due to non-bonded channels, were masked by the analysis routine and not included in the data analysis. While this approach eliminates the non-Gaussian tails in the spectra of pedestal runs, the signal spectra of runs with an external source still show non-Gaussian residues (Figure 3.11). Even when all the obviously noisy channels were masked, a considerable amount of fake noise hits could be observed. Fake hits that are produced at random channels are less likely to affect the signal at one individual channel, but they have a considerable impact on the channel collective. Thus, the effect of fake hits is especially relevant for runs with the radioactive source, since there a collective of channels must be considered, while for tests with the infrared laser mainly individual channels are of interest.

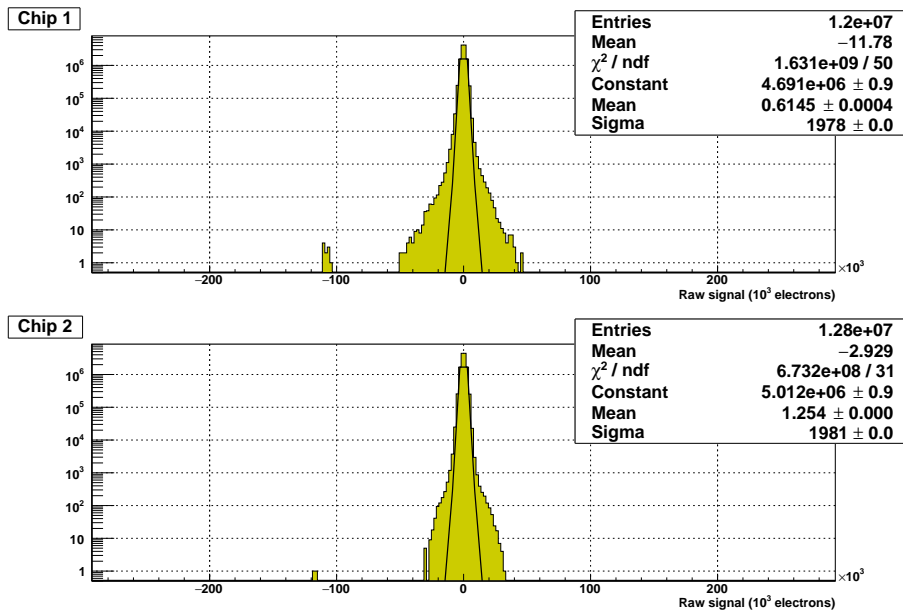
The reason for the non-Gaussian noise did not become entirely clear during the course of this thesis. However, since it can be eliminated for pedestal runs by masking of obviously noisy channels, but is still observed for runs where external sources are used to generate signal in the sensors, it seems to be an effect that is introduced by the additional electronics in play when external sources are used. For future applications it might therefore be useful to look into the role components like the trigger diode or the laser source play for the noise observed in the setup.

3.4 Radioactive Source Tests

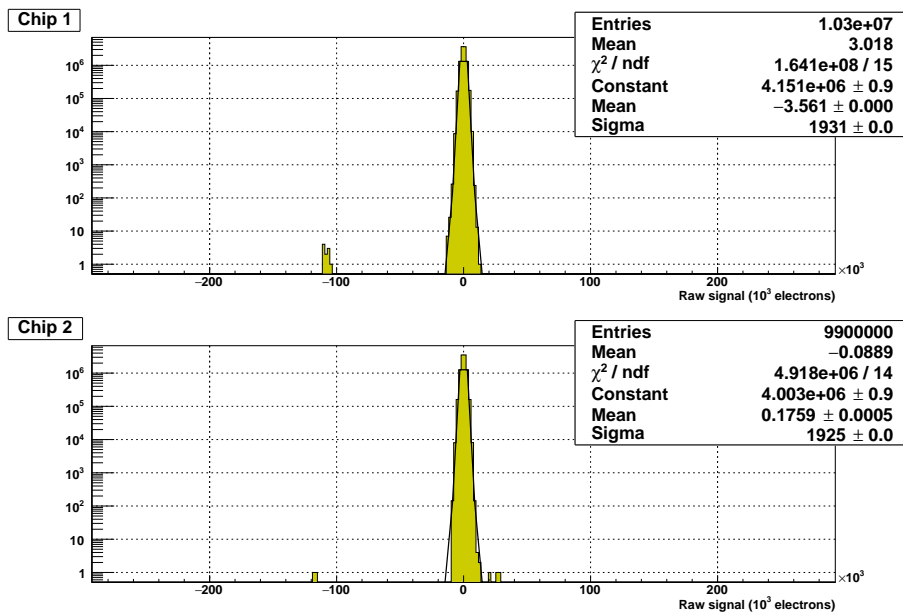
To test the sensor response to charged particles, a ^{90}Sr radioactive source was used. ^{90}Sr is a radioactive isotope of strontium with a half-life of 28.8 years and decays via β^- emission to ^{90}Y (yttrium). ^{90}Y in turn has a half-life of 64 hours and undergoes β^- decay to the stable zirconium isotope ^{90}Zr . Since the γ emission from the decay of ^{90}Y is very infrequent, ^{90}Sr can be regarded as an almost “pure” β^- source. The endpoint energy of the β spectrum is 0.546 MeV for ^{90}Sr and 2.27 MeV for ^{90}Y [36]. ^{90}Sr sources can therefore be used to approximate minimum ionising particles.

3.4.1 Measurement Procedure

For the measurements conducted during this thesis the ^{90}Sr source was placed in a dedicated mounting frame and centred by hand as close as possible above the sensors under test with a distance of about 5 mm to the sensor surface. Since the β^- radiation has a considerable spatial divergence, with this configuration statistics over the whole sensor area are obtained. Due to the statistical



(A) Non-gaussian tails in the spectra of both chips due to noisy channels.



(B) Gaussian noise spectra when disproportionately noisy channels are excluded from the analysis (masked).

FIGURE 3.10: Signal spectra of a pedestal run on both readout chips (128 channels in one histogram) with both sensors biased (Hamamatsu: 250 V, Infineon: 80 V). A Gaussian is fitted to each spectrum. Masking of noisy channels eliminates the non-Gaussian tails of the spectra.

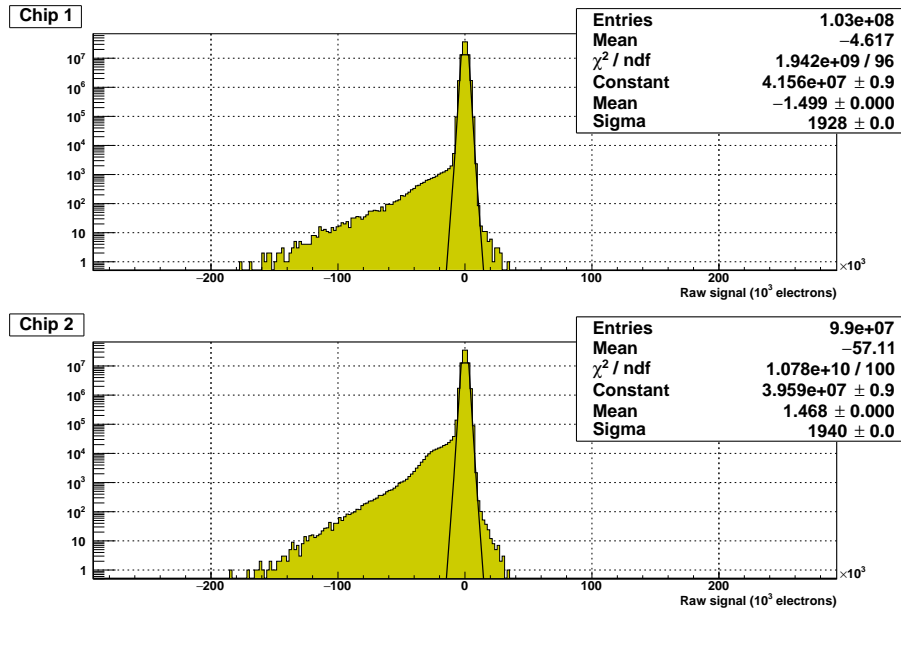


FIGURE 3.11: Signal spectra of a radioactive source run on both readout chips with both sensors biased (Hamamatsu: 250 V, Infineon: 80 V). A Gaussian is fitted to each spectrum. The negative signal results from the n-in-p sensor design (electrons are collected). Even though noisy channels are masked, non-Gaussian noise residues can be observed.

nature of the decay process and the spatial divergence of the β^- beam, the distribution of hits over the sensor surface can be approximated by a Gaussian bell curve (Figure 3.12). To obtain comparable results when looking at the different p-stop sections of the sensors, the x-y stage was used to perform runs with the source aligned roughly at the centre of each section.

The efficiency of the experiment is determined by the number of actual hits per number of triggers received by the trigger board (events). It was around 30% for the setup. This low value can be attributed to the geometry of the setup, the trigger threshold and the setup noise. Since the area of the trigger diode is larger than the area of the P-Stop-GEO sensors, particles that do not hit the sensors under test can still hit the diode below and generate a trigger signal. This effect cannot be eliminated completely, since the vertical distance between the trigger diode and the strip sensors is fixed and the radioactive source, too, cannot be placed infinitely close to the sensor surface. For future experiments it will be practical to further investigate this issue and to employ different means of triggering aside from the ALiBaVa trigger board.

3.4.2 Clustering

When a charged particle hits the silicon strip sensor, the drift of the generated charge carriers in the electric field induces a signal at the strips closest to the particle track. To determine the total charge generated during a particle hit and also to be able to detect its location, by, e.g., a centre-of-gravity calculation, the group of strips that took up the particle signal have to be found. The process of attributing a group of strips to a particle hit is called *clustering*.

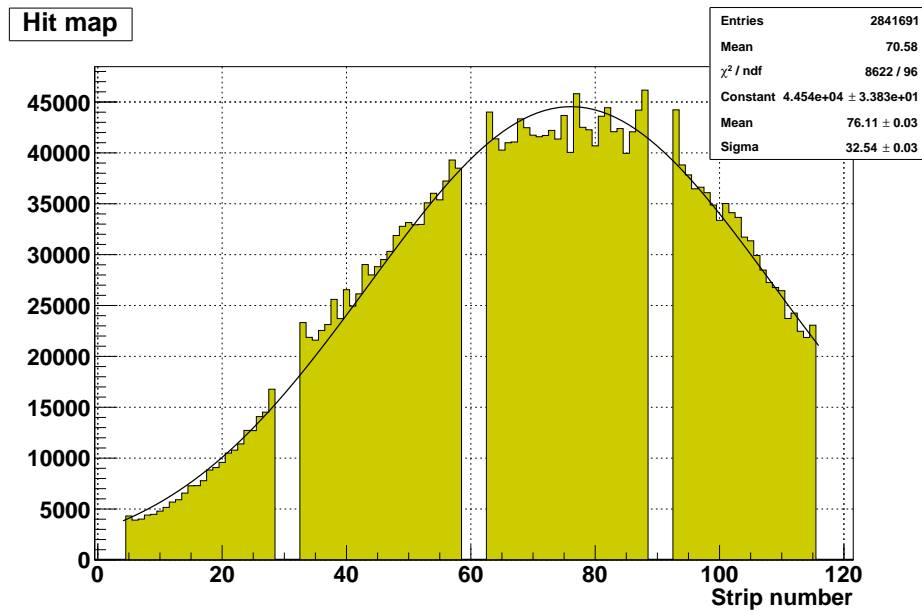


FIGURE 3.12: Hit map of the ^{90}Sr source centred above the Infi-neon P-Stop-GEO sensor for 10^7 recorded events. Noisy channels are masked by the analysis routine and a Gaussian is fitted to the data.

Various routines can be applied to find the cluster of strips associated with a particle hit (see Appendix A.3). Usually certain limits are set that determine the height of the signal amplitude necessary to regard a strip as part of a cluster. These cluster cuts refer to the signal-to-noise ratio of the respective group of strips. If the signal measured on a particular strip exceeds the strip noise by a predefined ratio, the strip is added to the cluster. Normally, two different cluster cuts are applied, the initial *seed cut* and a *neighbour cut*. The seed cut is set to an appropriately high signal-to-noise ratio and is used to determine the seed of the cluster, or the strip that took up most of the charge generated during a particle hit. Only if a strip with a signal exceeding the seed cut is found, the neighbour cut comes into play. It is lower than the seed cut and serves to find adjacent strips that might have detected a smaller fraction of the initial charge. From the seed strip onwards the signal of the neighbouring strips is compared to the neighbour cut, and if the signal of a strip exceeds the neighbour cut, the strip is added to the cluster. This routine is applied sequentially to the strips to the left and right of the seed until on both sides a strip is found that does not exceed the neighbour cut anymore and the cluster is complete. In the end the signal-to-noise ratio of the resulting cluster has to lie above another predefined cluster cut, which is usually the same value as the seed cut, in order for the cluster to be counted.

When looking at this, it becomes clear that the efficiency of the cluster finding algorithm depends on the right cluster cuts. If they are set to too high values, signal will be lost and the efficiency will decrease, while, on the other hand, if they are set too low, random noise will be classified as signal. Common values are a signal-to-noise ratio of 5 for the seed cut and 3 for the neighbour cut.

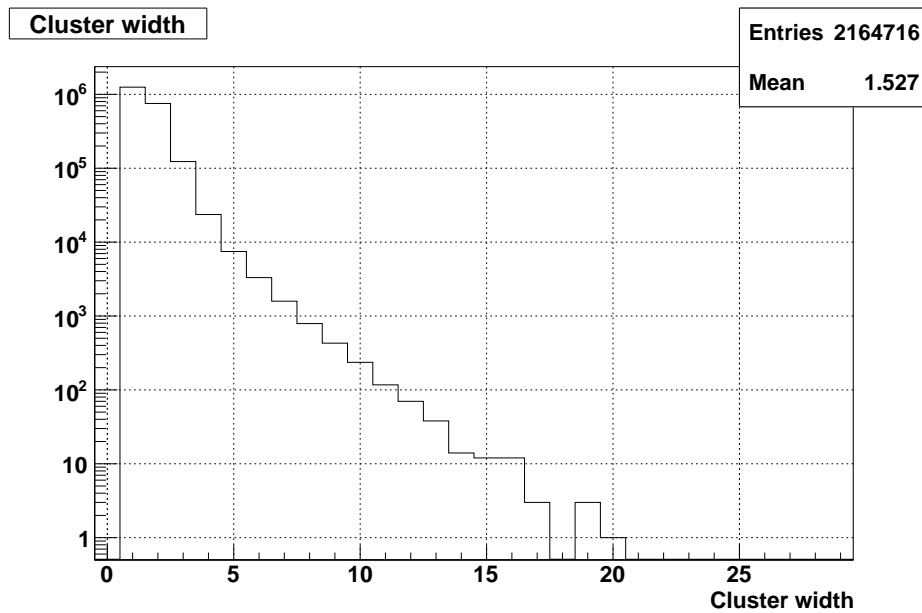


FIGURE 3.13: Distribution of the cluster widths of the ^{90}Sr source centred above the Infineon P-Stop-GEO sensor for 10^7 recorded events, seed cut 8 and neighbour cut 3. Noisy channels are masked by the analysis routine.

The width of the found clusters depends on the incident angle of the particle and the location of the track relative to the strips. For the ^{90}Sr source positioned above the sensor one would expect mostly clusters of size one or two for particles hitting approximately perpendicular to the sensor surface. Depending on their point of impact relative to the strips, the generated charge would mostly be taken up by the closest strip or shared between two strips if the particle hits roughly in the centre between them. However, when looking at the measured distribution of cluster widths for the source centred above the Infineon P-Stop-GEO sensor (Figure 3.13), aside from the expected clusters of sizes one and two, a long tail of broader clusters is observed. This long tail can be attributed to the fact that the spectrum of ^{90}Sr contains a considerable amount of low-energy electrons, which cause much higher signal than a minimum ionising particle. These particles can cause ionised electrons to travel in the plane of the sensor, ionising more electrons along their paths, which in turn results in larger cluster sizes.

A high noise level of random channels can lead to a false classification of random noise as particle hits. Because of the statistical nature of the process, this results in an additional amount of size-one clusters of low signal height caused by random noise. Since the setup used for the measurements as part of this thesis was found to be considerably noisy, this behaviour can be observed distinctly. Looking at the signal spectrum after the clustering routine was used to analyse the data, a peak at the head of the spectrum in the area of low signal heights can be noted, disrupting the characteristic Landau shape and moving the actual Landau peak to lower signal heights (Figure 3.14a). This additional peak is due to noise hits and can be limited by applying stricter cluster cuts (Figure 3.14b). It has to be noted that through this procedure the efficiency of the experiment is lowered further, since due to higher cluster cuts a number of

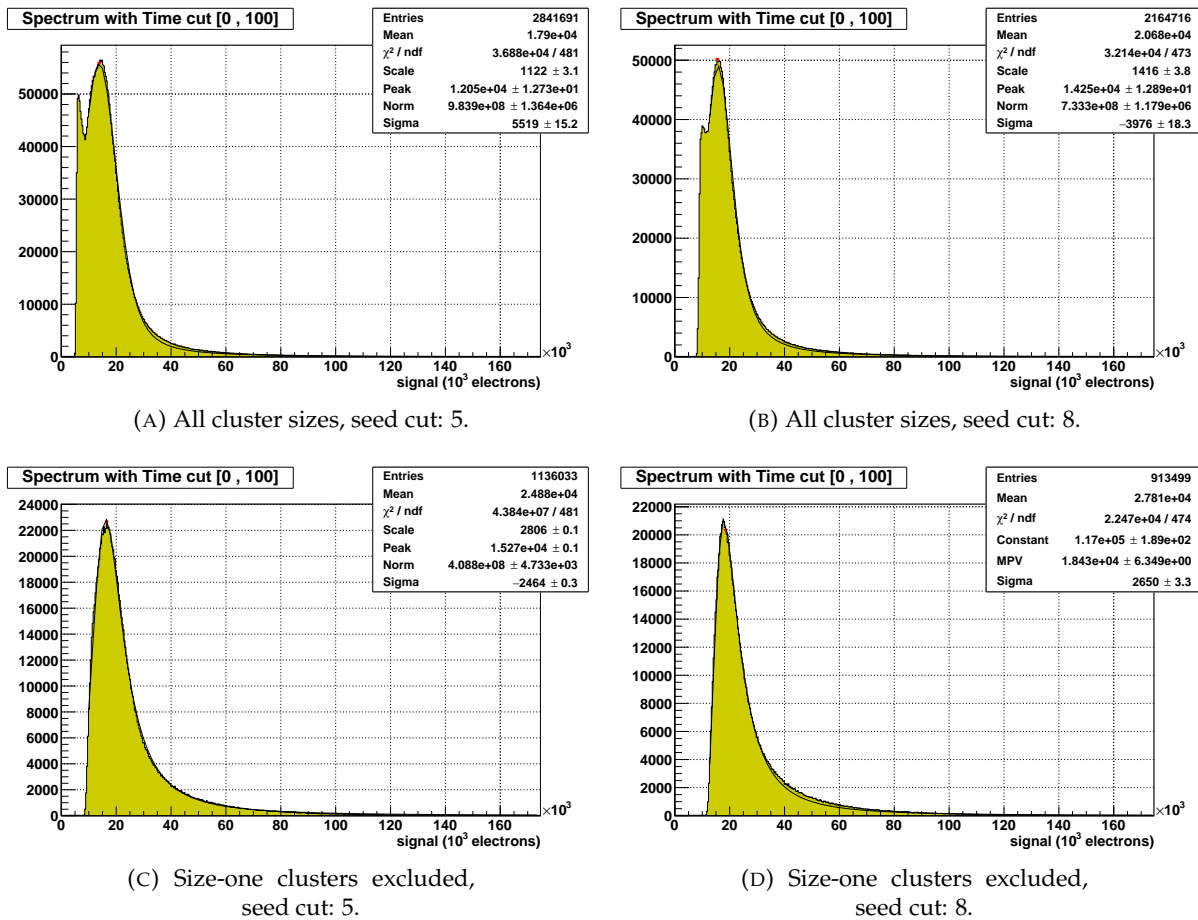


FIGURE 3.14: Signal of the ^{90}Sr source centred above the Infi-neon P-Stop-GEO sensor for 10^7 recorded events compared for different cluster cuts and cluster widths. The seed cut is varied, while the neighbour cut is kept at a constant value of 3. Noisy channels are masked and a Landau curve convoluted with a Gaussian is fitted to the data. By applying stricter cluster cuts the noise peak at the head of the spectrum can be limited. If only clusters of size ≥ 2 are considered, the noise peak can be eliminated completely.

hits with lower signal do not get recognised. An additional indication for the noise hits being the reason for the second peak in the spectrum can be found when looking at the cluster widths. When clusters of size one are excluded from the data analysis, the second peak vanishes completely (Figure 3.14c and 3.14d). Again, this procedure negatively affects the efficiency and now moves the Landau peak to higher signals by cutting off part of the spectrum.

3.4.3 Signal Calibration

As mentioned above, ^{90}Sr is an almost “pure” β^- emitter that can be used to approximate minimum ionising particles. Its spectrum is rather broad and contains a considerable amount of low energy electrons. For this reason the signal of the ^{90}Sr source in a silicon sensor is not exactly the same as that of a MIP. It still provides a sufficient approximation and can therefore be used to

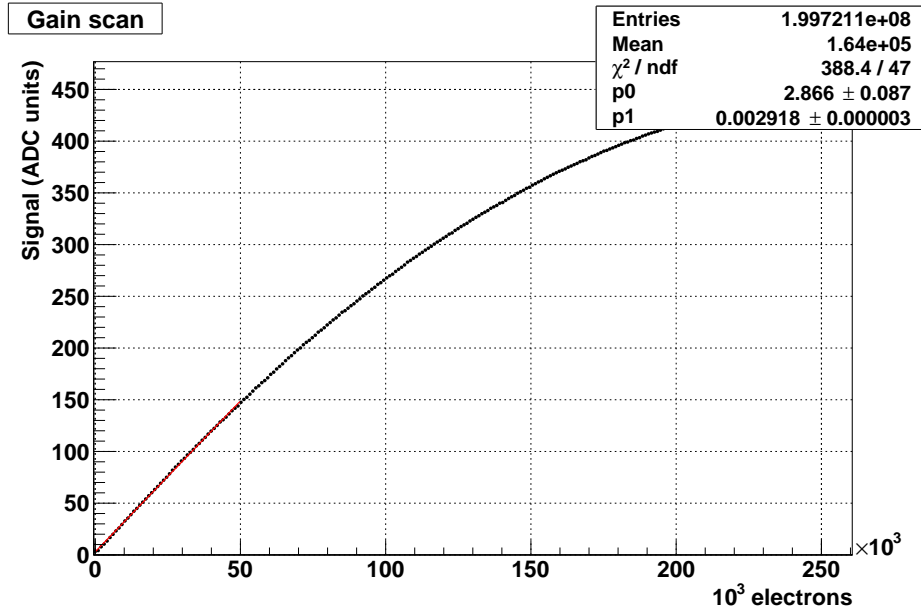


FIGURE 3.15: ADC response function to the Beetle chip test pulses. An exemplary plot for channel 180 is shown. A linear fit (red line) in the range between 0 and 50000 electrons yields a gain of approximately 0.00292 for this channel.

check the plausibility of the signal calibration mechanism the ALiBaVa system provides.

According to the Bethe-Bloch formula (equation 1.12) the mean energy loss dE/dx for a MIP in silicon is $1.664 \text{ MeV g}^{-1} \text{ cm}^2$ [19]. The number of created electron-hole pairs n is derived as the quotient of the total energy loss and the energy E_{eh} needed to create a pair of charge carriers, which is 3.6 eV for silicon. For the Infineon sensor with an active thickness d of $200 \mu\text{m}$ this estimation yields

$$n = \frac{dE/dx \cdot \rho \cdot d}{E_{\text{eh}}} = \frac{1.664 \cdot 10^6 \text{ eV g}^{-1} \text{ cm}^2 \cdot 2.329 \text{ g cm}^{-3} \cdot 0.02 \text{ cm}}{3.6 \text{ eV}} \approx 21500 \quad (3.2)$$

electron-hole pairs created by a MIP. The most probable energy loss scales to approximately 65% of the mean energy loss [19], yielding roughly 14000 electron-hole pairs in a $200 \mu\text{m}$ thick sensor. For the Hamamatsu sensor with an active thickness of $240 \mu\text{m}$ the same considerations yield a mean number of 25800 generated electrons and a most probable value of 16700 electrons.

The response function of the ADC to the charge pulses of the Beetle chip shows a non-linear characteristic (Figure 3.15). While for low to medium height charge pulses the response remains approximately linear, the function is clearly not linear anymore for higher signals. With the above considerations it is expected that the signal will be of the order of magnitude of a few ten thousand electrons and it is therefore legitimate to derive the gain value for each channel from a linear fit to only the lower part of the ADC response function. The measured ADC signal is then divided by the gain value for each channel to calculate the respective charge. For the measurements presented in this thesis a range of 0 to 50000 electrons was chosen for the fit.

When this calibration method is applied to the measured Landau spectra (Figure 3.14), the results fit reasonably well with the above calculations. While the peak is moved to a slightly lower number of electrons because of the influence of random noise, it moves to higher electron numbers if the noise is suppressed by stricter cluster cuts or the exclusion of size-one clusters, which is in good agreement to the expected behaviour. These results give confidence in the calibration mechanism provided by the ALiBaVa system.

3.5 Strip Scans with the Infrared Laser

The majority of the sensor tests during the course of this thesis were performed with an infrared laser. This setup allows to simulate the detector response to charged particles with precise position sensitivity. Position sensitive tests with charged particles are difficult to realise in a standard laboratory setting, as they require a collimated particle beam of sufficient energy and a beam telescope for particle tracking. Thus, tests like these are usually conducted at dedicated accelerator facilities. A laser source constitutes a convenient alternative at position sensitive sensor testing that is applicable in a standard laboratory, without the need for particle accelerators. With a collimated laser beam charge carriers can be generated at a fixed position in the sensor, making it possible to scan across individual strips and investigate properties like charge sharing between strips and also to look deeper into the role of the p-stop layer.

3.5.1 Signal Generation

Similar to charged particles photons can excite electron-hole pairs inside the sensor bulk through the photoelectric effect if their energy $E = h\nu$ is larger than the silicon band gap $E_g = 1.12$ eV. The absorption probability of a photon in silicon strongly depends on its energy. For energies $h\nu$ close to the band gap the absorption coefficient can be expressed as [16]

$$\alpha \propto (h\nu - E_g)^\gamma. \quad (3.3)$$

The constant γ depends on the type of electron transition (direct or indirect, allowed or forbidden) from the valence band into the conduction band and ranges from $\gamma = \frac{1}{2}$ to $\gamma = 3$ [16]. The intensity I of light travelling through a silicon detector decreases exponentially with the penetration depth z according to

$$I(z) = I_0 \cdot e^{-\alpha z}. \quad (3.4)$$

Thus, photons with energies close to the band gap on average can penetrate further into the material than those with higher energy. The light of a laser with a wavelength of 1060 nm like the one at the Laser setup in the HEPHY clean room has a penetration depth of about 800 μm in silicon. If a collimated laser pulse of this frequency traverses a 200 to 300 μm thick sensor, the electron-hole pairs are produced nearly uniformly distributed along the beam path [37].

To simulate the detector response to a charged particle, the laser stimulus has to mimic the fast passage of a relativistic charged particle through the silicon sensor (~ 1 ps) and create electron-hole pairs along its path in an area similar to the small tube where a charged particle deposits charge (radius ~ 1 μm).

This means that the diameter of the laser beam has to be much smaller than the detector strip pitch and the pulse duration of the laser has to be much smaller than the pulse shaping time constant of the detector front-end electronics [37]. Then the diffusion of the charge carriers generated by the laser will cover an area similar to that caused by a charged particle hit in the time until the signal is read out. Lastly, in order for the generated charge to match the signal height of a charged particle hit, the laser power has to be tuned to the right value.

3.5.2 Measurement Procedure

The laser output is collimated and focused to a minimum beam diameter of about $4\ \mu\text{m}$ on the sensor surface. Compared to the sensor strip pitch of $90\ \mu\text{m}$ this is sufficiently small, and together with a pulse duration of $50\ \text{ps}$ as compared to the Beetle chip shaping time of $25\ \text{ns}$ it can be safely assumed that the detector response to the infrared laser mimics that of charged particle hits.

To scan the laser across the sensor surface, the sensor module is moved using the x-y table, and at each point of the scan an ALiBaVa laser run is recorded. This process is automated using the AlCoPi Python software. The vertical distance between the laser optics and the sensor surface is adjusted using the z stage.

Since a high resolution of the inter-strip area is desired, the scans were mostly performed with the smallest possible step size provided by the x-y table, which is $1\ \mu\text{m}$. This results in a minimum of 90 to 100 scan points if only the area between two strips is scanned. With a mean trigger frequency of about $500\ \text{Hz}$ provided by the ALiBaVa board a laser run of 10^4 events takes approximately 20 seconds, and a scan with 100 steps takes about half an hour. With this in mind, a maximum number of 10^5 events could be taken per laser run in order to stay within a reasonable time frame for the laser scans. This is acceptable, since, as opposed to measurements with the radioactive source, the efficiency of the laser runs practically lies at 100%, with every trigger corresponding to a laser pulse that generates a signal in the sensor. Thus, also runs with significantly lower event numbers than for the radioactive source tests provide sufficient statistics.

The parameter of interest for investigations regarding the sensor layout is the measured signal height as a function of the scan position. To obtain this parameter, a Gaussian fit to the pedestal and common mode corrected signal distribution is performed at each channel, and the mean of the distribution is taken to determine the signal height (Figure 3.16). With this method the sensor layout can be mapped, and the influence of structures like the p-stop layer can be investigated.

3.5.3 Tuning of the Laser Signal

In order to mimic the signal of charged particles in the silicon sensor, the laser power has to be tuned. The PiLas laser diode can be tuned by setting the tune value at the control unit. Here a higher value means lower laser power. The control unit provides an auto tune option that fixes the tune value to 37% for frequencies in the magnitude of roughly $1\ \text{kHz}$. With this setting and with no other means of attenuation the laser signal in the silicon sensors is higher than the ADC dynamic range of ± 512 counts. It is possible to manually set the tune value to higher levels. This method, however, is tedious as the response of the

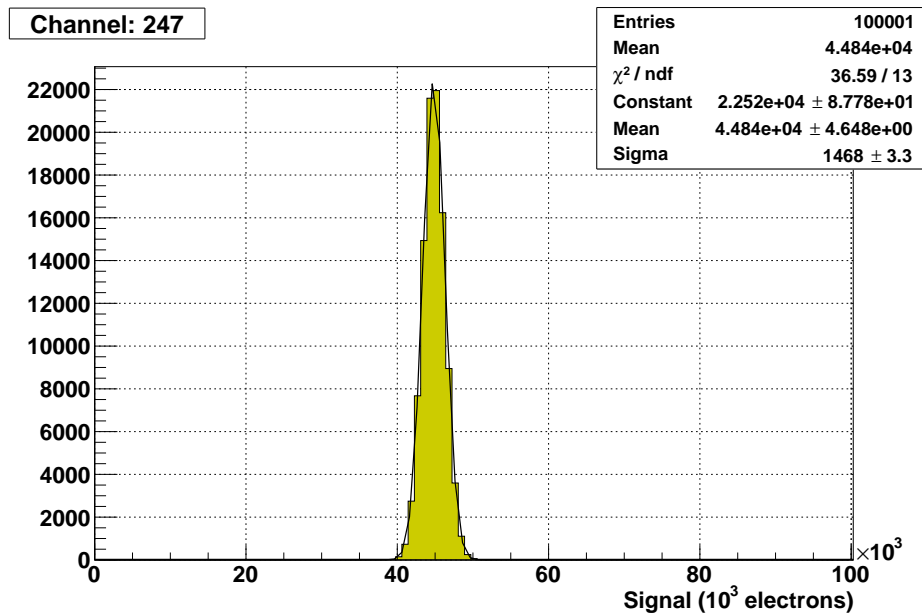


FIGURE 3.16: Laser signal at channel 247 of the ALiBaVa read-out, which corresponds to strip 9 of the Infineon sensor, for 10^5 events. A Gaussian is fitted to the data. The signal height of roughly 44800 electrons corresponds to approximately two times a MIP.

laser power to the tune setting is not linear, with the function getting steeper for higher tune values. This makes it hard to find the correct tune that fixes the signal at a level similar to that of a MIP.

For this reason an attenuator was introduced into the laser setup before the beam splitter (see section 3.1). It allows to tune the laser power by hand. The attenuation strength can be checked by observing the laser power with the power and energy meter. With this setting it is now possible to tune the laser using both, the attenuator and the built-in tune regulation.

To test the laser response to the tune settings, measurements were conducted of the laser signal as a function of the built-in tune value for different attenuator positions (Figure 3.17). For lenient attenuator settings the non-linear dependence of the laser signal on the tune value can be seen distinctly. Additionally, it can be noted that in order to prevent a saturation of the ADC, considerably high settings of either the tune value or the attenuator are necessary. Based on these measurements for all the tests conducted during this thesis the attenuator was set such that the power observed on the power and energy meter was 227 pW, and the laser tune was set to the automatic value of 37%. With these settings the signal generated in the silicon sensors was about 100 ADC counts, which roughly corresponds to two times the mean of a MIP signal.

3.5.4 Determination of the Laser Spot Size

The p-stop implants on the sensor surface have a minimum thickness between 4 and 8 μm . To be able to resolve these structures and also to efficiently mimic the charge deposition of a charged particle, a small laser beam spot is desirable.

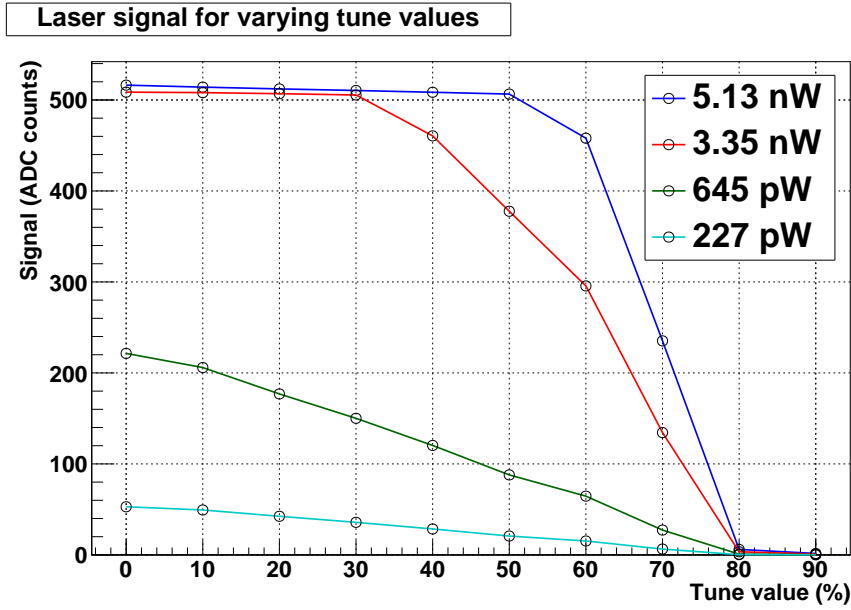


FIGURE 3.17: Signal height of the infrared laser as a function of laser tune for different attenuator settings. The listed values correspond to the power measured at the power and energy meter after the beam splitter for the various attenuator settings. The illuminated ALiBaVa readout channel is 153 (Infineon strip 102).

The minimum beam spot diameter at the beam waist is determined by the used optics and also by the quality of the laser beam. The beam quality can be expressed using the so-called beam quality factor M^2 that essentially describes how closely the laser beam resembles an ideal Gaussian beam [37]. It is a measure of how well the laser beam can be focussed and how strongly its width diverges along the beam axis with increasing distance from the waist. For an ideal Gaussian beam $M^2 = 1$. For the simulation of a charged particle signal it is not only important to achieve a small beam spot diameter at the beam waist, but also to generate charge carriers in a narrow tube along the beam path inside the sensor. Hence the divergence of the beam along the width of the sensor, characterised by the beam quality factor, is an essential parameter for the accuracy with which the laser can mimic the signal of a charged particle.

The radius w of the laser beam is defined as the distance from the beam axis at which the intensity drops by a factor of $1/e^2$ compared to its axial value. Its variation along the propagation axis z is given by [37]

$$w(z) = w_0 \sqrt{1 + \left(\frac{zM^2}{z_R}\right)^2}. \quad (3.5)$$

Here w_0 is the radius at the waist at $z = 0$, and

$$z_R = \frac{n\pi w_0^2}{\lambda} \quad (3.6)$$

is the Rayleigh length, with λ being the vacuum wavelength of the laser beam

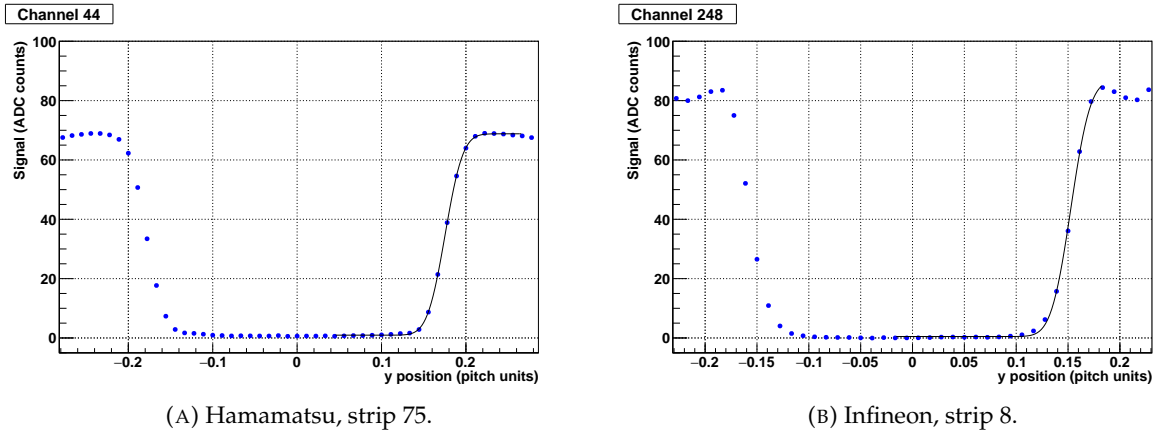


FIGURE 3.18: Comparison of the sensor signal generated by scanning the laser over an aluminium strip, for Hamamatsu and Infineon sensors. To determine the beam spot diameter, a Gaussian error function is fit to the rising edge of the scan.

and n the refractive index of the medium the laser beam travels through. The Rayleigh length denotes the distance along the beam axis in propagation direction from the beam waist to the point where the area of the beam cross section has doubled. This is equivalent to the point on the axis where the beam radius has increased by a factor of $\sqrt{2}$ compared to the waist. The beam quality factor is now defined as the ratio of the beam parameter product (minimum waist size w_0 times angular divergence θ_0) of a real beam and that of an ideal Gaussian beam, denoted with w_G and θ_G , and is given by [37]

$$M^2 = \frac{w_0\theta_0}{w_G\theta_G} = \frac{\pi w_0\theta_0}{\lambda}. \quad (3.7)$$

To determine the beam spot diameter of the laser setup, the laser was scanned across an aluminium strip on the front surface of the sensor (Figure 3.18). As the laser is reflected by the metal surface, the signal decreases gradually when the laser spot moves from the inter-strip region onto the aluminium strip, until it reaches zero when the metal strip fully blocks the laser light. At the opposite edge of the strip the signal increases again as the laser spot moves off the metal. The sharpness of this transition from maximum signal to zero signal at the metal strip is determined by the light intensity profile and size of the laser spot on the sensor plane [37]. Thus, for a Gaussian beam the radius of the beam spot can be determined by fitting a Gaussian error function to the region of the scan where the laser spot moves from the metal strip into the sensitive area between the strips. The used function,

$$S(y) = a \cdot \operatorname{erf}\left(\frac{\sqrt{2}(y - y_0)}{w}\right) + c, \quad (3.8)$$

is essentially a condensed version of the formula proposed in [38]. Here $S(y)$ is the measured laser signal. The variable y is chosen as the coordinate along the axis of the scan in accordance to the convention of the x-y table. The parameter a denotes the amplitude of the Gaussian error function, y_0 is the position

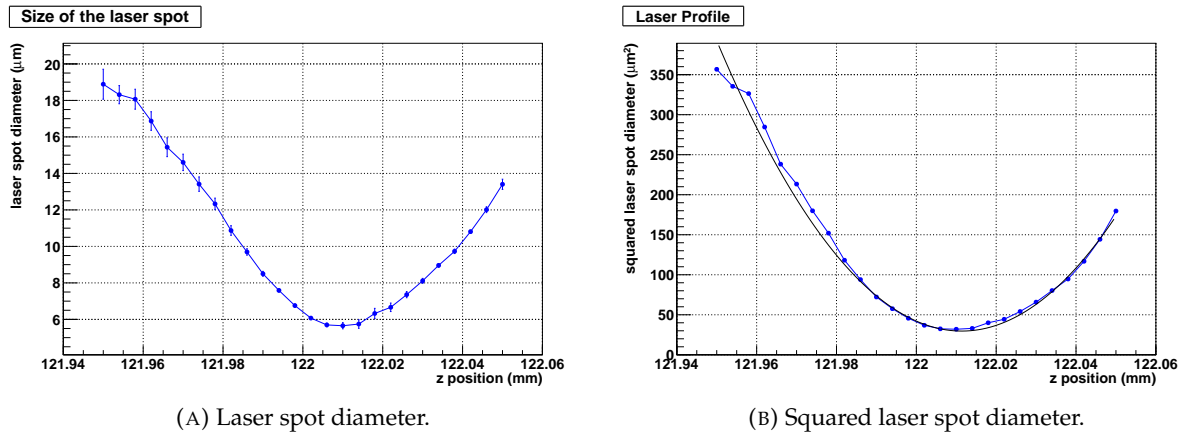


FIGURE 3.19: Laser spot diameter and squared laser spot diameter with a degree 2 polynomial fit for varying z heights, measured at strip 8 of the Infineon sensor (channel 248 of the ALiBaVa readout).

where the signal reaches half of the maximum amplitude, and c denotes the signal height at y_0 . The radius w of the laser spot can be read directly from the fit.

To find the minimum beam spot diameter $d_0 = 2w_0$, the described laser scans were repeated for varying z heights (Figure 3.19a). This way the beam size along the propagation axis z can be mapped, and from these measurements the beam quality factor M^2 can be deduced. For this purpose a polynomial of degree two,

$$d^2(z) = A + Bz + Cz^2, \quad (3.9)$$

is fit to the squared beam diameter for varying heights z (Figure 3.19b) as described in [39]. From the coefficients A , B , and C the position of the waist along the beam axis

$$z_0 = \frac{-B}{2C}, \quad (3.10)$$

the beam diameter at the waist

$$d_0 = \sqrt{A - \frac{B^2}{4C}}, \quad (3.11)$$

and the total angular spread

$$\Theta = 2\theta_0 = \sqrt{C} \quad (3.12)$$

can be determined. Finally, with this information the beam quality factor M^2 can be calculated.

The described measurements were conducted at four equidistant positions on both, the Hamamatsu and the Infineon sensor, one measurement point in each p-stop section. For each of these eight points scans across the sensor surface perpendicular to the strips were performed for varying z heights, and to each of these scans a Gaussian error function was fit as shown exemplary in Figure 3.18. From these fits the beam diameter was obtained and the values were plotted as shown in Figure 3.19. Then a polynomial like in equation 3.9

was fit to the data. The minimum beam spot diameter d_0 and the beam quality factor M^2 were obtained from the fit. Averaging over the results yields the beam spot diameter $d_0 = 4.71 \pm 0.49 \mu\text{m}$ at the waist and the beam quality factor $M^2 = 1.34 \pm 0.12$ in the plane perpendicular to the sensor strips (denoted with y).

If the minimum beam spot diameter is not calculated using the polynomial fit, but instead directly obtained from the error function fit at the calculated waist position z_0 , it yields a smaller result of $d_0 = 4.15 \pm 0.28 \mu\text{m}$. This can be attributed to the fact that the errors of the fit are much larger for greater distances from the waist along the beam axis (if the laser is strongly out of focus), and the polynomial fit, which takes into account the entire range of z scans, tends to overcompensate in these ranges.

A beam spot diameter of 4 to 5 μm is sufficient to resolve the structures on the sensor surface with high-enough accuracy. From the minimal beam spot radius at the sensor surface the radius after propagation through a 200 μm thick silicon sensor can be calculated using equations 3.5 and 3.6 and the refractive index of silicon $n = 3.6$. With these considerations a beam spot radius of 2.075 μm at the sensor surface (beam spot diameter 4.15 μm) increases by almost 200 % to 12.23 μm after the propagation through 200 μm silicon, resulting in a beam spot diameter of 24.46 μm at that distance. This is considerably different from the small tube of magnitude $\sim 1 \mu\text{m}$ that would be expected for the track of a charged particle. However, the spread of the laser beam inside the silicon sensor still remains smaller than the strip pitch of 90 μm . Within these limits it can be assumed that the laser setup can produce results similar to those of charged particles, however, it has to be noted that an exact comparison to charged particle signals is not possible.

3.5.5 Optical Properties of Different Sensor Layers

Silicon strip sensors comprise a number of different surface layers to optimise their electrical properties. These include the dielectric layer between the strip implants and the metal readout strips and the passivation layer that covers the whole sensor surface on the top. Due to the sensor design and the production process that usually includes various steps of photo lithography, edging, and sputtering, thickness and composition of the layers vary over the course of the sensor surface. The light of a laser that is used to investigate the sensor has to travel through the resulting multilayer of different materials on the sensor surface, and, depending on the optical properties and the thickness of the layers, different amounts of light will be reflected and transmitted at the layer interfaces. In the end the intensity of the light that reaches the sensor bulk determines the charge deposition inside the sensor and the generated signal. Hence, to correctly interpret the measured laser signals, multiple reflections and thin film interference between the surface layers have to be considered.

When a laser beam passes through the silicon sensor, it crosses several boundaries of thin layers with different optical properties. At each boundary a fraction of the light is reflected, and the rest is transmitted. The amount of light that is reflected and transmitted at a boundary essentially depends on the angle of incidence and the refractive indices of the bordering materials. For an angle of incidence of 90° (perpendicular to the sensor surface) the Fresnel reflection coefficient r at the boundary between materials of refractive indices

n_1 and n_2 becomes [37]

$$r = \frac{n_1 - n_2}{n_1 + n_2}. \quad (3.13)$$

A thin layer is characterised by two interfaces, at which light can be reflected and transmitted. The Fresnel reflection coefficients r_1 and r_2 for both interfaces can be calculated using equation 3.13 and the refractive indices of the interfacing materials n_1 , n_2 , and n_3 . Depending on the layer thickness d_1 , the optical path lengths of the beams reflected at the two boundaries differ, and interference occurs that can be both, destructive and constructive. The thickness of a thin layer is therefore an important parameter that characterises the resulting reflectance R of the layer, given by [37]

$$R = 1 - \frac{(1 - r_1^2)(1 - r_2^2)}{(1 - r_1 r_2)^2 + 4r_1 r_2 \sin^2(\phi/2)}. \quad (3.14)$$

Here ϕ is the phase difference between the transmitted light and the light reflected between the boundaries of the layer,

$$\phi = \pi + \frac{4\pi d_1 n_2}{\lambda}, \quad (3.15)$$

with n_2 being the refractive index of the thin layer between the boundaries and λ the vacuum wavelength of the laser light [37]. As can be seen from equation 3.15, the reflectance has a minimum if the optical thickness of the layer $d_1 n_2$ is an odd multiple of $\lambda/4$ and a maximum if $d_1 n_2$ is an even multiple of the quarter wavelength.

With these considerations an estimate of the intensity of the transmitted light and thus the relative height of the expected laser signal is possible if the composition of the multilayer on the sensor surface is known. The calculations presented within this thesis were performed with a dedicated online tool that uses the transfer-matrix-method to calculate the net reflectance of a given multilayer [40].

For both investigated sensors the exact composition of the surface multilayer is not known. The layers and processed materials are likely to vary from vendor to vendor, and it cannot be assumed that the surface layers are the same for the Hamamatsu and the Infineon sensor. However, aside from these vendor-specific differences in material composition and layout, the qualitative structure of the surface layers is expected to be similar (Figure 3.20). Based on microscope investigations and vendor specifications, a sandwich dielectric composed of a layer of SiO_2 and a thin layer of silicon nitride (Si_3N_4) is assumed for the reflectance calculations. The thickness of the SiO_2 layer varies above the p-stop implants and below the metal strips as compared to the rest of the sensor. The Si_3N_4 layer is very thin and is only added in the area below the aluminium strips to enhance the coupling qualities of the dielectric. Lastly, a layer of silicon nitride of unknown stoichiometric composition (Si_xN_y) is assumed as passivation.

With these assumptions the relative change of reflectance for different thickness variations and layer structures can be calculated and compared to the experimental results of the laser scans. For these calculations essentially two features of the surface multilayer can be pointed out, where variations of the reflectance are expected: the areas above the p-stop implants, where the SiO_2 layer is thinner than on the remaining sensor, and the areas at the edges of the

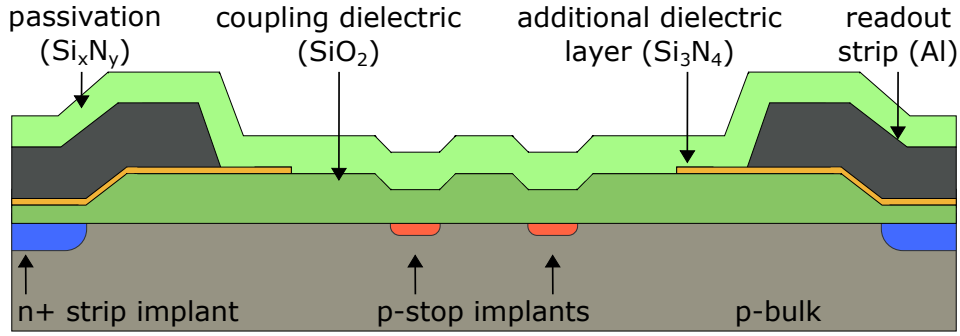


FIGURE 3.20: Qualitative cross section of the region between two strips of a silicon strip sensor, indicating the different layers at the surface. The material composition assumed for reflectance calculations is indicated in brackets. Some vendor-specific material variations have to be expected.

metal strip, where the silicon nitride layer reaches into the inter-strip regions. The p-stop layer itself does not have to be considered as an additional thin layer. Although a change of the refractive index is expected with an increase in doping concentration, this effect remains considerably small. Deviations of the refractive index of doped silicon from the nominal value have been found for doping concentrations above 10^{18} cm^{-3} [41]. The doping concentrations of the p-stop implants of the investigated sensors are considerably lower. In this case the expected change of the refractive index due to the doping concentration is of magnitude 10^{-4} [42] and thus negligible. Within these limits the p-stop layer can therefore be treated like normal silicon with a refractive index of $n = 3.6$ at a wavelength of 1060 nm.

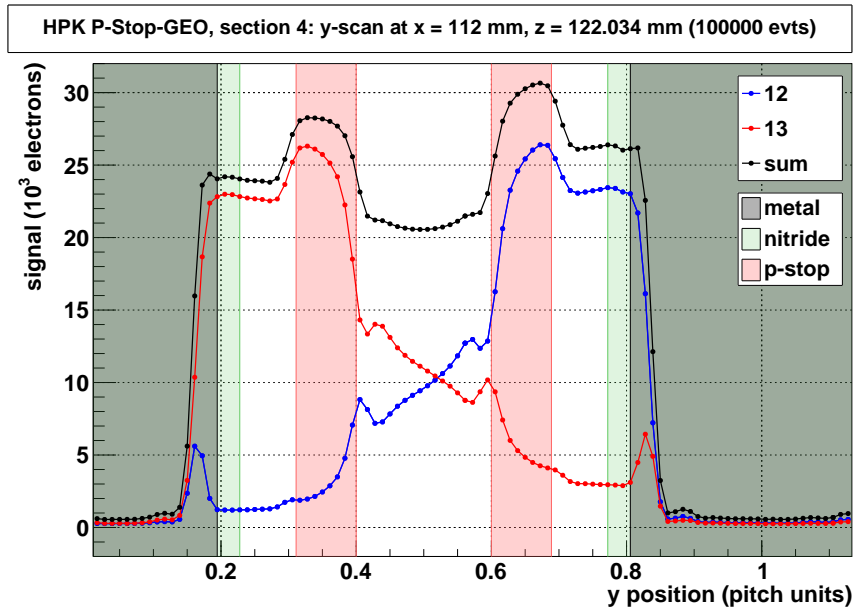
To determine the reflectance of an assumed multilayer, the thickness and the refractive indices of the involved materials must be known. With the assumptions made for the multilayer composition the refractive indices are known for all the materials except for the passivation layer. For Si_xN_y the refractive index depends on the silicon-nitrogen ratio Si/N and was estimated using [43]

$$n = \frac{[4(\text{Si}/\text{N}) - 3]n_\infty + 6n_{3/4}}{4(\text{Si}/\text{N}) + 3}. \quad (3.16)$$

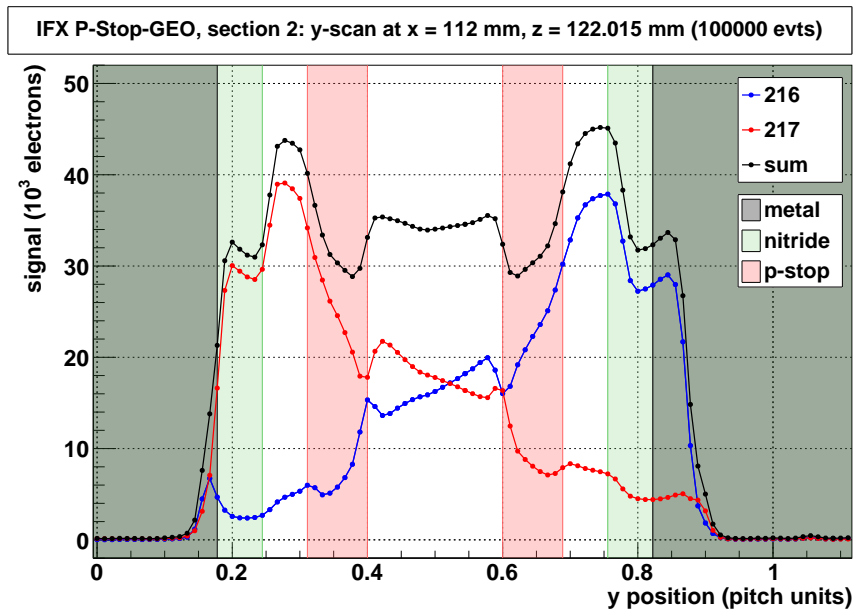
Here n_∞ is the nominal refractive index of silicon and $n_{3/4}$ that of Si_3N_4 . The thickness of the individual layers was taken from electron microscope measurements.

Looking at the laser signal as a function of the position between the readout strips, distinct variations can be observed (Figure 3.21). In the area of the p-stop implants a prominent rise of the measured signal by approximately 25% appears for the Hamamatsu sensor (Figure 3.21a), while for the Infineon sensor the signal drops by roughly 14% in the same area (Figure 3.21b). Additionally, a drop by about 29% is observed below the silicon nitride dielectric layer for the Infineon sensor. These observations can be attributed completely to the optical effects of the aforementioned surface layer variations.

As can be seen from equations 3.14 and 3.15, the reflectance R shows an oscillating characteristic as a function of the optical thickness d_1n of a thin layer with a period of $\lambda/2$ (Figure 3.22). The relative signal change ΔS caused by variations of the layer thickness is calculated using the transmittance $T = 1 - R$



(A) Hamamatsu, p-stop section 4.



(B) Infineon, p-stop section 2.

FIGURE 3.21: Laser scans perpendicular to the readout strips for the Hamamatsu and the Infineon sensor. Displayed are the signals on the two strips closest to the scanning laser spot and the sum of both signals. The surface structures based on the GDS layout files are superimposed on the plots. For both sensors the signal variations over the Si_3N_4 dielectric layer and the p-stop implants can be attributed to the optical properties of the different surface structures.

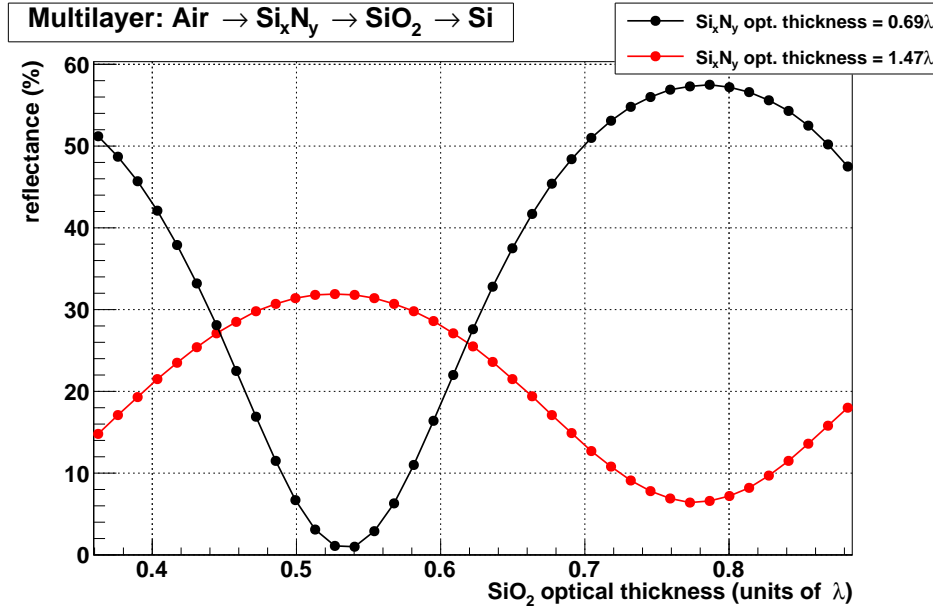


FIGURE 3.22: Reflectance of the multilayer above the p-stop implants as a function of the optical thickness d_1n of the oxide in units of the laser wavelength λ , plotted for different passivation configurations.

and

$$\Delta S = \frac{T_2 - T_1}{T_2} = \frac{R_1 - R_2}{1 - R_2}, \quad (3.17)$$

with $T_1 < T_2 < 1$ and $R_2 < R_1 < 1$.

Especially the fact that the Hamamatsu sensor shows a signal rise at the p-stop layer, where the Infineon sensor shows a signal drop, is a bold indication for an optical effect being the reason for these signal variations. A relative shift of the optical thickness d_1n of the silicon nitride passivation layer by an odd multiple of the quarter wavelength ($3\lambda/4$ for Figure 3.22) causes the reflectance function to shift so that a minimum will appear, where before a maximum was observed and vice versa. With this configuration for the Infineon sensor a decrease of the optical thickness of the SiO_2 layer above the p-stop implant by 0.45λ corresponds to a relative signal drop of 13.7%. Assuming a $3\lambda/4$ shift of the optical thickness of the silicon nitride passivation layer for the Hamamatsu sensor as compared to the Infineon one, a decrease of the optical thickness of the SiO_2 layer above the p-stop implant by 0.42λ then corresponds to a relative signal rise of 24.8%. Similarly, the configuration with the thin Si_3N_4 layer for the Infineon sensor yields an expected signal drop of 30.7%. For the Hamamatsu sensor the thin dielectric layer reaches not very far into the inter-strip region, and the reflectance differences compared to the passivation layer are presumably very small so that no signal change can be observed due to this additional layer.

In general the reflectance values calculated based on the electron microscope measurements of the real sensors are in very good agreement with the measured signal variations. Thus, it can be concluded that the observed signal variations for both sensors are due to the optical properties of the surface multilayer.

Chapter 4

Results

4.1 Influence of the P-Stop Layer on Charge Sharing

Charge sharing between adjacent strips is an important parameter that determines the achievable position resolution of a silicon strip sensor and the accuracy with which a particle track can be reconstructed. For particle tracks that do not hit the sensor perpendicular to the surface it is apparent that the charge generated along the particle track will be shared by a number of strips. But also for perpendicular tracks, like they are simulated with the infrared laser, charge sharing is an important phenomenon. Due to the diffusion of the charge carrier cloud inside the sensor material, the resulting signal is shared between the strips closest to the particle track. The coordinate of the particle hit can then be found by interpolation through, e.g., a centre-of-gravity method. How well this method can reconstruct the “real” point of impact of a traversing particle, is influenced by the charge sharing process between the involved strips as well as by the signal-to-noise ratio.

The p-stop layer is expected to have an impact on the charge distribution inside the sensor. As additional p-doped structures between the n⁺-strips, the p-stop implants alter the electric field inside the sensor. The spatial distribution of the charge cloud generated by a passing particle necessarily will be affected by the altered electric field. An impact on the ratio of charge shared between neighbouring strips as compared to a sensor without additional p-stop structures is to be expected. In the following this process will be studied in more detail and the results for different p-stop geometries will be discussed.

4.1.1 The η -Function

A convenient way to characterise the charge sharing between adjacent strips is provided by the η -function [44, 45]

$$\eta(y_0) = \frac{Q_R(y_0)}{Q_L(y_0) + Q_R(y_0)} . \quad (4.1)$$

Here Q_L and Q_R denote the charge collected by the left and right strip respectively, and y_0 denotes the centre of the laser spot measured with respect to the centre of the left strip. The variable y is again chosen for consistency with the axes of the x-y table. Defined such, the η -function describes the ratio of the charge collected on the right strip and the total charge collected on both adjacent strips. Thus, it essentially describes the charge sharing between the two strips as a function of the laser position.

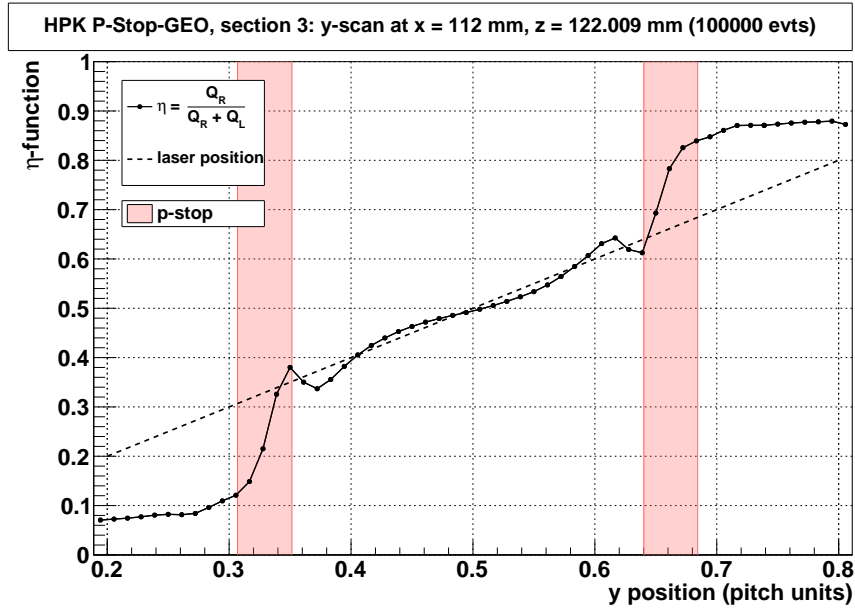


FIGURE 4.1: The η -function measured between ALiBaVa read-out channels 43 and 44 (Hamamatsu strips 76 and 75), denoting the reconstructed impact point with a centre-of-gravity method, compared to the real position of the laser spot. The p-stop structures based on the GDS layout file are superimposed on the plot.

The η -function is a very instructive tool to understand the influence of charge sharing on the position reconstruction capabilities of a silicon strip sensor. To resolve the original position y_0 of a charged particle track or a laser beam from the charge collected at a cluster of strips, the most common method is to calculate the centre of gravity

$$y = \frac{\sum_i (Q_i \cdot y_i)}{\sum_i Q_i}. \quad (4.2)$$

Here Q_i is the charge collected at the strip with index i , and y_i is the centre of that strip. The sum spans over the whole cluster of strips. If this method is applied to only two adjacent strips with the coordinates $y_L = 0$ and $y_R = 1$, it yields essentially the η -function $y = \eta(y_0)$.

For tests with the infrared laser the position y_0 is known. Comparing it to the position predicted by the centre-of-gravity method, however, distinct discrepancies can be observed (Figure 4.1). While in the central region between the strips the η -function stands in good agreement with the linear function of the laser position, at the edges, close to the strips the η -function does not show the same approximately linear dependency anymore. This non-linear behaviour can be explained by the charge diffusion process inside the sensor [44].

The width of the charge diffusion cloud is not very large compared to the strip pitch [44]. If the laser is positioned close to one of the two readout strips, most of the generated charge will be read by that strip, which results in the plateaus observed in the η -function at those positions. Only when the laser

moves toward the central region between the strips, the charge cloud is divided between both strips. In this region an approximately linear trend of the η -function can be observed. At the p-stop implants diffraction effects due to the height variations of the surface structures at the edges of the p-stop implants can be seen (see section 3.5.5). Thus, in the area of the p-stop implants the course of the η -function is not comparable to the signal expected of a charged particle hit.

In addition to the non-linearity of the η -function due to the width of the charge cloud, another feature stands out. In the areas close to the readout strips most of the charge flows to one strip. However, a small fraction is always shared with the neighbouring strip, as the η -function does not reach 0 or 1. This effect is due to the capacitive coupling between the strips [44].

From the course of the η -function measured with the infrared laser it becomes clear that a linear centre-of-gravity algorithm will produce satisfactory results in the inter-strip region, but will result in larger errors for particle tracks close to the strips. To improve the achievable position resolution, tracking algorithms that take the actual shape of the η -function into account have to be applied. To do this, the position y , as reconstructed from a centre-of-gravity method, is corrected to

$$y_{\eta} = y + f(\eta), \quad (4.3)$$

where $f(\eta)$ is the integral of the probability density distribution of η [44, 46].

A correction like this will be successful, if $f(\eta)$ is a strictly monotonic function of η or, in other words, if to every value of η corresponds exactly one value $f(\eta)$. Thus, in areas where the η -function exhibits flat plateaus, the correction algorithm will not be able to achieve a perfectly accurate position reconstruction. However, the algorithm will still considerably improve the accuracy of the track reconstruction as compared to a pure centre-of-gravity method.

4.1.2 Comparing Charge Sharing for Different P-Stop Layouts

The impact of the p-stop layer on the charge sharing between adjacent strips and consequently on the achievable position resolution of an n-in-p silicon strip sensor shall be investigated. For this purpose laser scans between neighbouring strips were performed for all the different p-stop layouts on the two sensors from Hamamatsu and Infineon. From these measurements the η -function was calculated for the different p-stop configurations. The results are compared in the following.

For an easier orientation on the resulting plots, the sensor structures, including the p-stop implants, the nitride layer of the dielectric, and the metal strips, are superimposed on all the figures. It has to be noted that the depicted structures are aligned by hand according to the measured signal distribution and that their dimensions correspond to those specified in the respective GDS layout files. These dimensions do not necessarily coincide exactly with the actual dimensions of the sensor structures. Different processing methods and production variations at the vendors can cause deviations from the theoretically expected layout. The exact layout of the investigated sensors is not precisely known, which can result in some offset or misalignment in the presented figures.

Additionally, it also has to be noted that only the η values in the inter-strip regions constitute reliable results. Because of the high reflectivity of the

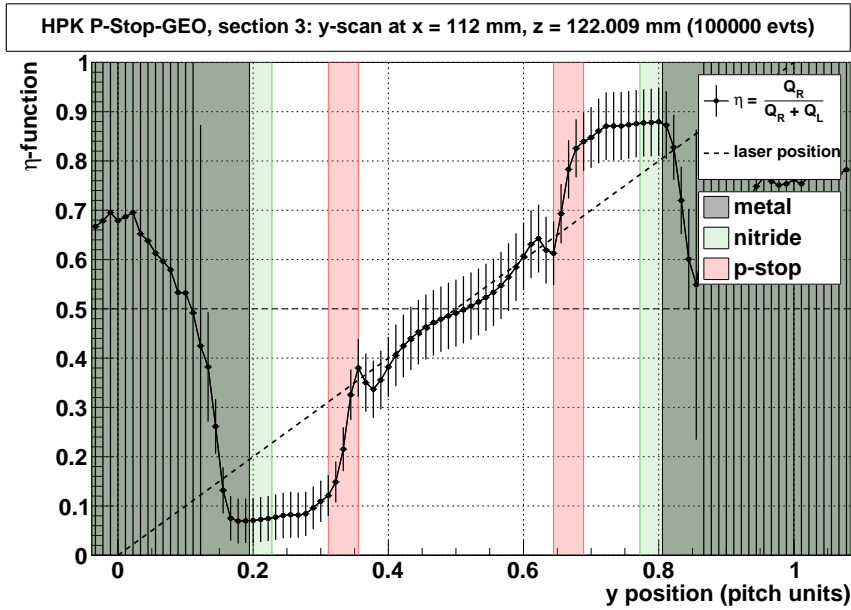
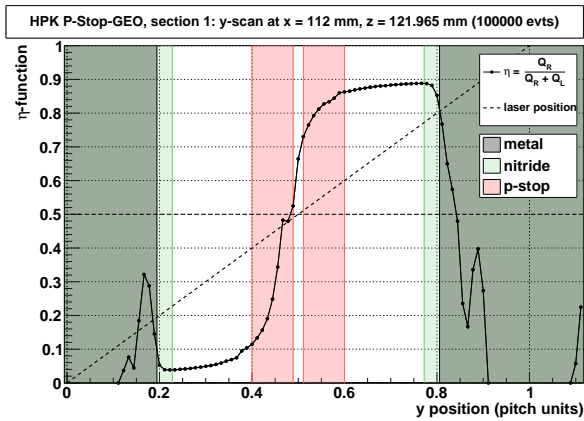


FIGURE 4.2: The η -function at p-stop section 3 of the Hamamatsu sensor (strips 75 and 76), compared to the linear function of the real laser position, with propagated errors. The surface structures based on the GDS layout files are superimposed on the plots.

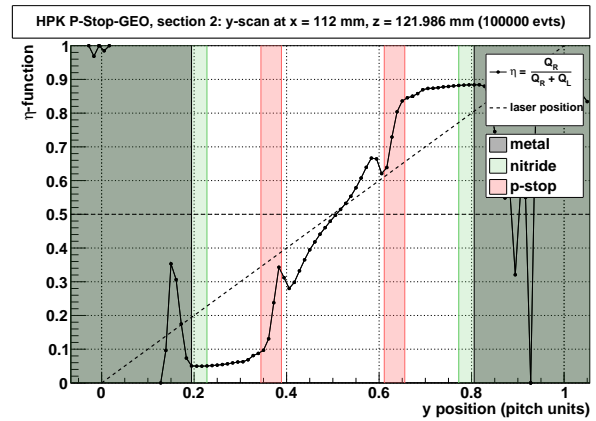
aluminium layer and the negligibly small penetration depth of light into aluminium at the used wavelength of about 1060 nm, the signal at the metal strips is practically zero, which results in considerably high errors for all the η values in the area of the metal strips (Figure 4.2). In favour of an easier readability the error bars are not depicted in the following graphs.

The η -functions obtained for both, the Hamamatsu and the Infineon sensor, are displayed in Figure 4.3 and Figure 4.4. In general in the central region between the p-stop implants an approximately linear trend can be noted, where mostly the η -function agrees relatively well with the real position of the laser beam. Discontinuities like the ones in Figure 4.4a can be attributed to diffraction effects at the surface edges and the finite width of the laser spot.

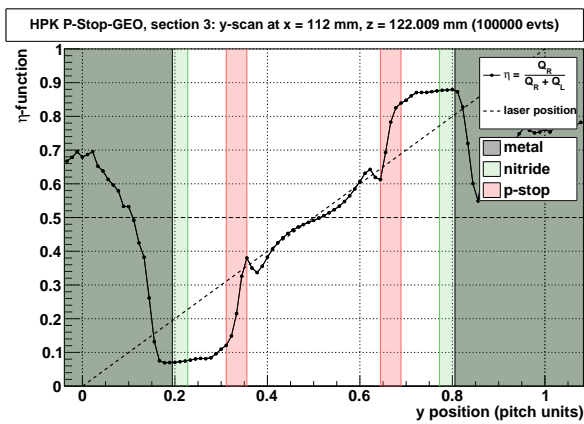
The approximately linear behaviour of the η -functions notably changes in the areas between the strip and the closest p-stop implant. Consistently, for all measured p-stop geometries, in the regions between the strip and the p-stop layer most of the generated charge flows to the closest strip, and only a small amount is transferred to the second strip. This feature is especially striking for the Hamamatsu sensor, where in the region between strip and p-stop the η -function is almost constant. While this feature is to some extent expected due to the finite width of the charge diffusion cloud, as explained in section 4.1.1, it is still notable that the width of this area of constant η values is determined by the distance between the strip and the p-stop implant (compare Figures 4.3a and 4.3d and Figures 4.3b and 4.3c). The plateau observed in the η -function is always confined to the area between the strip and the p-stop implant. A large distance between strip and p-stop thus corresponds to a wide plateau, whereas a closer spacing of strip and p-stop notably diminishes the width of



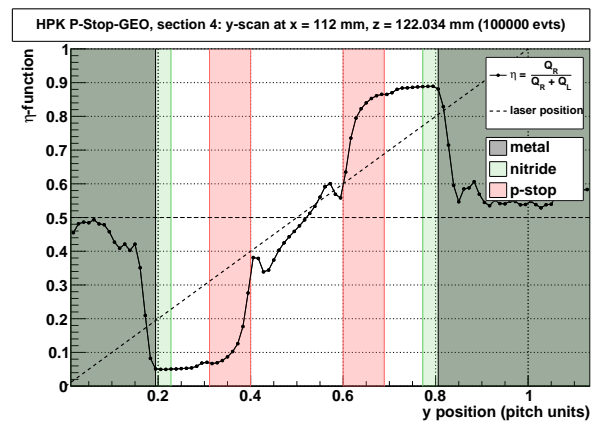
(A) Hamamatsu, strips 14 and 15.



(B) Hamamatsu, strips 44 and 45.



(C) Hamamatsu, strips 75 and 76.



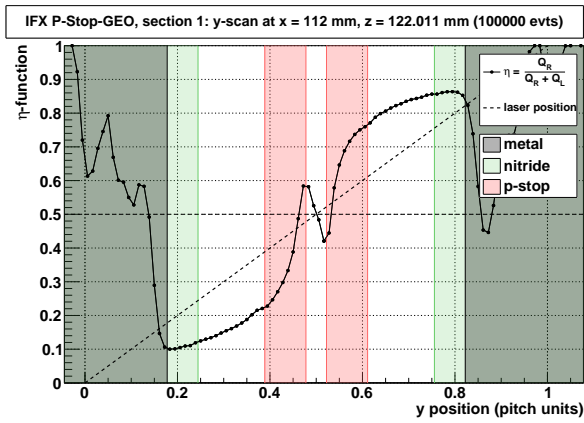
(D) Hamamatsu, strips 108 and 109.

FIGURE 4.3: The η -function measured at the four different p-stop geometries of the Hamamatsu sensor, compared to the linear function of the real laser position. The surface structures based on the GDS layout files are superimposed on the plots.

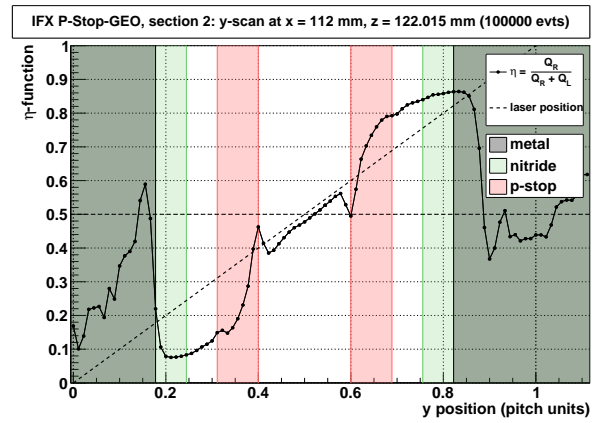
the η plateau. As a result the impact point reconstructed from a centre-of-gravity algorithm will be more accurate for configurations where the p-stop implants are positioned close to the readout strips.

This effect can be understood if the configuration of the electric field in the sensor is considered (Figure 4.5). The p-stop implants essentially introduce an area of zero electric field (constant electric potential) in the region between the strips (Figure 4.5b). If charge carriers are generated in this area of the sensor, the charge cloud widens due to diffusion, until some carriers begin to drift in the weighting field of one strip, while the charge carriers at the other end of the charge cloud will drift in the weighting field of the second strip, similar to a configuration without p-stop structures (Figure 4.5a). For charge carriers generated close to one of the strips, in the area between the strip and the p-stop implants, the weighting field of the second strip is effectively screened by the barrier of p-stop, and as a result the charge carriers will mainly drift toward the closest strip, which leads to the observed plateau of the η -function.

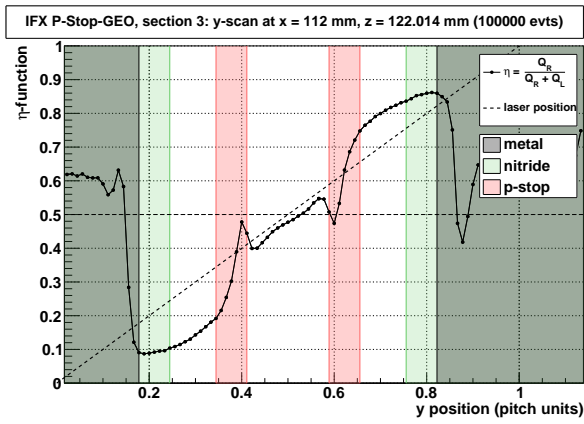
For the Infineon geometries this plateau is not as pronounced as for the Hamamatsu sensor. Here a monotonic rise of the η -function can be observed



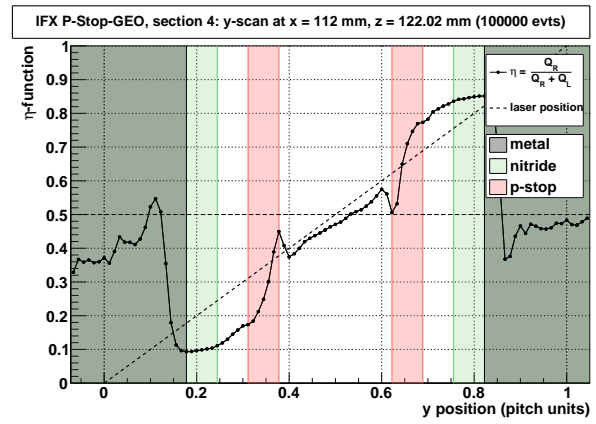
(A) Infineon, strips 8 and 9.



(B) Infineon, strips 39 and 40.



(C) Infineon, strips 71 and 72.



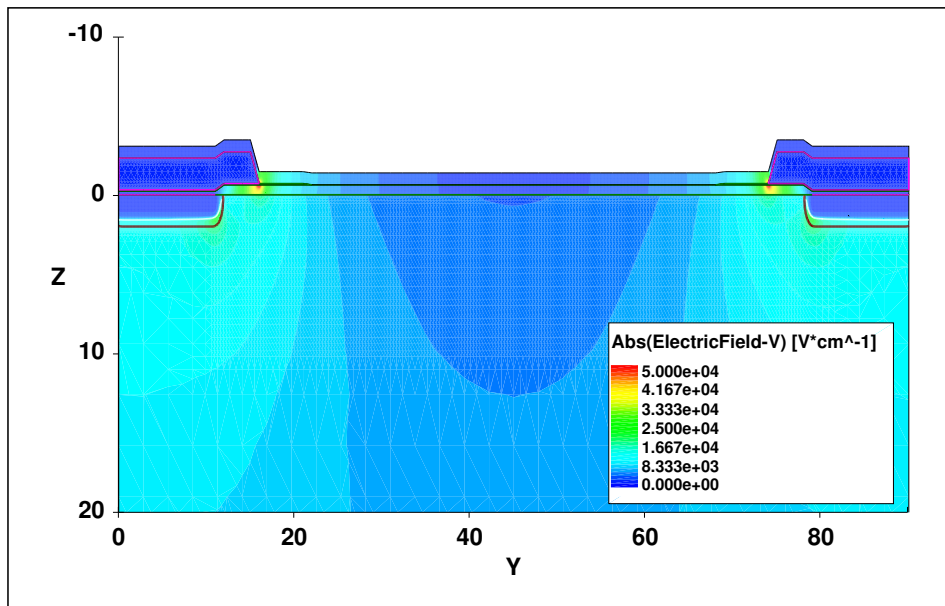
(D) Infineon, strips 102 and 103.

FIGURE 4.4: The η -function measured at the four different p-stop geometries of the Infineon sensor, compared to the linear function of the real laser position. The surface structures based on the GDS layout files are superimposed on the plots.

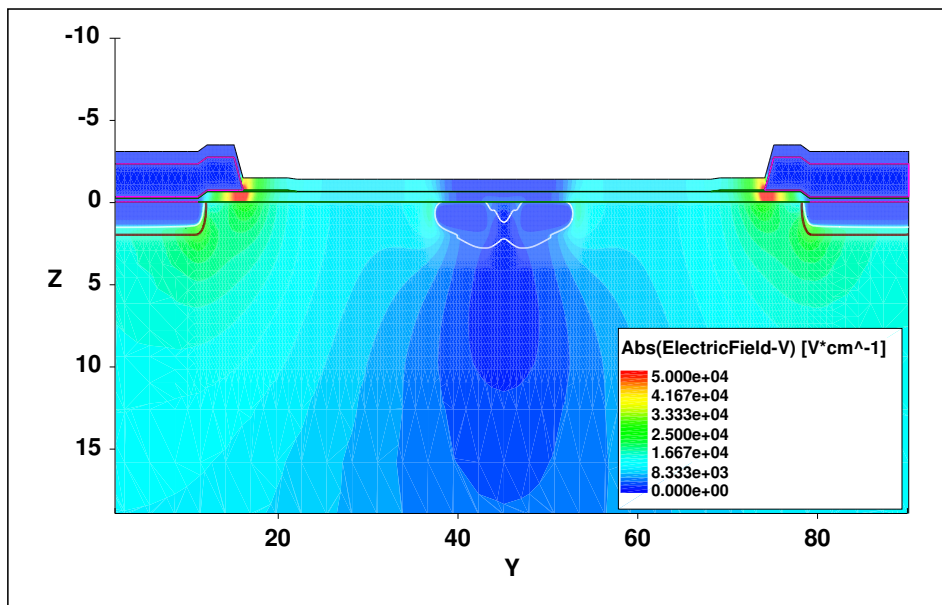
also in the regions between the strips and the p-stop layers. This behaviour can possibly be explained with a slightly lower doping concentration and a smaller implant depth of the p-stop implants, which would result in a different configuration of the electric field. Thus, the η -functions measured for the Infineon sensor follow the course of the real laser position somewhat more accurately than those for the Hamamatsu sensor. In combination with an η reconstruction algorithm this will lead to a more accurate reconstruction of the “real” particle track as compared to the Hamamatsu sensor.

This difference between the two sensors also becomes apparent when looking at the function characteristic in the area between the p-stop layers. Here the rise of η is much stronger than that of the linear function of the laser position for some Hamamatsu geometries (Figure 4.3a, 4.3b and 4.3d). The slope of the η -function in this area correlates with the distance between the p-stop layers, with closer spaced p-stop implants resulting in a steeper slope. This comes as a natural consequence of the wider plateaus caused by these configurations.

It becomes clear from these measurements that the p-stop spacing has a strong influence on the linearity of the η -function and thus on the accuracy of



(A) Configuration without p-stop.



(B) Configuration with p-stop implants.

FIGURE 4.5: TCAD (Technology Computer Aided Design) simulation of the electric field in the inter-strip region of a biased silicon strip sensor. Comparison between configurations with and without p-stop implants. Axis units are μm . The electric field essentially is computed by numerically solving the Poisson equation for a predefined mesh of points along the sensor cross section.

a centre-of-gravity position reconstruction method. In addition to this it can be noted that also the thickness of the p-stop layer affects the charge sharing between adjacent strips. This becomes apparent when p-stop implants with the same distance from the strips, but varying thickness are compared (Figure 4.3c and 4.3d as well as Figure 4.4b and 4.4d). As the plateaus of the η -function extend into the p-stop layers, thicker implants also broaden the area where charge carriers almost exclusively drift toward the closest strip implant. This can be explained by the fact that broader p-stop implants increase the screening effect on the electric field between the strips.

All of the presented measurements illustrate the effect the p-stop layer has on the charge sharing between neighbouring strips reasonably well. A quantitative analysis of this effect was not performed as part of this thesis, however, the qualitative process could be depicted and investigated. P-stop implants effectively disrupt the electric field in the inter-strip region, leading to a “screening” of the weighting fields of the electrodes, which causes charge carriers that are generated in the area between strip and p-stop implant to almost exclusively drift toward the closest strip electrode. This leads to a distinctly non-linear behaviour of the η -function. The effect is less pronounced for somewhat lower doping concentrations of the p-stop implants.

In general it can be noted that thin p-stop layers close to the readout strips yield the closest approximation of the η -function to a linear characteristic. With such configurations a centre-of-gravity method for particle tracking that does not take into account the actual shape of the η -function will yield more accurate results than for configurations with thicker p-stop layers that are spaced close together in the central region between the strips.

4.2 Charge Loss at the P-Stop Implant

The p-stop layer alters the electric field configuration inside a silicon strip sensor. Field peaks that characteristically appear at the edges of the metal strips and n^+ -implants are observed, albeit less pronounced, at the edges of the p-stop layers as well [47]. Charge carriers that are generated inside the silicon bulk drift in the electric field. Depending on their point of origin these charge carriers will see different field strengths. Considering the field peaks at the p-stop implants, it is possible that some part of the generated charge carriers drift toward the p-stop implants and accumulate there, which may result in a fraction of the generated charge not being detected at the n^+ -strips.

The laser measurements of the P-Stop-GEO sensors of both, Infineon and Hamamatsu, provide a convenient way of studying the phenomenon of charge loss due to the p-stop layer. In the following the results of the conducted measurements will be discussed and qualitative conclusions about charge loss at the p-stop layer will be drawn.

4.2.1 Comparison of Different P-Stop Layouts

In order to investigate a possible charge loss caused by the p-stop layer, laser scans between neighbouring strips were performed for all p-stop geometries of the Hamamatsu and the Infineon sensor. The results are plotted in Figure 4.6 and Figure 4.7. Displayed are the signal on the left and right strip respectively as well as the sum of both signals.

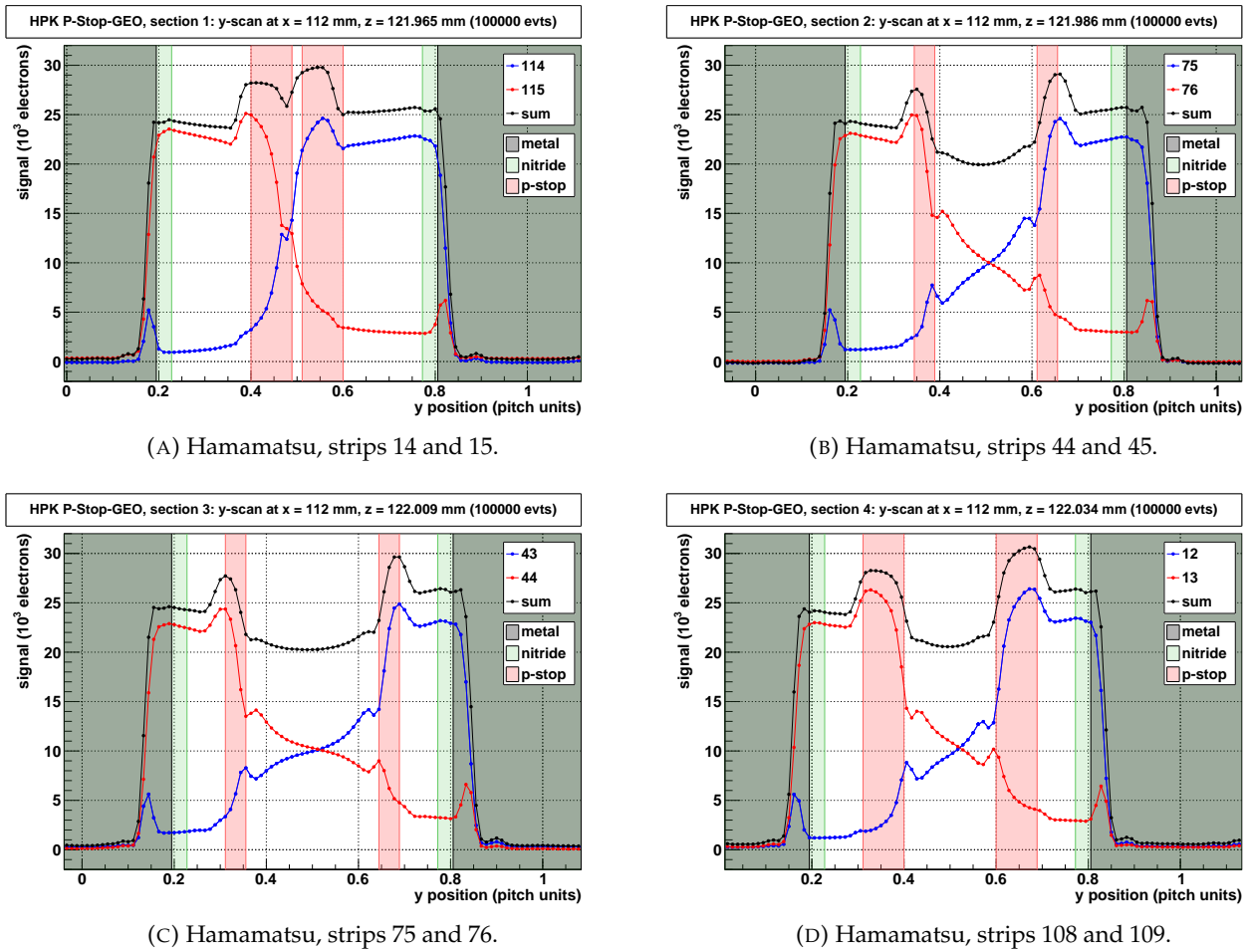


FIGURE 4.6: Laser scans perpendicular to the readout strips for the Hamamatsu sensor. Displayed are the signals on the two strips closest to the scanning laser spot and the sum of both signals. The surface structures based on the GDS layout files are superimposed on the plots.

Disregarding the comparatively small amount of charge that is read out at the second-order neighbours, the sum of the signals on the two adjacent strips constitutes the total charge deposited in the silicon bulk by the laser at every scan point. As external conditions like the laser power do not change over the course of a scan, the total deposited charge should stay approximately the same for every scan position. This holds true as long as the surface layer configuration is the same for all regarded scan areas. Due to their altered optical properties, areas of varying surface layer thickness or composition have to be excluded from this analysis (see section 3.5.5). For this reason only areas with the standard layer configuration: passivation, oxide, silicon bulk (“white” regions in Figures 4.6 and 4.7) are considered for the following qualitative analysis.

When first looking at the results of the performed laser scans for different p-stop geometries, a prominent feature can be noted: In the regions between the p-stop implants the sum of the charge collected at both readout strips is

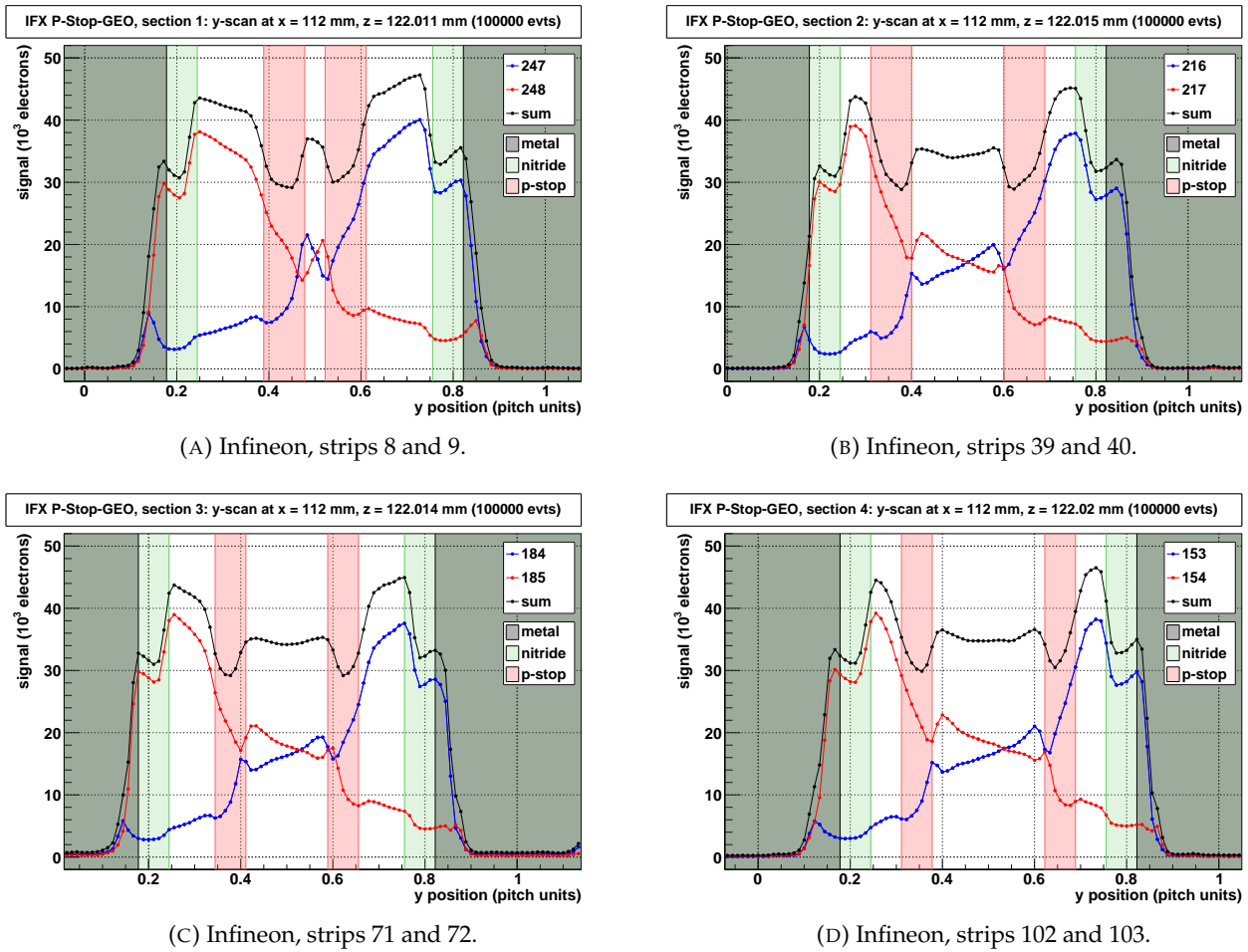


FIGURE 4.7: Laser scans perpendicular to the readout strips for the Infineon sensor. Displayed are the signals on the two strips closest to the scanning laser spot and the sum of both signals. The surface structures based on the GDS layout files are superimposed on the plots.

significantly smaller than in the regions between the strips and the p-stop implants. This effect is seen for all the p-stop sections on both, the Hamamatsu and the Infineon sensor, with the exception of Hamamatsu section 1 (Figure 4.6a). In this case the finite laser spot diameter of roughly $4\ \mu\text{m}$ does not allow a sufficiently high resolution of the area between the p-stop implants, which are spaced apart by only about $2\ \mu\text{m}$ according to the respective GDS layout file. For the remaining sections the observed signal drop is very similar, ranging from approximately 17.2% at Infineon section 1 (Figure 4.7a) to 22.2% at Infineon section 4 (Figure 4.7d). Averaging over all measured sections except for Hamamatsu section 1, yields a mean signal drop of $19.7 \pm 1.75\%$ in the area between the p-stop implants.

An additional feature of all the measurements is a higher sum signal in the area of the right strip as compared to the left side. This effect remains at 6% for all the measured sections and could not be fully resolved during the course of this thesis. However, the systematic nature of the effect points to a common cause in the detector readout or the laser scan method. To account

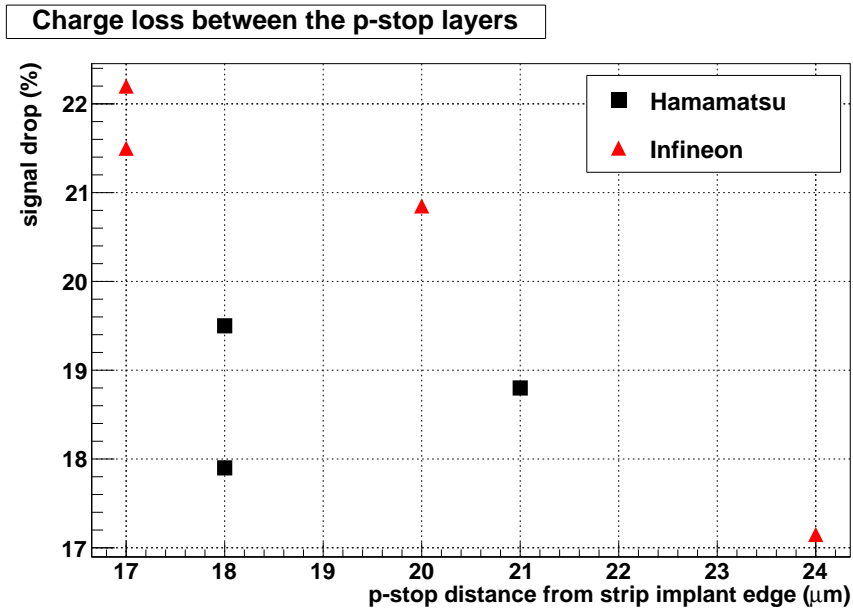


FIGURE 4.8: Charge loss in the region between the p-stop layers as a function of the distance between the strip implant edge and the p-stop edge, measured for the Hamamatsu and the Infineon sensor.

for this irregularity, the percentages of the signal drop in the region between the p-stop layer were calculated with respect to the average signal on the left and right side.

The observed signal drop in the inter-strip region between the p-stop implants is a strong indication for an effect of charge loss attributable to the p-stop structures. The magnitude of this effect remains roughly the same for all observed p-stop configurations. However, a slight dependency on the p-stop spacing can be observed, which is more pronounced for the data of the Infineon sensor (Figure 4.8). A significant dependency of the signal drop on the width of the p-stop layer is not observed.

In addition to the signal drop in the area between the p-stop layers, for the Infineon sensor in the regions between the strips and the p-stop implants a decrease of the signal can also be observed for closer distances of the laser spot to the p-stop layer (see Figures 4.7a and 4.7c). This as well can be interpreted as an indication of an effective loss of collected charge due to the p-stop layer.

In summary, from all the measurements conducted for various p-stop geometries for two different sensors it can be deduced that the p-stop layer has a significant influence on the charge collection inside the sensor. For laser incidence points in the region between the p-stop implants a distinct loss of signal is observed, which is attributed to a loss of charge caused by the change of the electric field configuration due to the added p-stop layers. The observed charge loss is reduced if the distance between strip implant and p-stop layer is increased, but the possible improvement remains considerably small.

4.3 Favoured P-Stop Layout

From the conducted measurements of the p-stop configurations of the Hamamatsu and Infineon P-Stop-GEO sensors a conclusion about a favourable p-stop layout with regard to charge sharing capabilities and charge loss shall be drawn.

From the investigation of the charge sharing process between neighbouring strips it was found that wide p-stop layers that are spaced close together in the central region between the readout strips negatively affect the performance of a standard centre-of-gravity algorithm for particle tracking. For such configurations the charge sharing function η shows a strong non-linear characteristic that can be attributed to the screening effect of the p-stop layer in the electric field distribution inside the sensor. For particle tracks between the strip and the p-stop layer most of the generated charge is read by the closest strip as the p-stop layer weakens effective charge sharing between neighbouring strips. In order to minimise this effect, a p-stop configuration with thin p-stop layers located close to the readout strips is preferable. Also, lower doping concentrations and shallower implant depths of the p-stop layer were found to be advantageous.

The effect of the p-stop layer on the electric field inside the sensor also causes a distinct loss of charge especially in the regions between the p-stop layers. This feature is not very strongly affected by the chosen p-stop layout. As a somewhat preferable configuration with regard to charge loss, a layout with larger distances between the readout strips and the p-stop implants is proposed.

As can be seen from this considerations, the requirements for the p-stop layout with regard to charge sharing and charge loss somewhat contradict one another. Considering the low impact variations of the p-stop configuration had on the charge loss effects, focusing the efforts of layout design on the influence of the p-stop layer on charge sharing appears preferable. However, by applying the η -correction to the centre-of-gravity tracking method, especially for lower p-stop doping concentrations and implant depths the performance can be improved. With this in mind the layout design can be focused more on improving the charge loss effect caused by the p-stop layer. Thus, it can be concluded that for the investigated purposes a p-stop configuration comprising small implant widths and p-stop layers centred close together between the n^+ -strips is favourable. For this purpose a common p-stop layout variant with just one implant between the strips might even show better results.

In the end, however, also parameters like, e.g., the inter-strip resistance and the high-voltage stability of a sensor as well as the performance under irradiation have to be considered to determine a favourable p-stop layout. For this purpose further investigations and quantitative assessments of the p-stop properties that go beyond the scope of this thesis will be necessary. It will come down to finding the happy medium between factors like charge sharing and charge loss on the one hand and the electrical properties of the sensors, which determine the stability of the sensor performance, on the other.

Chapter 5

Summary and Conclusion

5.1 The P-Stop Layer and its Influence on Sensor Performance

This thesis focuses on the influence of the p-stop strip isolating structure on the performance of silicon strip sensors. The p-stop layer is an additional p⁺-implant that surrounds the individual n⁺-strips of an n-in-p type silicon strip sensor. Its purpose is to increase the resistance between the sensor strips by disrupting the electron accumulation layer that forms at the surface of these sensors due to the assembly of positive charges in the covering oxide surface layer. With the inclusion of the p-stop layer into the sensor layout the electric field inside the sensor is altered compared to a configuration without additional strip separation.

It was an important aspect of the presented work to study the effects of the p-stop layer with respect to the charge sharing between adjacent strips and charge loss caused by the p-stop implant. For this purpose two prototype sensors comprising a number of different p-stop geometries from two different manufacturers were investigated using a radioactive source and an infrared laser system.

A newly purchased ALiBaVa readout system [28] for silicon strip sensors was set up in the laboratory and successfully commissioned for the usage with the prototype sensors. A set of ROOT macros provided by ALiBaVa was employed for offline data analysis and adapted and enhanced for the requirements of the sensor tests. The remastered macros can be downloaded from a dedicated SVN repository [34].

For the sensor tests with this system a module was built, composed of the tested sensors wire bonded to the readout channels of the ALiBaVa daughter board. A number of readout channels showed considerably high noise levels that appeared as distinct non-Gaussian tails in the raw signal spectrum. These high noise peaks could be attributed to strips at the sensor edges as well as the non-bonded channels of the readout chips. The non-Gaussian noise could be significantly reduced by masking of the affected channels during offline data analysis.

An infrared laser system was applied for position sensitive testing of the sensors. The influence of the surface layer structure on the laser signal in the sensor was investigated, and the observed signal variations could be traced back to differences in the surface multilayer thickness and composition. Scanning the laser spot across the sensor surface perpendicular to the strips, subsequently the different p-stop geometries could be studied.

It was found that the p-stop layer strongly affects the charge sharing between adjacent sensor strips. With the p-stop layers present, charge carriers

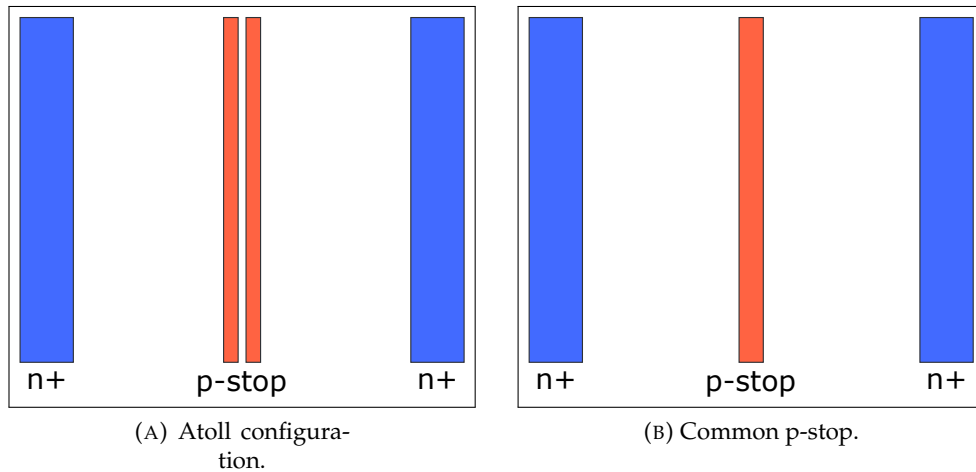


FIGURE 5.1: Qualitative p-stop layout proposed for an optimised performance with regard to charge sharing and charge loss.

that are generated in the area between the strip and the p-stop implant preferably drift toward the closest strip, which causes a distinct non-linear characteristic of the charge sharing function in these areas. This characteristic negatively affects the performance of a linear centre-of-gravity method for reconstructing the impact point of a traversing charged particle. The disadvantageous influence of the p-stop layer on charge sharing is improved by thinner p-stop implants that lie close to the respective strips. Also lower doping concentrations of the p-stop layer showed a slightly better performance in terms of charge sharing. A non-linear tracking algorithm with an η -correction applied to the centre-of-gravity track reconstruction is expected to significantly improve the tracking performance.

Due to the influence of the p-stop layer on the electric field inside the sensor, a loss of detected charge in the magnitude of 20 % was observed in the region between the p-stop implants. This effect turned out to be only minimally influenced by the p-stop geometry, preferring closely spaced p-stop structures in the centre between the sensor strips.

With respect to the properties investigated as part of this thesis it is concluded that a p-stop configuration with relatively thin implants spaced close together at the centre between the readout strips (Figure 5.1a) or even a common p-stop variant (Figure 5.1b) is preferable, as it would minimise the effect of charge loss. To account for the worsening of the charge sharing in such a configuration, the centre-of-gravity tracking algorithm has to be improved with a more accurate η -correction. However, it has to be stressed that to be able to paint a complete picture and determine the best possible p-stop layout, other parameters like the required inter-strip resistance or the performance under irradiation have to be considered.

5.2 Outlook and Open Issues

The study of the properties of the p-stop layer leaves open a field for further investigations. It will be very instructive to employ the newly set up ALiBaVa

system to investigate a larger number of different p-stop geometries to gain a quantitative insight in the parameters charge sharing and charge loss. Additionally, it will be of interest to study the same sensors again after irradiation and investigate the influence of the p-stop layer on parameters like the charge collection efficiency.

Furthermore, in terms of quantitative analysis of the p-stop properties, it will be possible to gain a lot of insight from TCAD simulations of the sensor response to the laser stimulus. Comparing the laser simulations to simulations of charged particle signals will help to understand the accuracy with which the laser can mimic charged particle hits and to better apply the results to real-life experiments with charged particles.

Another important objective to be able to quantify the laser measurements and compare them to charged particle measurements will be the analysis of the sensor surface layer structure. Parameters like thickness and composition of the individual layers will have to be investigated in more detail to comprehend the influence of the surface multilayer on the laser beam intensity and also to be able to correctly interpret the measured signals. For this purpose as well numeric simulations will help to gain a lot of insight.

With regard to the commissioned readout system and laboratory setup, further investigations will be necessary to fully tackle the noise issue. Studies in this direction are already under way, and newly built modules with different sensors have already shown better performances in terms of the observed noise levels.

Additionally, the issue of asymmetric signals with a bias towards readout strips the right side has to be tackled. This behaviour has also been observed for other sensor modules and will probably have to be tracked to a fundamental component in the electronic readout or the analysis routines.

The extended ROOT macros are still being improved. It is a dedicated goal to incorporate more features and also to facilitate the user interaction. The commissioned system will be employed at an upcoming test beam experiment, where newly built sensor modules will be tested with a focused charged particle beam.

Appendix A

ALiBaVa ROOT Macros for Offline Data Analysis

The ALiBaVa software includes a number of macros based on C++ and ROOT to analyse the data taken during ALiBaVa runs. A brief description of the macros can be found in [33]. These macros were enhanced and extended to meet the requirements that arose during the course of this thesis.

A.1 Installation

The remastered macros can be found in an SVN repository [34] together with the tar.gz-files of a number of ALiBaVa software versions and a README-file with basic installation instructions. To install the macros ALiBaVa should be installed as well. On Linux based systems the installation procedure from the sources in the SVN repository is as follows:

1. Unpacking the tar.gz-file of the ALiBaVa version that shall be installed by typing: `tar -zxvf alibava-x.x.x-x.tar.gz`.
2. Copying the files in `/alibava-system/root_macros_only` into the folder `/root_macros` of the unpacked ALiBaVa distribution.
3. Typing `./configure` in the parent directory of the unpacked ALiBaVa distribution. Here it is useful to pass the directory to which ALiBaVa should be installed by specifying `-prefix=$HOME/ALIBAVA` or any other directory, otherwise ALiBaVa will be installed to `/usr/local`.
4. Typing `make` and `make install`.
5. If another prefix than `$HOME/ALIBAVA` has been specified, finally the `rootlogon.C` file in the `/root_macros` folder of the installed ALiBaVa distribution has to be edited to contain the right paths to the ALiBaVa installation directory and the directory that contains the ROOT macros.

To check if the macros have been installed correctly, one can open ROOT from the `/root_macros` folder. The line

```
=====
:> libAlibavaRoot.so loaded
=====
```

should be printed. If this is not the case, the paths have not been specified correctly in the `rootlogon.C` file.

If the macros are altered by the user, they can be compiled from the `/root_macros` folder using the provided makefile `Makefile_vh` by typing `make -f Makefile_vh`.

A.2 Important Classes and Functions

In the following a number of important features of the extended ROOT macros are explained to help with the orientation for new users.

A.2.1 DataFileRoot

The `DataFileRoot` class is the first instance needed to read the ALiBaVa data files and access the data within. It can work with files of type `AsciiRoot` (binary data file format) or `HDFRoot` (HDF5 file format) and contains a number of functions that can be used to process the data. A selection of the most interesting and useful ones is given in the following:

- `compute_pedestals()`
This method computes the pedestals from the data file by fitting a Gaussian to the peak with the lowest mean of the raw signal histogram for each readout channel. It can be employed if no dedicated pedestal run was recorded and also to process the data from a pedestal run that was not saved using the "Save Pedestals" option, which produces a text file, but instead recorded as a standard run using the "Log Data" option. The number of events that shall be considered for the pedestal calculation (`int mxevts`) and whether or not a common mode correction shall be performed (`bool do_cmmd`) can be passed as parameters to the function.
- `find_clusters()` and `find_clusters_vh()`
These methods contain the clustering routines that are part of the macros (see section A.3). The method `find_clusters()` is essentially provided by ALiBaVa, while `find_clusters_vh()` was written and customised as part of this thesis.
- `load_pedestals()`, `load_masking()` and `load_gain()`
As their names suggest, these are the methods to retrieve pedestals, masked channels and calibration values from user specified txt-files. The read values are consequently used for the performed data analysis.
- `process_event()`
This method calculates the signal for every readout channel from the read data by subtracting pedestals and common mode. The common mode correction is performed per default, but can be suppressed by specifying the boolean `do_cmmd` as false. The signal-to-noise ratio is calculated with this method as well.
- `common_mode()`
This method computes the common mode noise. The algorithm is explained in section A.4.
- `spy_data()`
This method can be used to debug the data by looking at events individually (see [33] for description).

A.2.2 Analysis Methods

The methods for analysing the data like, e.g., fitting functions and methods for displaying the data in histograms are contained in the file `analysis.cc`. In the following the most important methods are described:

- `analyze()`
This is the standard method to call to process a data file. It essentially checks which type of ALiBaVa measurement run is contained in the file and selects the appropriate methods to process the data. Depending on the run type either the method `draw_scan()` or `spectrum()` is called.
- `draw_scan()`
This method is applied, if either a calibration run or a laser synchronisation run is processed. It essentially fills the processed data into histograms for further use. If, for the calculation of calibration factors, the range of the linear fit to the ADC response function to the Beetle chip test pulse needs to be changed, this can be done by altering the code here.
- `spectrum()`
This is the main method that handles the files from standard ALiBaVa data taking runs. A number of histograms are defined that can later be used for displaying the data. Subsequently, on an event-to-event basis, the data is processed, the clustering routine is called, and the results are filled into the specified histograms. This method contains a number of additional histograms that were included during the course of this thesis for easier handling of the data. Also, the clustering routine one wants to employ can be chosen here from the two possible versions `find_clusters()` and `find_clusters_vh()` (see section A.3).
- `show_spectrum()`
As its name suggests, this method displays all the processed data. Essentially it draws the histograms that were created and filled with `spectrum()` on a number of canvases. Design parameters and histogram choices can be set here.
- `GausMean_Channels()` and `GausSigma_Channels()`
These are two methods that were added as part of this thesis to facilitate the data handling for the laser tests. They work with a list of histograms that are created in `spectrum()`. Each histogram contains the raw signal data of one ALiBaVa readout channel. Consequently, these methods fit a Gaussian to the signal histogram for every channel to reconstruct the height of the laser signal (mean of the Gaussian). The mean and the standard deviation of the fit are written into a vector respectively. The resulting vector, containing the signal height and the standard deviation for each channel respectively, is returned by each function and can subsequently be used for further processing.

A.2.3 `sin_preguntas.C`

The macro `sin_preguntas.C` is essentially intended as a tool that performs all the necessary analysis on a data file for the user, thus the name “sin preguntas”, which is Spanish for “no questions asked”. It is initially provided by

ALiBaVa, but has been adapted and extended during the course of this thesis to fit the arisen requirements.

A large number of parameters can be passed to the function. For clarification they will be explained here.

- **A**: a pointer to a user supplied `DataFileRoot` (or descendant) object. For most applications this will be an `AsciiRoot` type object. If `sin_preguntas()` is called from the ROOT prompt, **A** can be declared by typing

```
A = new AsciiRoot("[data_file]")
```

and specifying the path to an ALiBaVa data file as the argument. For advanced usage of ALiBaVa it is also possible to write one's own class that inherits from `DataFileRoot` to define any special methods that read the dedicated data blocks of the ALiBaVa data files. (This can become necessary if ALiBaVa is used with a plugin. Refer to [33] for details.)
- **data_file**: the path to the ALiBaVa data file that shall be processed.
- **cal_file**: the path of a calibration file. It can be an ALiBaVa data file produced during a calibration run or an ASCII text file with as many lines as channels, with gain and offset in each line.
- **ped_file**: the path of a pedestal file. It can again be an ALiBaVa data file from a pedestals run or an ASCII text file. If no file is given, `sin_preguntas()` uses the data file to compute pedestals.
- **sensor**: This parameter was added to account for different types of sensors and modules tested with the ALiBaVa system. Essentially, it is needed so that the ALiBaVa channel numbers are correctly converted to the strip numbering of the bonded sensors. The respective sensor type is passed as a simple integer to `sin_preguntas()`. Which number needs to be passed here, depends on the sensor that is investigated and is described in detail in the comments of `sin_preguntas.C`. Per default 0 is passed.
- **clstbegin**: an integer denoting the strip number from where the clustering routine will start the search for clusters. Per default 1 is passed.
- **clstend**: an integer denoting the strip number until which the clustering routine will search for clusters. Per default 120 is passed.
- **polarity**: the polarity of the bias voltage. Possible values are -1 and 1.
- **dofit**: boolean variable that defines whether or not a Landau fit shall be performed for the signal histogram.
- **peaktimesliceinitial** and **peaktimeslicefinal**: integer values to define a time window around the peak of the pulse shape.

After calling the function, `sin_preguntas()` first processes the pedestal and the calibration file. If no pedestal file is given, it computes the pedestals using the method `compute_pedestals()`. If no calibration file is given, all the signals are displayed in ADC counts. Subsequently, the methods `load_gain()`, `load_pedestals()`, and `load_masking()` are called, and finally

the methods `analyze()` and `show_spectrum()` to display the processed data.

When a new user begins to use ALiBaVa and needs to familiarise themselves with the provided macros, looking at the code of `sin_preguntas.C` is a good start to get a feeling of the various methods and how the data is handled.

A.2.4 Processing of the Laser Data

To process the data recorded with AlCoPi laser scans, the method `process_laser_data_chan()` was written. It can be found in the files `process_laser_data_chan.cc` and `process_laser_data_chan.h`. It is based in principle on the structure of `sin_preguntas()`, but adapted for processing a large number of ALiBaVa data files containing the data of laser runs. One can pass the following parameters:

- `datafolder`: AlCoPi stores the ALiBaVa files that are produced during the laser runs in a dedicated folder named after the weekday, date and time of the start of the scan. The path to this folder needs to be passed as first argument.
- `logfilepath`: path to the AlCoPi log file, which contains the numbering of the produced data files and the associated x-, y-, and z-position of the x-y-z stage. It is named like `Log_[datafolder].txt` and is located in the same directory as the datafolder.
- `ped_file`: path to a pedestal file.
- `cal_file`: path to a calibration file.
- `sensortype`: integer denoting which sensor is investigated. Like for `sin_preguntas()`, this parameter is needed to correctly convert the ALiBaVa channel numbers to the strip numbering of the bonded sensors during data analysis. Refer to the comments in either `sin_preguntas.C`, `find_clusters_vh()`, or `process_laser_data_chan.cc` for the sensor numbering convention.

After `process_laser_data_chan()` is called, it processes the data files in `datafolder` according to the specified AlCoPi log file. Essentially the methods `GausMean_Channels()` and `GausSigma_Channels()` are employed to fit a Gaussian to the raw signal histogram for each channel. Subsequently, for every scan step mean and sigma of the Gaussians for all the channels are pushed into two-dimensional vectors. Based on these vectors the data is filled into histograms and graphs that are stored as `.root`-files so that they can be accessed again later without the need to process the raw data files anew, since, depending on the number of scan steps recorded during the AlCoPi run, the data handling can take relatively long.

A.3 Cluster Finding Algorithms

In the following the two clustering routines that are part of the ALiBaVa ROOT macros are introduced. They are both contained in the class `DataFileRoot` and can be found written in the file `DataFileRoot.cc`. Essentially, they both

perform the same job, but there are a number of subtle differences between them.

A.3.1 DataFileRoot::find_clusters()

The method `find_clusters()` is the clustering routine that comes as part of the standard ROOT macros when ALiBaVa is installed. It is contained in two separate methods `find_clusters(int ichip)` and `find_clusters(ChanList &C)`. Depending on the situation, methods like `spectrum()` (see section A.2.2) will call either of the two to initialise the cluster finding algorithm.

The first method takes an integer `chip` as argument that can be used to specify the Beetle readout chip, at the channels of which the routine will look for clusters. A value `chip=0` stands for the first readout chip (channels 0 to 127) and `chip=1` stands for the second chip (channels 128 to 255). If any other number is passed, the clustering routine looks at all 256 Beetle chip channels. From the specified chip number the method then creates an object of type `ChanList`, which is essentially a list of the channel numbers, and calls the second method `find_clusters(ChanList &C)`.

This method is the one, where the actual clustering algorithm is specified. It takes as argument the list of channels (an object of type `ChanList`) for which the clustering routine shall be performed. This list of channels can be passed by the user or otherwise is passed from the first routine `find_clusters(int ichip)` that creates the list of channels according to the specified Beetle chip.

The clustering mechanism now runs through all the channels provided by the `ChanList` object and searches for the channel with the highest signal that exceeds the seed cut. From this channel onwards the routine proceeds to the left and to the right and searches all the channels for signals that exceed the neighbour cut and adds those channels to the cluster. Channels that are added to the cluster are marked as used so that they cannot be added to the same cluster twice, and channels that have been masked by the call of `load_masking()` beforehand are excluded from the cluster search as well. The routine can find at max one cluster per event (trigger) that ranges around the channel with the highest signal of that respective event. However, it does not have any condition implemented other than the begin and end points of the channel list for when a cluster is complete. Thus, it is possible that strips with a high random noise level that otherwise would lie out of the range of a compact cluster are added to the cluster as well. This can in theory result in a number of broader clusters and also in clusters where not all member channels lie directly next to each other. Such errors, however, are expected to be few such that the clustering routine will do a fast and reliable job in most if not all of the cases.

In addition to the standard clustering routine that is contained in `find_clusters()` and was provided by ALiBaVa, during this thesis an extension that calculates the η value (refer to section 4.1.1) for every cluster was included. This value is defined as [44]

$$\eta = \frac{S_R}{S_L + S_R}. \quad (\text{A.1})$$

The values S_L and S_R denote the signals on the left and right channel of the two channels with the highest signal in the cluster respectively. One of these will be the seed channel (the channel with the highest signal) and the other will

be its highest neighbour. Note that either of the two can be the left or the right channel. The such found η values for each cluster can subsequently be used to display the probability density distribution of η (η distribution). The added η -algorithm essentially searches for the second highest signal in the cluster that exceeds the neighbour cut. Then it takes this channel and the seed channel and calculates the η value, differentiating between all the possible cluster sizes, 1, 2, and > 2 , and the respective possibilities of where the neighbour with the highest signal can be located accordingly. For clusters of size 1, where no neighbour exceeds the respective cut, the channel with the highest signal directly next to the seed strip (left or right) is used for the calculation of η .

The such created cluster is subsequently added to the list of hits that have been found in the processed data taking run. The object `Hit` is a member of the class `Hit` and contains all the information about the respective clusters, including left and right end, the channel with the highest signal, total cluster signal, the calculated η value as well as the calculated centre of gravity.

A.3.2 DataFileRoot::find_clusters_vh()

The cluster finding routine that was written as part of this thesis is structured in much the same way as `find_clusters()` with a method `find_clusters_vh(int ichip, int sensor, int begin, int end)` that produces a list of channels according to the specified integer `ichip` and passes it to the method `find_clusters_vh(ChanList &C, int sensor, int begin, int end)`. However, it needs a few more arguments and uses a slightly different approach to compute the clusters. As of now, its main differences as compared to the routine provided by ALiBaVa are the following:

- The cluster search is performed according to sensor strip numbers instead of Beetle chip channel numbers. For this purpose the parameter `sensor` that is essentially an integer number representing the sensor module configuration can be passed to the routine. According to the passed value, the Beetle chip channel numbers will be converted into the according strip numbers.
- The parameters `begin` and `end` can be passed to restrict the cluster search to a specified area of strips. They also correspond to the strip numbering convention instead of the ALiBaVa channel numbers.
- Only compact clusters are considered. A found cluster is considered complete as soon as on the left and right of the seed strip a neighbour that does not exceed the neighbour cut is reached.
- It is possible that more than one cluster per event is found. This allows an option to investigate the frequency and circumstances of fake noise hits.
- Total cluster noise and signal-to-noise ratio of the resulting hit are computed and passed to the object `Hit`.

The cluster search proceeds in the following way: Starting with the lowest strip number (which does not necessarily correspond to the lowest Beetle chip channel number) and excluding all the strips that were masked by the call of `load_masking()` beforehand, a strip that exceeds the seed cut is searched.

If a seed strip is found, it is taken as the starting point to check if the channel next to it on the left exceeds the neighbour cut. If yes, the next left channel is checked and so on, until a neighbouring channel does not exceed the neighbour cut anymore. Subsequently the same process is repeated to the right of the seed. As soon as to the left and to the right any direct neighbour strip of the cluster does not exceed the neighbour cut, the cluster is regarded as complete. All the strips that are part of the cluster are marked as used, η value, cluster noise, signal-to-noise ratio and centre-of gravity are computed and the cluster is passed to the object `Hit`. From this point on the same search routine continues for the rest of the strips that have not yet been checked. If another cluster is found for the same event, it is passed to `Hit` in the same way.

A.4 The Common Mode Algorithm

The common mode correction is performed by the routine `DataFileRoot::common_mode()`, which is included in the standard ALiBaVa macros. Like the clustering routines it is contained in two different methods. The first one assigns the channels 0 to 127 and 128 to 255 to chip 1 and 2 respectively and passes them as channel lists to the second routine, where the actual common mode correction is computed. Per default the common mode is computed separately for each Beetle chip, but with the above mentioned structure the user can also specify a dedicated number of channels for which the common mode shall be computed.

To find the common mode correction, the algorithm runs through the same routine three times. In the first iteration the common mode is computed as the mean of the pedestal corrected signal measured on all channels of the Beetle chip,

$$\langle CM \rangle_1 = \frac{1}{N} \sum_{i=0}^N (s_i - p_i), \quad (\text{A.2})$$

where s_i and p_i are the raw signal and the pedestal on channel i respectively and N is the total number of investigated channels. In the second iteration subsequently strips with extreme noise values and outliers are excluded by computing their deviation from the before calculated common mode mean $\langle CM \rangle$ with

$$\Delta_i = |(s_i - p_i) - \langle CM \rangle| \quad (\text{A.3})$$

and excluding all those with a deviation $\Delta_i > 2.5\sigma_j$, with the standard deviation σ of the j -th channel computed as

$$\sigma_j = \sqrt{\frac{\sum_{i=0}^j (s_i - p_i)^2}{j} - \langle CM \rangle_1^2}. \quad (\text{A.4})$$

From the such reduced values $\langle CM \rangle_2$ is computed again. In the third iteration the process is repeated to tackle also less prominent outliers. The end result is the mean common mode after the thrid iteration $\langle CM \rangle_3$.

Bibliography

- [1] J. W. Goethe. *Faust. Der Tragödie erster Teil*. 382-383. Stuttgart: Philipp Reclam jun., 1986.
- [2] L. Evans and P. Bryant. “LHC Machine”. In: *JINST* 3 (2008). DOI: [10.1088/1748-0221/3/08/S08001](https://doi.org/10.1088/1748-0221/3/08/S08001). URL: iopscience.iop.org/1748-0221/3/08/S08001/pdf/1748-0221_3_08_S08001.pdf.
- [3] CERN Geneva. *CERN-Brochure-2009-003-Eng*. [Accessed: 2017-01-19]. 2009. URL: <http://cds.cern.ch/record/1165534/files/CERN-Brochure-2009-003-Eng.pdf>.
- [4] The LHCb Collaboration. “Implications of LHCb measurements and future prospects”. In: *The European Physics Journal C* (May 2013). DOI: [10.1140/epjc/s10052-013-2373-2](https://doi.org/10.1140/epjc/s10052-013-2373-2). URL: <https://arxiv.org/abs/1208.3355v3>.
- [5] B. Povh et al. *Teilchen und Kerne*. Springer-Verlag Berlin Heidelberg, 2006. DOI: [10.1007/3-540-36686-5](https://doi.org/10.1007/3-540-36686-5).
- [6] D. Contardo et al. *Technical Proposal for the Phase-II Upgrade of the CMS Detector*. Tech. rep. CERN-LHCC-2015-010. LHCC-P-008. CMS-TDR-15-02. CERN. Geneva.: CMS Collaboration, June 2015. URL: <https://cds.cern.ch/record/2020886>.
- [7] CMS Collaboration. *CMS public website*. [Accessed: 2017-01-24]. 2011. URL: <http://cms.web.cern.ch/>.
- [8] Peter W. Higgs. “Broken symmetries, massless particles and gauge fields”. In: *Physics Letters* 12.2 (1964), pp. 132–133. ISSN: 0031-9163. DOI: [http://dx.doi.org/10.1016/0031-9163\(64\)91136-9](http://dx.doi.org/10.1016/0031-9163(64)91136-9). URL: [//www.sciencedirect.com/science/article/pii/0031916364911369](http://www.sciencedirect.com/science/article/pii/0031916364911369).
- [9] Peter W. Higgs. “Broken Symmetries and the Masses of Gauge Bosons”. In: *Phys. Rev. Lett.* 13 (16 Oct. 1964), pp. 508–509. DOI: [10.1103/PhysRevLett.13.508](https://doi.org/10.1103/PhysRevLett.13.508). URL: <http://link.aps.org/doi/10.1103/PhysRevLett.13.508>.
- [10] Nobelprize.org. *The Nobel Prize in Physics 2013*. [Accessed: 2017-01-24]. 2013. URL: http://www.nobelprize.org/nobel_prizes/physics/laureates/2013/.
- [11] V. Karimäki et al. *The CMS tracker system project: Technical Design Report*. Tech. rep. Geneva: CMS Collaboration, 1997. URL: <http://cds.cern.ch/record/368412>.
- [12] *The CMS tracker: addendum to the Technical Design Report*. Tech. rep. Geneva: CMS Collaboration, 2000. URL: <http://cds.cern.ch/record/490194>.
- [13] Maximilien Brice. “First half of CMS inner tracker barrel”. Oct. 2006. URL: <http://cds.cern.ch/record/995912>.

- [14] M. Moll. "Radiation Damage in Silicon Particle Detectors". PhD Thesis. Universität Hamburg, 1999. URL: <https://mmoll.web.cern.ch/mmoll/thesis/pdf/moll-thesis.pdf>.
- [15] Sophie Mallows. *TWiki*, *CMSPublic Web*. [Accessed: 2017-01-26]. 2015. URL: <https://twiki.cern.ch/twiki/bin/view/CMSPublic/BRILRSelbaHGC>.
- [16] S.M. Sze and Kwok K. Ng. *Physics of Semiconductor Devices*. John Wiley & Sons, Inc., 2006. DOI: [10.1002/9780470068328.fmatter](https://doi.org/10.1002/9780470068328.fmatter).
- [17] Gerhard Lutz. *Semiconductor Radiation Detectors*. Springer-Verlag Berlin Heidelberg, 2007. DOI: [10.1007/978-3-540-71679-2](https://doi.org/10.1007/978-3-540-71679-2).
- [18] A. König. "Electrical Characterisation and Aging Studies of Silicon Strip Sensors". Master's Thesis. Universität Wien, 2014.
- [19] C. Patrignani et al. "Review of Particle Physics". In: *Chin. Phys.* C40.10 (2016), p. 100001. DOI: [10.1088/1674-1137/40/10/100001](https://doi.org/10.1088/1674-1137/40/10/100001).
- [20] L. Landau. "On the energy loss of fast particles by ionization". In: *J. Phys.(USSR)* 8 (1944), pp. 201–205.
- [21] H. Kolanoski and N. Wermes. *Teilchendetektoren. Grundlagen und Anwendungen*. Springer-Verlag Berlin Heidelberg, 2016. DOI: [10.1007/978-3-662-45350-6](https://doi.org/10.1007/978-3-662-45350-6).
- [22] T. Bergauer. "Process Quality Control of Silicon Strip Detectors for the CMS Tracker". Master's Thesis. Vienna University of Technology, 2004.
- [23] H. Behnamian. "Sensor R&D for the CMS outer tracker upgrade for the HL-LHC". In: *Journal of Instrumentation* 9.04 (2014), p. C04033. URL: <http://stacks.iop.org/1748-0221/9/i=04/a=C04033>.
- [24] M. Valentan. "The Silicon Vertex Detector for b-tagging at Belle II". PhD Thesis. Vienna University of Technology, 2013.
- [25] E. Frühwirth. "Processing and Characterisation of Silicon Microstrip Detectors produced by Infineon Technologies Austria AG". Master's Thesis. Vienna University of Technology, 2011.
- [26] A. König et al. "Developing silicon strip detectors with a large-scale commercial foundry". In: *Nuclear Instruments and Methods in Physics Research Section A: Accelerators, Spectrometers, Detectors and Associated Equipment* 824 (2016). Frontier Detectors for Frontier Physics: Proceedings of the 13th Pisa Meeting on Advanced Detectors, pp. 419–421. ISSN: 0168-9002. DOI: [http://dx.doi.org/10.1016/j.nima.2015.09.005](https://dx.doi.org/10.1016/j.nima.2015.09.005). URL: [//www.sciencedirect.com/science/article/pii/S0168900215010542](http://www.sciencedirect.com/science/article/pii/S0168900215010542).
- [27] T. Bergauer et al. "First thin AC-coupled silicon strip sensors on 8-inch wafers". In: *Nuclear Instruments and Methods in Physics Research Section A: Accelerators, Spectrometers, Detectors and Associated Equipment* 830 (2016), pp. 473–479. ISSN: 0168-9002. DOI: [http://dx.doi.org/10.1016/j.nima.2016.05.076](https://dx.doi.org/10.1016/j.nima.2016.05.076). URL: [//www.sciencedirect.com/science/article/pii/S0168900216304703](http://www.sciencedirect.com/science/article/pii/S0168900216304703).
- [28] AlibavaSystems S.L. *Alibava Systems*. [Accessed: 2017-03-21]. 2014. URL: <https://www.alibavasystems.com/>.

- [29] R. Marco-Hernández. “A Portable Readout System for Microstrip Silicon Sensors (ALIBAVA)”. In: *IEEE Transactions on Nuclear Science* 56.3 (June 2009), pp. 1642–1649. ISSN: 0018-9499. DOI: [10.1109/TNS.2009.2017261](https://doi.org/10.1109/TNS.2009.2017261).
- [30] R. Marco-Hernández. “Design, development and implementation of a readout system for microstrip silicon sensors. Upgrade for test beam measurements”. PhD Thesis. Universidad de Valencia, 2012.
- [31] S Löchner and M Schmelling. *The Beetle Reference Manual - chip version 1.3, 1.4 and 1.5*. Tech. rep. LHCb-2005-105. CERN-LHCb-2005-105. Geneva: CERN, Nov. 2006. URL: <http://cds.cern.ch/record/1000429>.
- [32] CERN. *ROOT Data Analysis Framework*. 2017. URL: <https://root.cern.ch/>.
- [33] AlibavaSystems S.L. *Alibava Usermanual*. [Accessed: 2017-03-23]. 2014. URL: <https://www.alibavasystems.com/images/Catalogo/alibava-usermanual.pdf>.
- [34] V. Hinger. *ALiBaVa software with adapted ROOT macros*. Feb. 2017. URL: <https://forge.hephy.oeaw.ac.at/scm/svn/user-vhinger/alibava-system>.
- [35] G. Giacomini. “Noise Characterization of Silicon Strip Detectors - Comparison of Sensors with and without Integrated JFET Source-Follower”. PhD Thesis. Università degli studi di Trieste, 2007. URL: http://inspirehep.net/record/1429490/files/fulltext_OhHkIw.pdf.
- [36] G. F. Knoll. *Radiation Detection and Measurements*. John Wiley & Sons, Inc., 2000.
- [37] O. Sokolov. “Prototyping of Silicon Strip Detectors for the Inner Tracker of the ALICE Experiment”. PhD Thesis. Universiteit Utrecht, 2006. URL: <https://dspace.library.uu.nl/handle/1874/10279>.
- [38] J. Magnes et al. *Quantitative and Qualitative Study of Gaussian Beam Visualization Techniques*. Tech. rep. physics/0605102. May 2006. URL: <http://cds.cern.ch/record/948194>.
- [39] J. Eichler, L. Dünkel, and B. Eppich. “Die Strahlqualität von Lasern – Wie bestimmt man Beugungsmaßzahl und Strahldurchmesser in der Praxis?” In: *Laser Technik Journal* 1.2 (2004), pp. 63–66. ISSN: 1863-9119. DOI: [10.1002/latj.200790019](https://doi.org/10.1002/latj.200790019). URL: <http://dx.doi.org/10.1002/latj.200790019>.
- [40] Filmetrics Inc. *Reflectance Calculator*. [Accessed: 2017-03-17]. 2016. URL: <http://www.filmetrics.com/reflectance-calculator>.
- [41] Zhen-Hong Zhou et al. “Epifilm thickness measurements using Fourier transform infrared spectroscopy: Effect of refractive index dispersion and refractive index measurement”. In: *Journal of Applied Physics* 76.4 (1994), pp. 2448–2454. DOI: [10.1063/1.357595](https://doi.org/10.1063/1.357595). URL: <http://dx.doi.org/10.1063/1.357595>.
- [42] B. R. Bennett, R. A. Soref, and J. A. Del Alamo. “Carrier-Induced Change in Refractive Index of InP, GaAs and InGaAsP”. In: *IEEE Journal of Quantum Electronics* 26.1 (Jan. 1990), pp. 113–122. ISSN: 0018-9197. DOI: [10.1109/3.44924](https://doi.org/10.1109/3.44924).

- [43] J. G. E. Gardeniers, H. A. C. Tilmans, and C. C. G. Visser. "LPCVD silicon-rich silicon nitride films for applications in micromechanics, studied with statistical experimental design". In: *Journal of Vacuum Science & Technology A: Vacuum, Surfaces, and Films* 14.5 (1996), pp. 2879–2892. DOI: [10.1116/1.580239](https://doi.org/10.1116/1.580239). URL: <http://dx.doi.org/10.1116/1.580239>.
- [44] R. Turchetta. "Spatial resolution of silicon microstrip detectors". In: *Nuclear Instruments and Methods in Physics Research Section A: Accelerators, Spectrometers, Detectors and Associated Equipment* 335.1 (1993), pp. 44–58. ISSN: 0168-9002. DOI: [http://dx.doi.org/10.1016/0168-9002\(93\)90255-G](http://dx.doi.org/10.1016/0168-9002(93)90255-G). URL: <http://www.sciencedirect.com/science/article/pii/016890029390255G>.
- [45] I. Abt et al. "Characterization of silicon microstrip detectors using an infrared laser system". In: *Nuclear Instruments and Methods in Physics Research Section A: Accelerators, Spectrometers, Detectors and Associated Equipment* 423.2–3 (1999), pp. 303–319. ISSN: 0168-9002. DOI: [http://dx.doi.org/10.1016/S0168-9002\(98\)01337-0](http://dx.doi.org/10.1016/S0168-9002(98)01337-0). URL: <http://www.sciencedirect.com/science/article/pii/S0168900298013370>.
- [46] H. Yin. "Readout software for the Belle II silicon vertex detector and beam test data analysis". Master's Thesis. Vienna University of Technology, 2015.
- [47] Y. Unno et al. "P-stop designs for reducing electric field strength at implant edges". In: *2008 IEEE Nuclear Science Symposium Conference Record*. Oct. 2008, pp. 2507–2512. DOI: [10.1109/NSSMIC.2008.4774864](https://doi.org/10.1109/NSSMIC.2008.4774864).